University of Reading

Electronic structure simulations of energy materials: chalcogenides for thermoelectrics and metal-organic frameworks for photocatalysis

Alex Aziz

September 2017

Submitted in partial fulfillment of the requirements
for the degree of Doctor of Philosophy

Department of Chemistry

University of Reading
Whiteknights
PO Box 217
Reading
Berkshire
RG6 6AH
United Kingdom

Declaration: I confirm that this is my own work and the use of all material from other

sources has been properly and fully acknowledged.

Alex Aziz

Abstract

A theoretical investigation of the electronic structure of chalcogenides for thermoelectric applications and metal organic frameworks (MOFs) for photocatalytic applications is presented in this thesis. The development of chalcogenide materials for thermoelectric applications presents an opportunity to move away from tellurium based materials, which are not cost-effective. Their mainstream realization is dependent on an increase in their efficiency. A combination of density functional theory and Boltzmann transport theory are used to investigate the electronic and phonon transport properties of chalcogenide materials. In the shandite family, the transport properties of $Ni_3Sn_2S_2$ provide a useful rationalization of their behaviour. In $Co_3Sn_2S_2$ indium substitutes tin preferentially at the interlayer sites, and leads to a compositionally induced metal-to-semiconductor-to-metal transition which is critical to its thermoelectric properties. $Cu_2ZnSnSe_4$ is the most promising of the quaternary chalcogenides and is investigated for thermoelectric applications. It is a *p*-type semiconductor and a combined theoretical and experimental analysis shows how its *ZT* can be optimized through doping.

In the second part of this thesis, two classes of MOFs are investigated for their photocatalytic properties, porphyrin based MOFs (PMOFs) and zeolitic imidazolate frameworks (ZIFs). In both materials, DFT calculations are used to obtain the electronic band structure, which is then aligned with a vacuum reference. In these MOFs, as in chalcogenides, chemical substitution can be used to engineer the band structure for their optimal properties. In PMOFs metal substitution at the octahedral metal centre is able tune the band edge positions. Optimal properties were found by partial substitution of Al by Fe at the octahedral sites, while keeping Zn at the porphyrin centres. In ZIFs the band edge positions are mainly determined by the molecular linker and intrinsic photocatalytic activity can be achieved by mixing different linkers.

iii

Acknowledgments

Contents

Nomenclature

Abbreviations

AZGS Ag_2ZnGeS_4

AZGSe $Ag_2ZnGeSe_4$

AZTS Ag_2ZnSnS_4

AZTSe $Ag_2ZnSnSe_4$

BTE   Boltzmann transport equation

BZ   Brillouin zone

CZGS Cu_2ZnGeS_4

CZGSe $Cu_2ZnGeSe_4$

CZTS Cu_2ZnSnS_4

CZTSe $Cu_2ZnSnSe_4$

DFT   Density Functional Theory

DOS   Density of states

GGA   Generalized-gradient approximation

HF   Hartree-Fock

HER   Hydrogen evolution reaction

HOCO   Highest occupied crystal orbital

HSE06   Heyd, Scuseria and Ernzerhof functional

LDA   Local density approximation

LMCT   Ligand to-metal charge transfer

LPAW   Linear projector augmented wave method

LR   Long range

LUCO   Lowest unoccupied crystal orbital

MOF	Metal organic framework
MLWF	Maximally localized Wannier functions
OER	Oxygen evolution reaction
PAW	Projected Augmented Wave
PBE	Perdew-Burke-Ernzerhof
PMOF	Porphyrin metal organic framework
RBA	Rigid band approximation
RTA	Relaxation time approximation
SCF	Self-consistent field method
SOD	Site occupancy disorder
sod	Sodalite topology
SR	Short range
TEG	Thermoelectric generator
VASP	Vienna *ab initio* simulation program
vdW	van der Waal
WF	Wannier function
XC	Exchange correlation
ZIF	Zeolitic imidazolate framework
ZT	Figure of merit

Symbols

Γ^+	Phonon absorption scattering rates
Γ^-	Phonon emission scattering rates
Δ_λ	Deviation to the relaxation time approximation
Ξ	Transport distribution function

$\Phi_{ij}^{\alpha\beta}$	Second order force constants
$\Phi_{ijk}^{\alpha\beta\gamma}$	Third order force constants
Φ	Electrostatic potential
Φ_{av}	Average electrostatic potential
Ω	Spread of the Wannier function
Ω_m	Equivalency in configurational space
∇	Del operator
ε	Energy
κ_{el}	Electronic thermal conductivity
κ_{latt}	Lattice thermal conductivity
κ_{total}	Total thermal conductivity
λ	Mean free path
ρ	Electron probability density
σ	Electrical conductivity
τ	Relaxation time
$\boldsymbol{v}$	Group velocity
φ	One electron wavefunction
ψ	Wavefunction
ω	Frequency
ϕ	Phase of a wave (Wannier functions)
ϕ_u	Basis function
C	Expansion coefficient
$C(\omega)$	Specific heat capacity of a phonon mode
C_{v}	Heat capacity at constant volume
$\boldsymbol{D}$	Dynamical matrix

$\boldsymbol{E}$	Electric field
E_F	Fermi energy
E_c	Potential energy at the conduction band edge
$\boldsymbol{F}$	Force constants matrix
$\boldsymbol{F}_\lambda$	Phonon mean free path
$\boldsymbol{G}$	Reciprocal lattice vector
G	Free energy
$\boldsymbol{H}$	Magnetic field
H	Enthalpy
$\hat{H}$	Hamiltonian
$\boldsymbol{J}$	Current density
L_0	Lorenz number
M	Number of nuclei
M_A	Mass of nuclei A
N_c	Number of inequivalent configurations
N	Number of electrons
P_m	Probability of occurrence of the mth configuration
$\boldsymbol{Q}$	Heat flux density
R	Gas constant
R	Position of a nuclei
$\boldsymbol{R}$	Associated unit cell
S	Seebeck coefficient
$\boldsymbol{T}$	Translational vector
T	Temperature
$\bar{T}$	Mean operating temperature

T_C	Temperature at the cold side of a material
T_H	Temperature at the hot side of a material
U	Unitary transformation
V	System volume
Z_A	Charge of nuclei A
Z	Configurational partition function
$\hat{f}$	Fock operator
f_0	Equilibrium distribution
f_λ	Non-equilibrium distribution for phonons
f_k	Non-equilibrium distribution for electrons
f_{dmp}	Damping function
$\hbar$	Reduced Planck's constant
h_i^{KS}	One electron Kohn-Sham Hamiltonian
k	Wavevector
k_B	Boltzmann's constant
m_e	Mass of an electron
n	Band index
$p\text{-}n$	Carrier concentration (holes minus electrons)
q	Phonon wavevector
r	Position of an electron
t	Time
v	Potential energy
w_{nR}	Wannier function of the nth band of the Rth unit cell

1   Introduction

1.1   Motivation

Guaranteeing the supply for increasing levels of energy consumption is one of the greatest challenges faced by humanity in the 21st century. Global population growth and industrialisation is expected to lead to a 48% increase in energy consumption from 2012 to 2040.[1] Even with an expected 2.6% rate in renewable energy generation, it is still expected that in 2040 fossil fuel will still account for 78% of the worlds energy use in 2040. The continued exploitation of fossil fuels, a finite resource, is clearly unsustainable in the long term.

The content of this thesis is related to two remedial solutions to combat climate change. The first is a reduction in energy demand through increasing energy efficiency. Increasing energy efficiency could be implemented at any stage of power generation. Energy losses occur across all types of industries, in factories, in all electrical devices and in homes. Power stations are only typically 40-60% efficient in generating electrical energy. In the automotive industry combustion engines only convert ~35% of energy into useful mechanical energy. Around 40% is lost directly in the production of mechanical energy and another 25% is lost in cooling the engine. Any energy not utilised in these processes will ultimately be lost as heat. Increasing energy efficiency can be achieved directly in the application, or indirectly by harvesting the waste heat and converting it back to useful energy. Harvesting waste heat presents a novel opportunity to increase energy efficiency and reduce fossil fuel consumption. The conversion of heat back into electricity has been known for nearly 200 years. The phenomenon was discovered in 1821 and is known as the Seebeck effect. Materials that exhibit this property are known as thermoelectric materials and it is this class of materials that will be studied.

The second remedial solution to climate change is a continued move to renewable energy. The current main sources of renewable energy generation can be divided into solar photovoltaics (PV), wind, bioenergy, geothermal and hydropower. Whereas solar PV converts solar energy directly in electricity, the work discussed in the second part of this thesis focuses on photocatalytic reactions involved in water splitting to produce hydrogen or the reduction of carbon dioxide to produce organic fuels like methane or methanol.

1.2   Thermoelectric materials

When a thermoelectric material is subject to a temperature gradient there is a build-up of an electric potential due to the diffusion of free carriers (electrons or holes) from the hot side of the material to the cold side. At the hot side, carriers have more energy and can diffuse at a faster rate. Charge subsequently builds up at the cold side of the material and a balance is reached generating a voltage difference or a "thermoelectric force". Thomas Seebeck discovered this effect when he connected two different metals in a circuit with their junctions held at different temperatures, the generated current deflected a compass magnet. This is referred to as a closed-circuit thermocouple and the connected materials are often referred to as thermocouple legs (Figure 1.1).[2] To utilise a current in a thermoelectric generator (TEG) device one of the thermocouple legs should be *n*-type (conduct electrons) and the other *p*-type (conduct holes). A thermocouple leg that allows the conduction of both electrons and holes from the hot side to the cold side will result in a cancellation of the induced Seebeck voltage.
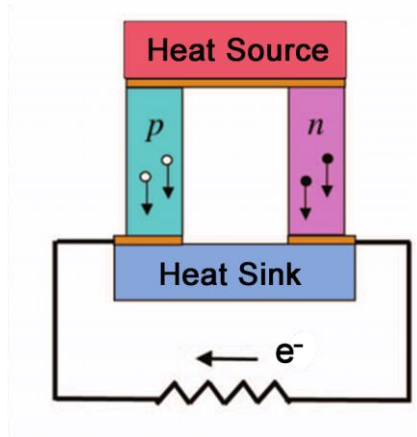
Figure 1.1. A closed-circuit thermocouple with its *p*-type and *n*-type thermocouple legs shown

Thermoelectric devices have no moving parts, making them easy to maintain, and can be easily miniaturized, making them suitable for both large-scale devices such as power stations and small scale applications such as engines, laptops or even mobile phones. This gives thermoelectric generators several distinct advantages over photovoltaic solar panels, which are expensive to install and require a large space. Their miniaturisation also allows micro-generation of energy with their possible installation in gas boilers in homes and buildings. When a current is supplied to a thermoelectric device it can act in reverse and act to cool a device. This is known as the Peltier effect and may also present an opportunity to reduce energy consumption by efficient cooling of internet data centres and supercomputers. In space, thermoelectric devices are used to power satellites with heat generated from the decay of a radioactive material.

Thermoelectric devices have not yet seen mainstream implementation due to their fabrication costs and low efficiencies. Traditional thermoelectric materials are mainly based on Bi_2Te_3, with efficiencies in the region of 2-5%.[3] They are currently uncompetitive with traditional energy generation and pose an investment risk due to the increasing costs of tellurium.[3] Furthermore, tellurium is toxic, posing a risk to the

environment and human health. As a result, there is a growing research effort into increasing the efficiency of tellurium-free thermoelectric materials.

The performance of a thermoelectric material is assessed based on a dimensionless value, known as its figure of merit (ZT):

$$ZT = \frac{\sigma S^2 T}{\kappa_{\text{el}} + \kappa_{\text{latt}}} \tag{1.1}$$

where σ is the electrical conductivity, S is the Seebeck coefficient (the potential difference generated per degree of applied temperature difference), T is the absolute temperature and κ_{el} and κ_{latt} are the electronic and thermal lattice conductivities respectively.[3] The lattice thermal conductivity is the result of phonon propagation in the material. It is important to stress that the ZT is an intrinsic property of the material, and as such it can only give a partial indication of the efficiency of a full device, which requires two thermoelectric materials connected in a circuit. A modified ($Z\bar{T}$) can be defined, representing the thermoelectric capacity after considering the ZT of the each of the thermoelectric materials at the mean operating temperature ($\bar{T}$). The efficiency (η) of the thermoelectric device is given as

$$\eta\,(\%) = 100.\left(\frac{T_{H-}T_C}{T_H}\right).\frac{\sqrt{1 + Z\bar{T}} - 1}{\sqrt{1 + Z\bar{T}} + \left(\frac{T_C}{T_H}\right)} \tag{1.2}$$

where T_H and T_C are the temperatures on the hot and cold side respectively.[4] Equation (1.2) suggests that to maximise efficiency the device should be operated at the highest possible temperature difference between the hot and cold side, but the temperature also affects the ZT of each of the respective materials. It is also clear from Equation (1.1) that to maximise the ZT the power factor (σS^2) must be maximised while the thermal

conductivity must be minimised. This presents a challenge as these parameters are not independent of each other. For example, increasing the electrical conductivity also has the effect of increasing the electronic component of the thermal conductivity, which tends to reduce the temperature gradient.

One way an increase in ZT can be achieved is through doping. Doping a material has the effect of changing the carrier concentration which also changes the Fermi level of the material, allowing the tuning of both σ and S. Nanostructured materials show promise in the reduction of the lattice thermal conductivity κ_{latt}, as their surfaces limit the propagation of phonons. Dopants can also introduce disorder and phonon scattering sites that reduce the lattice thermal conductivity.[5] In the so-called Phonon Glass Electron Crystals (PGEC) materials, electrons are able to pass through the solid with a high conductance, *i.e.* the material acts as a crystal to the electrons. Phonons on the other hand are highly scattered by the material, *i.e.* the material acts as a glass to the phonons.[6] In pseudo-2D layered materials one layer may act as a phonon scatterer, minimising the lattice thermal conductivity, while another layer acts as a conduction layer, to obtain a maximised value for ZT.[7]

The ideal operating temperature range for a thermoelectric device is material-specific, this adds another challenge to the goal of using thermoelectric materials for energy recovery. The material selected in a TEG device should have an optimal ZT close to the temperature at which it is to be used for energy recovery, which leads to three distinct groups of thermoelectric materials. At low operating temperatures from around room temperature to 450 K, Bi_2Te_3 is currently the material of choice; in the mid temperature regime between 500-900 K there are the PbTe- and $CoSb_3$-based materials;[8] and above 1000 K SiGe alloys are typically used.[9, 10] As thermoelectric research continues to expand, the goal is to increase efficiencies while avoiding toxic elements such as Pb

and Te and use earth abundant elements in order to reduce costs and avoid price fluctuations.

In the first part of this thesis we will deal with two families of metal chalcogenides with potential as thermoelectric materials. Chapter 3 focuses on the tertiary chalcogenide with the shandite mineral structure; a class of layered materials with the general formula $A_3M_2X_2$ (A = Ni, Co, Rh, Pd, M = Pb, In, Sn, Tl, X=S, Se).[3,11] Previous work by Corps *et al.*[3] has shown there may be significant scope to increase the *ZT* of the material through doping. Chapter 4 investigates a group of quaternary chalcogenides with the form A_2ZnBQ_4 (A = Cu, Ag; B = Sn, Ge; Q = S, Se) that have been reported in both the kesterite and stannite crystal structures. They have attracted great interest in solar PV as have shown efficiencies of up to 12.6%,[12, 13] but have also recently gained attention for their use as intermediate thermoelectric materials.[14, 15]

1.3   Photocatalytic materials

The second part of this thesis focuses on photocatalytic materials and their potential use in fuel synthesis. Solar-driven photocatalysis of water splitting to produce hydrogen and of the reduction of CO_2 into organic fuels such as methane and methanol[16, 17] offers great potential to increase the supply of renewable energy at a low environmental impact.[18-20] The water splitting reaction can be electrochemically divided in two half-reactions. The oxidation half-reaction is the oxygen evolution reaction (OER):

$$H_2O \leftrightarrow 2H^+_{(aq)} + \frac{1}{2}O_{2(g)} + 2e^-, \qquad (1.3)$$
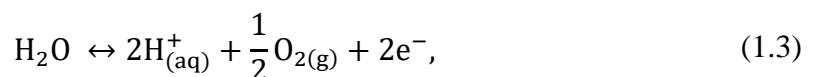
while the reduction half-reaction is the combination of the generated protons and electrons to produce hydrogen gas, which is called hydrogen evolution reaction (HER):

$$2H^+_{(aq)} + 2e^- \leftrightarrow H_{2(g)} \tag{1.4}$$

As in the case of thermoelectric materials, the key to optimise the functionality of photocatalytic materials is engineering their electronic structure. For water splitting to occur, the band gap must be narrow enough to permit the absorption of incoming electromagnetic radiation, but at the same time must be wide enough for the band edges to straddle the redox potentials for water photolysis.[21-23]

Since Fujishima and Honda first reported the photocatalysis of water using a TiO_2 electrode,[24] research has continued into the search for suitable photocatalysts.[25-27] Initially research was focussed on inorganic semiconductors[20, 24, 28-30] but has now expanded to a wider class of materials, including nanostructures such as fullerenes, nanotubes and graphene-like 2D solids.[31-35] As water splitting and CO_2 reduction are the core reactions in photosynthesis,[36] research has been extended to artificial photosynthesis biomimeticing nature.[20, 37-39] Some work has focused on Mn-complexes, which are similar to the metallo-oxo cluster of four manganese ions that form the active site for the OER in natural photosynthesis.[40-42]

Another class of molecules which have been shown to exhibit photocatalytic properties are porphyrins[43, 44] and are composed of four interconnected pyrrole subunits allowing an active metal iron to co-ordinate to the four interior nitrogen atoms, similar to the structure of haemoglobin. The caveat with molecular systems is that their complicated separation from the liquid media is necessary for recyclability. A possible solution that has been proposed is their immobilization in solid hosts.[45, 46] Metal-organic frameworks (MOFs) consisting of metal ions co-ordinated to organic ligands have appeared as promising hosts,[47-50] where catalytic centres can be encapsulated[51-55] or moreover be part of the constituents of the materials.[55-58] After pioneering work by Suslick and

coworkers,[59] a number of porphyrin-based MOFs were reported (PMOFs),[60-63] including some with photocatalytic properties.[60-62] Chapter 5 of this thesis investigates the photocatalytic potential of porphyrin-based MOFs, where we tune the electronic structure by varying the metal at the porphyrin metal centre and also the octahedral metal ion which coordinates to the organic linkers. Chapter 6 focuses on a different class of MOF, known as zeolitic imidazolate frameworks (ZIFs). ZIFs are composed of tetrahedrally-coordinated transition metal ions connected by imidazolate linkers. They are topologically isomorphic with zeolites as the 145° metal-imidazole-metal angle is similar to the Si-O-Si angle found in zeolites. The investigation of ZIFs takes a similar approach to that of the porphyrin MOFs, but in this case the imidazole linker is modified and its subsequent potential as a photocatalyst investigated.

1.4   Objectives

The overall goal of this thesis is to use advanced computer simulation techniques to understand, and then potentially optimise, the electronic structure of a group of materials with potential applications in thermoelectric and photocatalytic devices.

In the first part of this thesis the aim is to calculate the electronic structure, electron transport and phonon transport properties of two families of chalcogenide materials. The next step is to validate the computational results by their comparison with experimental work that has been done concurrently by our collaborators. Successful validation of the computational results will justify the future use of the theoretical models used for other systems or alternatively suggest ways that the models can be improved in future work. It is hoped the successful the validation of the computational results will give an insight into understanding the underlying mechanisms behind the material's properties and act as a guide for experimentalists to optimize the material and increase its thermoelectric performance. The long-term goal is to reach efficiencies where thermoelectric energy generation is competitive with other energy generation mechanisms which will allow their use in mainstream applications.

In the second part of this thesis photocatalytic materials are investigated. The first goal is to accurately obtain the electronic structure and the band gaps of the materials. The second step is to align the band edges to the vacuum level to compare their band edges with that of the water splitting and carbon dioxide fixation reactions. This is an important step as the materials photocatalytic properties are dependent on their valence band edge lying below the potential of the oxygen evolution reaction and their conduction band edge lying above that of hydrogen evolution reactions. It is hoped that this band alignment will give key information to experimentalists on which materials show the most promise as photocatalysts.

2　　Theoretical background

2.1　　Electronic structure calculations

2.1.1　　Quantum mechanical methods

In quantum mechanics, the stationary states (ψ) of the system are the eigenfunctions of the Hamiltonian operator ($\widehat{H}$), leading to the equation[64]

$$\widehat{H}\psi = E\psi \tag{2.1}$$

where E is the energy of the stationary state. For example, for a one electron system $\widehat{H}$ is the solution to the time-independent Schrödinger equation

$$\left[-\frac{\hbar^2}{2m_e}\nabla^2 + V(\boldsymbol{r})\right]\psi = E\psi \tag{2.2}$$

where m_e is the mass of the electron, $\hbar$ is the reduced Planck's constant, ∇ is the "del" operator, $V(\boldsymbol{r})$ is the external potential and ψ is the wavefunction. As the system size is increased, solving the Schrödinger equation soon becomes a formidable task. In the general case, the Schrödinger equation for M nuclei and N electrons is

$$\left[-\sum_{i=1}^{N}\frac{\hbar^2}{2m_e}\nabla_i^2 - \sum_{A=1}^{M}\frac{\hbar^2}{2M_A}\nabla_A^2 - \sum_{i=1}^{N}\sum_{A=1}^{M}\frac{Z_A e^2}{r_{iA}} + \sum_{i=1}^{N}\sum_{j\neq i}^{N}\frac{e^2}{r_{ij}}\right.$$

$$\left. + \sum_{A=1}^{M}\sum_{B\neq A}^{M}\frac{Z_A Z_B e^2}{R_{AB}}\right]\psi = E\psi \tag{2.3}$$

where M_A is the mass of nucleus A, Z_A represents the charge (atomic number) of nucleus A, r_{ij} is the distance between the electron i and j and R_{AB} is the distance between nuclei A and B. The first term is the kinetic energy of the electrons and the second term is the kinetic energy of the nuclei. The remaining three terms are Columbic terms representing

electron – nuclei interactions, nuclei-nuclei repulsion and electron-electron repulsion respectively. Equation (2.3) is simplified by using atomic units ($\hbar = 1$, $m_e = 1$, e = 1).

$$\left[-\sum_{i=1}^{N} \frac{1}{2} \nabla_i^2 - \sum_{A=1}^{M} \frac{1}{2M_A} \nabla_A^2 - \sum_{i=1}^{N} \sum_{A=1}^{M} \frac{Z_A}{r_{iA}} + \sum_{i=1}^{N} \sum_{j \neq i}^{N} \frac{1}{r_{ij}} + \sum_{A=1}^{M} \sum_{B \neq A}^{M} \frac{Z_A Z_B}{R_{AB}} \right] \psi \tag{2.4}$$
$$= E\psi$$

As the number of atoms in a system increases, the number of variables needed to solve the Schrödinger equation increases, this makes solving the Schrödinger for any more than a few atoms computationally impossible. Simplification of the problem is possible by applying the Born-Oppenheimer approximation.[65] The Born-Oppenheimer approximation treats the nuclei as being fixed in position, as they are much greater in mass than the electrons and their kinetic energy is neglected. As the electronic energy depends on the positions of the nuclei they can be moved incrementally, each time resolving the Schrödinger equation to build up the energy landscape of the system.

$$\left[-\sum_{i=1}^{N} \frac{1}{2} \nabla_i^2 - \sum_{i=1}^{N} \sum_{A=1}^{M} \frac{Z_A}{r_{iA}} + \sum_{i=1}^{N} \sum_{j \neq i}^{N} \frac{1}{r_{ij}} \right] \psi = E_e \psi \tag{2.5}$$

Once the nuclei positions corresponding to lowest energy configuration are calculated, their positions can be re-introduced into the Hamiltonian and their kinetic energy calculated. The convention is not to include the classical nuclear-nuclear repulsion in the Hamiltonian but to add it in at the end of the calculation.[64, 66] This is possible as the Hamiltonian depends on the electronic coordinates. The nuclear-nuclear repulsions are independent of the electronic wavefunctions, the addition of the nucleus-nucleus contribution just acts to shift the energy levels by a constant.[64]

2.1.2 Hartree-Fock theory

A further approximation is set to constraint the form of the multielectron wavefunction, which can be represented as a Slater determinant.

$$\psi(x_1, \ldots, x_N) = \frac{1}{\sqrt{N!}} \det \begin{vmatrix} \varphi_a(x_1) & \varphi_b(x_1) & \ldots & \varphi_z(x_1) \\ \varphi_a(x_2) & \varphi_b(x_2) & \ldots & \varphi_z(x_2) \\ \vdots & \vdots & \ldots & \vdots \\ \varphi_a(x_N) & \varphi_b(x_N) & \ldots & \varphi_z(x_N) \end{vmatrix} \tag{2.6}$$

The multi-electron wavefunction's representation as a Slater determinant rather than as the product of the individual wavefunctions is necessary to comply with the antisymmetry principle, which is related to the Pauli exclusion principle: two electrons cannot have the same spatial coordinates and spin. If only two electrons are considered the slater determinant would be

$$\psi(x_1, x_2) = \frac{1}{\sqrt{2}} \det \begin{vmatrix} \varphi_a(x_1) & \varphi_b(x_1) \\ \varphi_a(x_2) & \varphi_b(x_2) \end{vmatrix} \tag{2.7}$$

If the coordinates and spins are exchanged by swapping the columns the determinant just changes sign. If the electrons are in the same spin state and position the determinant equals zero. There is no probability of this happening as the probability is given by the square of the wavefunction.

The next step in HF theory is to find the one-electron wavefunctions. The best choice of wavefunction is one which minimises the total energy:

$$E_e = <\psi|\hat{H}|\psi> \tag{2.8}$$

The one-electron wavefunction that minimises E_e obeys the equation:

$$\hat{f}_i \varphi_i = \varepsilon_i \varphi_i \tag{2.9}$$

where $\widehat{f_i}$ is an effective one-electron operator (Fock operator):

$$\widehat{f_i} = -\frac{1}{2}\nabla_i^2 - \sum_{A=1}^{M}\frac{Z_A}{r - R_A} + \hat{v}_i^{HF}$$ (2.10)

Here the first term represents the kinetic energy of the ith electron, the second term represents a Coulombic interaction between the electron and each atom in the system and the third term is the interaction between the electron and all other electrons in the system and is known as the HF potential. The HF potential depends on the other electron wavefunctions so must be solved in an iterative manner. This is known as the self-consistent field method (SCF). An initial guess of the electron orbitals is made and the HF potential is calculated. This is used to solve Equation (2.9) and to obtain a new set of orbitals. The process is then continued until a convergence criterion is met.

The molecular orbitals are typically expressed as linear combinations of atomic orbitals, with a variety of choices in the number and type of atomic orbitals making up the basis set for the expansion.

$$\varphi_i(\mathbf{r}) = \sum_{\mu=1}^{K} C_{\mu i}\phi_\mu(\mathbf{r})$$ (2.11)

Here ϕ represents the basis function or atomic orbital, which in molecular calculations is typically chosen as Slater- or Gaussian-type functions or a mixture of both. With the choice of atomic function, the last step is to calculate the C coefficients. In principle, the basis set expansion is exact when K reaches infinity, which is obviously not possible, therefore in practise a cut off is used for the expansion.

There are two main sources of error at this level of theory. There is the error given by the incompleteness of the basis set using a cut off for K. But there is also an intrinsic

error due to the representation of the all-electron wavefunction from independent one-electron orbitals in the form of the Slater determinant. The difference in energy between the Hartree-Fock solution (in the limit of an infinite basis set) and the exact ground state of the system is known as the correlation energy.

2.1.3 Density functional theory (DFT)

Density Functional Theory (DFT) became popular in the 1990s and is based on the Hohenberg-Kohn theorems.[67] The first theorem known as the Hohenberg-Kohn existence theorem states that "for any system of interacting particles in an external potential, the external potential, and hence the total energy, is a unique functional of the electron density." The DFT method is not based on a multi-electron wavefunction but on the expression of the electronic energy as a functional of the electron density. In a similar manner to HF theory the energy is solved in a self-consistent process which approaches the ground-state energy of the system as stated by Hohenberg-Kohn's variational theorem. "For a trial electron density function $\rho(r)$, the energy given by the density functional cannot be less than the true ground-state energy of the molecule". DFT calculations are simplified in the same way as other *ab initio* theories using the Born-Oppenheimer approximation.[65] The electronic energy E_e can be given as a functional of the electron density:

$$E_e[\rho(r)] = T_e[\rho(r)] + V_{ne}[\rho(r)] + V_{ee}[\rho(r)] + E_{xc}[\rho(r)] \qquad (2.12)$$

Equation (2.12) is analogous to Equation (2.4) where here the first term represents the kinetic energy of the electron, the second and third terms make up the classical electrostatic electron energy given by nuclei-electron repulsion and electron-electron repulsion respectively. The fourth term is known as the exchange-correlation functional.

It includes the correlation energy as well as the exchange energy, which relates to the exchange of the electrons spin and non-classical electron – electron interactions.

The electron density of the system is constructed from a set of auxiliary one-electron orbitals corresponding to non-interacting electrons.[68]

$$\rho(\boldsymbol{r}) = \sum_{i=1}^{N_e} |\psi_i|^2 \tag{2.13}$$

The one-electron orbitals that minimize the energy in Equation 2.13 under the condition (2.14) are the eigenfunctions of the one-electron Kohn-Sham Hamiltonian h_i^{KS}

$$h_i^{KS} \psi_i^{KS} = \varepsilon_i^{KS} \psi_i^{KS} \tag{2.14}$$

where the one electron Hamiltonian is

$$h_i^{KS} = -\frac{\hbar}{2m_e} \nabla_i^2 + v_{\text{eff}}(\boldsymbol{r}_i) \tag{2.15}$$

The effective potential is given in terms of the electron density $\rho(\boldsymbol{r}')$

$$v_{\text{eff}}(\boldsymbol{r}) = v(\boldsymbol{r}) + \int \frac{\rho(\boldsymbol{r}')}{|\boldsymbol{r} - \boldsymbol{r}'|} d\boldsymbol{r}' + v_{\text{xc}}(\boldsymbol{r}) \tag{2.16}$$

The exchange-correlation density functional defines the exchange-correlation potential

$$v_{\text{xc}}(\boldsymbol{r}) = \frac{\partial E_{\text{xc}}[\rho]}{\partial \rho(\boldsymbol{r})} \tag{2.17}$$

An initial guess of Kohn-Sham orbitals leads to an initial value of $\rho(\boldsymbol{r})$ which can be used to define the effective potential. Solving the Kohn-Sham equation will lead to a new set of Kohn-Sham orbitals. The cycle can be repeated using the SCF method until convergence is achieved.

The simplest representation of the exchange-correlation functional is the local density approximation (LDA) introduced by Kohn and Sham[68] where the exchange-correlation energy per particle at a given point of space is a function of the local electron density. This work uses density functionals based on the generalized-gradient approximation (GGA), in particular the PBE functional developed by Perdew, Burke and Ernzerhof, where the exchange correlation energy per particle depends on the local electron density and also on its gradient.[69, 70]

2.1.4 Solid state systems

Solid state systems are periodic and can be represented by the repetition of a unit cell in all directions. In periodic systems Bloch's theorem can be used to find a solution to the wavefunction.[71] Bloch's theorem proves that a wavefunction within a perfectly periodic potential (such as a crystal) can be expressed as a Bloch function which has the form:

$$\psi_k(\boldsymbol{r}) = e^{ik.r}u_k(\boldsymbol{r}) \tag{2.18}$$

where $u_k(\boldsymbol{r})$ is a periodic function with the periodicity of the lattice. Bloch's theorem implies that $\psi_k(\boldsymbol{r})$ is related to $\psi_k(\boldsymbol{r} + \boldsymbol{T})$, where $\boldsymbol{T}$ is a translational vector to the next unit cell, by just a phase shift $(e^{ik.T})$:

$$\psi_k(\boldsymbol{r} + \boldsymbol{T}) = e^{ik.T}\psi_k(\boldsymbol{r}) \tag{2.19}$$

Since the function $u_k(\boldsymbol{r})$ is periodic, it can be expanded as a Fourier series:

$$u_k(\boldsymbol{r}) = \sum_{G} u_G e^{iG.r} \tag{2.20}$$

where the G vectors represent the points of the reciprocal lattice. Equation (2.20) can then be substituted into Equation (2.18) to give an expression for the wavefunction as a sum of plane waves:

$$\psi_k(\boldsymbol{r}) = \sum_G C_{k+G} e^{i(k+G).\boldsymbol{r}}$$

(2.21)

where the expansion coefficients C_{k+G} contain all the information about the wavefunction. The summation is performed over all G-points in the reciprocal space. However, the higher the value of G the higher the kinetic energy corresponding to the plane wave. At high kinetic energy, the basis functions that make up the summation will have negligible weight and the kinetic energy cut off can be chosen based on specific convergence criteria. This method is known as the plane wave expansion method. The k-grid and the energy cut off (G_{max}) used in DFT calculations are two essential parameters that must be checked for convergence.

In the plane wave method, the wavefunction is very close to a sinusoidal wave in the interstitial region which is appropriate for the plane wave model. In the region close to the atomic nuclei the wavefunction varies rapidly. In order to model the core region around the nuclei a very high order of plane waves would be required. The alternative is to separate the wavefunctions for the core region (associated with core electrons) and the interstitial regions which are generally associated with the valence electrons. This work used two programs for DFT calculations, with different treatments of the core electrons: the Vienna *ab initio* simulation program (VASP)[13,14,15] and WIEN2k.[72]

VASP keeps core electrons frozen at their reference atomic state using the projector augmented wave method (PAW).[73, 74] The PAW potentials are available within VASP. Plane wave expansion is only performed on the valence electrons. The one

electron wave functions are then combined with the one electron wavefunctions of the core electrons (using the pseudo-potentials) to form a complete basis set.

In contrast WIEN2k is an all-electron code, which means that the core electron levels are also calculated. The method separates the unit cell into non-overlapping atomic spheres centred on each nucleus and an interstitial region based on distances from each nucleus rather than by core and valence electrons. In the core atomic sphere region the linear augmented plane wave (LAPW) method is utilised,[73, 74] and a linear combination of a radial functions multiplied by spherical harmonics are used to solve the radial Schrödinger equation. Convergence of this basis set then depends on the cut off parameter $R_{mt}K_{max}$. R_{mt} is the smallest atomic sphere radius in the unit cell and K_{max} is the magnitude of the largest K vector. In the interstitial region plane wave expansion is utilised as in VASP. The VASP code was the chosen for geometry optimisation and electron structure calculations due to its lower computational cost. WIEN2k was occasionally preferred for electronic structure calculations as it more readily interfaced with other required codes.

2.1.5   Correction to the self-interaction problem

A major problem arising in DFT in the GGA approximation is the electron self-interaction problem, where GGA calculations wrongly include repulsion where an electron appears to repel itself (Figure 2.1). This problem arises mainly with d and f-orbitals which have very localised states. This self-interaction leads to delocalisation of the charge density, which results in an underestimation of band gap.
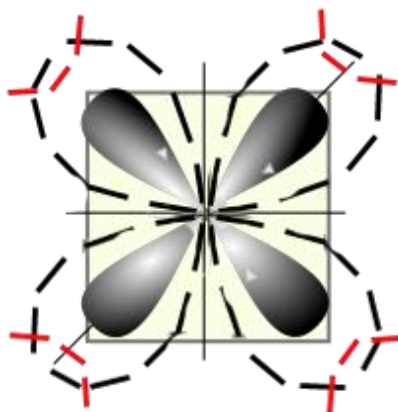
Figure 2.1. Representation of a localised *d* orbital (shaded). Due to self-interaction the DFT-calculated orbital expands as indicated by the black dotted lines. This results in an increased overlap with orbitals from ligands (red dotted lines). The DFT+U acts by penalizing that overlap.

To overcome this self-interaction problem the GGA+U correction is often applied. In the Dudarev approach,[75] the GGA+U energy includes a penalty term U which is proportional to the overlap (hybridisation) of *d* orbitals with ligands' *p*-orbitals.

$$E_{\text{GGA+U}} = E_{\text{GGA}} + U \times \text{Hybridisation} \qquad (2.22)$$

Therefore, the GGA+U method tends to contract the *d* orbitals in comparison with the pure GGA solution, thus recovering the correct degree of localisation. The technique relies on an effective U (U_{eff}) which is equivalent to the difference between the Hubbard-like Coulomb interaction (U) and the screened Stoner exchange parameter (J).

Where accurate band gaps are required another possible method to deal with GGA limitations is to use a hybrid functional. Hybrid functionals incorporate both HF theory and GGA in the calculation of the exchange component:

$$E_{xc}^{\text{hybrid}} = aE_x^{\text{HF}} + (1-a)E_x^{\text{GGA}} + E_c^{\text{GGA}}. \qquad (2.23)$$

This achieves a balance between the underestimation of the band gap in GGA and an overestimation of the band gap in HF theory. By combining the two theories into a hybrid functional accurate band gaps are generally obtained, albeit at a significantly higher computational cost in plane wave formulations.

The HSE06 functional is a special case of hybrid functional, which mixes the HF and PBE exchange energies as the Heyd, Scuseria and Ernzerhof functional (HSE06).[76, 77] In general, the HF exchange energy (E_x^{HF}) is calculated in real space as the sum over all the significant interactions in the unit cell and neighbouring cells. This gives the HF exchange energy as a function of distance from the reference cell. The problem is that convergence is extremely slow with distance from the reference cell. To achieve convergence Heyd *et al.*[76, 77] separate the exchange term into long-range (LR) and short-range (SR) contributions. The HSE06 functional screens out the long-range (LR) part of the HF exchange, leading to the expression:

$$E_{xc}^{\omega\mathrm{HSE06}} = aE_x^{\mathrm{HF,SR}}(\omega) + (1-a)E_x^{\mathrm{PBE,SR}}(\omega) + E_x^{\mathrm{PBE,LR}} + E_c^{\mathrm{PBE}} \qquad (2.24)$$

where ω is an adjustable parameter which governs the extent of the short-range interactions and a which equals ¼ is the mixing coefficient. The HSE06 functional leads to very accurate bandgaps of semiconducting materials.[78]

The correlation between fluctuating charge distributions are not accurately described by local DFT functionals and therefore corrections are often needed to account for van der Waal (vdW) forces and obtain more accurate geometries. In a series of methods by Grimme,[79-81] the total energy of the system is given by:

$$E_{\mathrm{DFT-D}} = E_{\mathrm{DFT}} + E_{\mathrm{disp}} \qquad (2.25)$$

where E_{KS-DFT} is the Kohn-Sham DFT energy and E_{disp} is an empirical dispersion energy correction. Several approaches exist to calculate this vdW correction, including the DFT-D2[80] and DFT-D3[81] methods which depend on a dispersion coefficient (C_6^{ij}) for atoms pair i and j. In the DFT-D2 method, the C_6^{ij} coefficients are geometry independent and are based only on the geometric mean of tabulated dispersion coefficients (C_6):

$$C_6^{ij} = \sqrt{C_6^i C_6^j}. \tag{2.26}$$

The DFT-D3 method is a more accurate, less empirical extension of the DFT-D2 method where C_6^{ij} are geometry dependent, do not rely on atom connectivity and are computed explicitly. In Chapter 5 of this thesis the DFT-D2 method was used to investigate the effect of vdW interactions on geometries and electronic structures, but the results were found to be independent of the particular dispersion correction.

In both methods dispersion coefficients are used to calculate the dispersion energy correction, in the DFT-D2 method E_{disp} is calculated as follows:

$$E_{\text{disp}} = -s_6 \sum_{i=1}^{N_{\text{at}-1}} \sum_{j=i+1}^{N_{\text{at}-1}} \frac{C_6^{ij}}{R_{ij}^6} f_{\text{dmp}}(R_{ij}) \tag{2.27}$$

where the dispersion is summed over all the atoms in the system (N_{at}), R_{ij} is the interatomic distance and s_6 is a global scaling factor that depends on the functional used. As vdW forces are long range and to avoid small range contributions a damping function (f_{dmp}) is used:

$$f_{\text{dmp}}(R_{ij}) = \frac{1}{1 + e^{-d\left(\frac{R_{ij}}{R_r} - 1\right)}} \tag{2.28}$$

where d is kept constant at 20 and R_r is the sum of the atomic vdW radii. At short

distances where the interatomic distance is less than R_r the damping factor tends to zero

and the energy correction is negligible.

2.1.6 Band alignment in solids

The use of the HSE06 functional generally gives a more accurate description of

the allowed energy levels of the electrons in the system but one issue remains. The energy

levels obtained in DFT calculations provide only relative energy values with respect to

an internal reference, which is typically the average electron potential in the solid. To

obtain absolute energy levels, *i.e.* with respect to the vacuum potential, as is required to

assess the materials suitability as a photocatalyst, a procedure to align the bands is needed.

This work uses the method described by Butler *et al.*[82] where the vacuum level in porous

structures is estimated, based on calculating the potential at different positions within the

pores. In framework materials, the atoms and associated electrons are confined to the

framework and these generate an electrostatic potential. This electrostatic potential

reaches a plateau (a gradient of zero means no electric field) at a point far enough from

any atoms or electrons in the system. To determine the electrostatic potential at the centre

of the pore the spherical average is taken:

$$\Phi_{\text{av}}(\boldsymbol{r}) = \frac{1}{V} \int_V \Phi(\boldsymbol{r} + \boldsymbol{r}') d^3\boldsymbol{r}' \tag{2.29}$$

where V is a spherical region around $\boldsymbol{r}$. To validate the calculated spherical average

potential and check convergence the mean and variance of the values within the sphere

are also computed at a designated radius from the pore centre. Butler *et al.*[82] reported that,

in all cases they tested the variance fell to within 1×10^{-4} V. This method will be used in this work along different directions in the pore. Since the potential along the pore is periodic and continuous, there will always be at least two different points (one maximum and one minimum) of zero gradient. In each case the potential at the zero-gradient point that is farthest from the framework atoms is chosen as the vacuum potential.

2.2   Electron transport properties

Electronic structure calculations give the allowed energy levels of the electrons in the system at each point of the reciprocal space (electronic bands). This information can then be used to calculate the electron transport properties of the material. In this section, the theory behind obtaining the Seebeck coefficient (S), electronic conductivity (σ), and the electronic part of the thermal conductivity (κ_{el}) from the band structures are discussed.

2.2.1   Boltzmann transport equations

Electron transport in solids can be considered as electrons moving in a periodic potential created by the surrounding ions and other electrons. As the electron moves through the solid it can of course be scattered by various interactions. Scattering events occur by interactions with other electrons, interactions with lattice vibrations or standing waves known as phonons, interactions with impurities or even with magnetic spin waves known as magnons. At equilibrium, there is no net flow of electrons; electron velocity through diffusion will be balanced by the scattering events: The Fermi-Dirac distribution can be used to calculate the number of electrons with a given energy. In equilibrium at temperature T the Fermi-Dirac distribution function is

$$f_0 = \frac{1}{e^{\left(\frac{\varepsilon - E_F}{k_B T}\right)} + 1} \tag{2.30}$$

23

where E_F and k_B are the Fermi energy and Boltzmann's constant, respectively.[83] In the non-equilibrium distribution (f_k) the possible values of the electron wave vector k, depend on the electric field, the temperature gradient across the material and the electron's group velocity (v_k) and can be described by the Boltzmann transport equation (BTE).

$$\frac{\partial f_k}{\partial t} = -v_k \cdot \frac{\partial f_k}{\partial r} - \frac{e}{\hbar}\left(E + \frac{1}{c}v_k \times H\right) \cdot \frac{\partial f_k}{\partial k} + \frac{\partial f_k}{\partial t}\bigg|_{scatt} \tag{2.31}$$

The BTE (2.31) states the rate of change of the population with respect to time is dependent on diffusion, the effect of electric (E) or magnetic (H) fields, or scattering. The BTE is solved in the absence of a magnetic field and temperature gradients, giving a solution that relates a system out of equilibrium (f_k) to the equilibrium system (f_0).

$$f_k = f_0 + e\left(-\frac{\partial f_0}{\partial \mathcal{E}}\right)\tau_k v_k \cdot E \tag{2.32}$$

where τ is the relaxation time of the electron; that is the time that an electron moves freely between two successive collisions or the inverse of the scattering rate and is normally of the order of 10^{-14} s. The band index n is omitted here to make the expressions simpler but strictly speaking k should be replaced by (n,k) in all the indices. The electron's group velocity can be calculated from the gradient of the bands $\mathcal{E}(k)$ in k-space.[84] The group velocity and its distribution can also be related to the electrical current (J) as the summation of the group velocity multiplied its distribution and charge over all k-space leads to an expression for J.

$$J = e\sum_k f_k v_k \tag{2.33}$$

As the current J equals the conductivity multiplied by the electric field an expression for the conductivity can be obtained:

$$\sigma = \frac{J}{E} = e^2 \sum_k \left(-\frac{\partial f_0}{\partial \mathcal{E}}\right) \tau_k v_k{}^2 \qquad (2.34)$$

The electrical current for carriers (electrons or holes) can be obtained using the carrier's group velocity; which can be calculated from first principles as it is the gradient of the band energy with respect to k.

$$v_k = \frac{1}{\hbar} \frac{\partial \mathcal{E}_k}{\partial k} \qquad (2.35)$$

In this work the transport properties are given in terms of the transport distribution function (Ξ) which is given as a summation over all the bands ($\mathcal{E}_n$) integrated over all of k-space and dependent on direction.

$$\Xi = \sum_{k,n} v_{k,n}\, v_{k,n}\, \tau_{k,n} \approx \tau \sum_{k,i} v_{k,n}\, v_{k,n} \qquad (2.36)$$

where τ is the so-called relaxation time (time without collisions); $1/\tau$ is the scattering rate.[84-86] Treating the relaxation time as constant and moving it outside the summation is known as the constant relaxation time approximation. Using the transport distribution function the conductivity can then be expressed as:

$$\sigma = e^2 \int d\varepsilon \left(-\frac{\partial f_0}{\partial \mathcal{E}}\right) \Xi(\varepsilon) \qquad (2.37)$$

the Seebeck coefficient as:

$$S = \frac{e k_B}{\sigma} \int d\varepsilon \left(-\frac{\partial f_0}{\partial \mathcal{E}}\right) \Xi(\varepsilon) \frac{\varepsilon - \mu}{k_B T} \qquad (2.38)$$

where μ is the chemical potential and the electrical thermal conductivity at zero field can be expressed as:

$$\kappa_{\mathrm{el}}^0 = k_B^2 T \int d\varepsilon \left(-\frac{\partial f_0}{\partial \varepsilon}\right) \Xi(\varepsilon) \left[\frac{\varepsilon - \mu}{k_B T}\right]^2 \qquad (2.39)$$

To obtain the electrical thermal conductivity at zero current which is what is reported in experiment the following correction is necessary

$$\kappa_{\mathrm{el}} = \kappa_{\mathrm{el}}^0 - TS^2\sigma \qquad (2.40)$$

In metals the conductivity is high compared to semiconductors and insulators and the electrical conductivity also results in a high electrical thermal conductivity. In fact, in metals it has been shown that the ratio of the two are proportional to the absolute temperature:

$$\frac{\kappa_{\mathrm{el}}}{\sigma} = L_0 T \qquad (2.41)$$

where

$$L_0 = \frac{\kappa_{\mathrm{el}}}{\sigma T} = \frac{\pi^2 k_B^2}{3e^2} \approx 2.4453 \times 10^{-8} \; \mathrm{W\Omega K^{-2}} \qquad (2.42)$$

Equation (2.41) is known as the Wiedemann-Franz law and is generally valid at high temperatures where the scattering mechanisms are elastic. At low and intermediate temperatures where the carriers have insufficient energy to be elastically scattered and are instead scattered inelastically the Wiedemann-Franz law fails.[71, 83]

In order to solve the transport Equations (2.37-2.39) two terms must be calculated, the total relaxation time (τ) which is the inverse of the total scattering rate and the group velocity, these parameters are now discussed.

A. Scattering rates

According to Matthiessen's rule each scattering process is independent, and therefore the different contributions to the total scattering rate are additive. Taking into account the three main scattering processes, electronic scattering by impurities, phonons and electrons, scattering rates have a different dependence on temperature for metals and semiconductors.

In metals at very low temperatures, lattice vibrations cannot produce phonons with sufficient energy to scatter electrons, phonon scattering is negligible. The dominant electron-scattering mechanism in this temperature regime is impurities. Impurities have a different charge to the host, leading to electrons being elastically scattered by impurities (Rutherford scattering). Electrons that are scattered at very low temperatures are at the Fermi surface and have constant energy. Scattering events are therefore independent of temperature in this regime.

Around and above the Debye temperature (T_D), phonons will have sufficient energy to scatter electrons. As the number of phonons increase linearly with temperature, electron-phonon scattering increases linearly with temperature and is the dominant scattering mechanism in this temperature regime. Finally, in metals with a complicated Fermi surface or where there are a large density of states at the Fermi level electron-electron scattering may become significant and scattering rates are proportional to T^2. Around and above T_D, this leads to a polynomial expression for the total electron scattering in metals:

$$\frac{1}{\tau} = a_0 + a_1 T + a_2 T^2 \tag{2.43}$$

In the case of semiconductors, free carriers have a quasi-Boltzmann energy distribution, the average energy of the carriers varies with T. At T well below T_D, impurity

scattering dominates. The scattering cross-section is proportional to T^{-2}, scattering of electrons by impurities decrease with temperature. In contrast, the carrier's speed increases with temperature and is proportional to $E^{\frac{1}{2}}$, *i.e.* $T^{\frac{1}{2}}$ leading to:

$$\frac{1}{\tau} \alpha \frac{T^{-2}}{T^{-\frac{1}{2}}} = T^{-\frac{3}{2}} \tag{2.44}$$

Near and above T_D, as in the case with metals, the number of phonons are proportional to T. In contrast to metals, the carrier's energy is not constant but increases as a function of temperature, being proportional to $T^{\frac{1}{2}}$ leading to

$$\frac{1}{\tau} = \frac{T}{T^{-\frac{1}{2}}} = T^{\frac{3}{2}} \tag{2.45}$$

The total scattering rates can again be calculated as the sum of the individual scattering mechanisms,[71, 87] leading to an expression for non-degenerate semiconductors

$$\frac{1}{\tau} = a_0 T^{-\frac{3}{2}} + a_1 T^{\frac{3}{2}} + a_2 T^2 \tag{2.46}$$

B. Group velocity

The evaluation of the group velocity directly from Equation (2.35) is numerically difficult to implement.[84] The first computational techniques carried out to determine the group velocity involved relating the group velocity to the momentum and determining the coefficients at a zero field and was reported by Scheidemantel *et al.*[84] With increased computer power a new approach for evaluating the group velocity has been based on Fourier expansion of the band-energies which can then be analytically differentiated to obtain the group velocity.[86] This method was first reported using the BoltzTrap code by Madsen and Singh and implemented within WIEN2k.[86] The computational expense of

the calculation results from the need to calculate the group velocity on a fine $\boldsymbol{k}$-grid to accurately obtain the correct derivatives and avoid band crossings. This is certainly possible at the PBE level but where accurate band gaps are needed HSE calculations may need to be used. Calculations on high $\boldsymbol{k}$-grids using HSE functionals are currently still too computationally expensive. The alternative in this case is implementing the use of Wannier functions which are functions in real space and can readily interpolated from a coarse to a fine $\boldsymbol{k}$-grid in order to calculate transport properties.

2.2.2   Wannier functions

The electronic wavefunction for periodic solids is a Bloch function, Equation (2.18), described here with n as the band index:

$$\psi_{nk}(\boldsymbol{r}) = e^{ik.r} u_{nk}(\boldsymbol{r}) \tag{2.47}$$

The electronic wavefunction can also be represented in terms of a real space Wannier function (WF) for a specific band index, n and its associated unit cell $\boldsymbol{R}$[88-91]

$$w_{n\boldsymbol{R}}(r) = \frac{V}{(2\pi)^3} \int_{\text{BZ}} \psi_{nk}(\boldsymbol{r})\, e^{-ik.\boldsymbol{R}} d\boldsymbol{k} \tag{2.48}$$

where V is the volume of the cell. There exists a certain amount of freedom in the way one can choose u_{nk}. The transformation

$$u_{nk} \rightarrow e^{i\phi_n(\boldsymbol{k})} u_{nk} \tag{2.49}$$

is always valid and WFs with different spatial distributions are dependent on the choice of phase (ϕ). For an isolated set of bands, the choice of phase is the only possible freedom in changing the WF. For a (composite) set of bands, the transformation is more general and can be expressed as

$$u_{nk} \rightarrow \sum_{m=1}^{N} U_{mn}^{(k)} u_{mk} \tag{2.50}$$

where $U_{mn}^{(k)}$ is a unitary matrix that mixes Bloch states at wavevector k. Substituting the wavefunction ψ_{nk} in Equation (2.48) and expressing the periodic function using its unitary transform, Equation (2.50) the WF can be expressed as

$$w_{nR}(r) = \frac{V}{(2\pi)^3} \int_{BZ} \left[\sum_{m=1}^{N} U_{mn}^{(k)} \psi_{mk}(r) \right] e^{-ik.R} dk \tag{2.51}$$

In theory for each different R the same WF should be obtained; $w_{nR}(\mathbf{r}) = w_n(\mathbf{r}\text{-}\mathbf{R})$.[92] In practise any change in R leads to large oscillations in the calculated WF as it is an exponential term. Different choices of the unitary matrix lead to different WFs, so the WFs are not uniquely defined. Changes in the choice of the unitary transformation will change the spread or variance (Ω) of the unitary transform; but the expected mean of the WF should remain constant.

$$\Omega = \sum_{n=1}^{N} [\langle w_{n0}(r)|r^2|w_{n0}(r)\rangle - |\langle w_{n0}(r)|r|w_{n0}(r)\rangle|^2] \tag{2.52}$$

where the first term is the spatial localisation of the calculated WF and the second term is the expected mean, both are in Å^2. Maximally localised Wannier functions (MLWFs) can be obtained by minimisation of this spread. Marzari and Vanderbilt[93] minimized Ω based on a gradient approach by considering infinitesimal changes of unitary transformation of the Bloch orbitals. They show that the only information needed in calculating the gradient are the overlaps between the cell periodic part of the Bloch states

$$M_{mn}^{(k,b)} = \langle u_{mk} \mid u_{n,k+b} \rangle \tag{2.53}$$

where b are vectors connecting a k-point to its nearest neighbour. The spread is small whenever the magnitude of the square of overlaps between the Bloch states at neighbouring k-points is large. This part of the spread is known as the gauge invariant (Ω_I) spread, it is invariant with the choice of unitary transform. In fact, the total spread is the sum of two components:

$$\Omega = \Omega_I + \widetilde{\Omega} \tag{2.54}$$

where $\widetilde{\Omega}$ is the gauge-dependent term. $\widetilde{\Omega}$ is the result of the failure of the WFs to be eigenfunctions of the band-projected position operator in $3d$ real space.[93]

In semiconductors and metals where groups of bands are mixed or "entangled" together a further procedure known as the disentanglement method is used.[92] In this method a set of bands in a frozen energy window is selected. In this portion of the band structure the Bloch states and therefore the bands are forced to be preserved. In the outer energy window, the Bloch states can change depending on the choice of unitary transformation. At each k-point in the frozen window the Bloch states are mapped into another set of Bloch-like states from which the WF can be constructed. The bands are disentangled by taking scalar products along k-space. The more similar the bands are to one another the less the angle will change in k-space which leads to a greater scalar product.

The use of MLWFs to calculate electron transport properties is an alternative to calculating group velocities from solutions to the wavefunctions on a fine k-grid. The MLWFs can be calculated from wavefunctions on a coarse grid. The MLWF can be used to interpolate the band structure on a fine k-grid reducing computational costs. This is of particular importance when HSE06 calculations are required. In addition, it is possible to calculate the band derivative at any k-point from the derivative of the Wannier Hamiltonian and this procedure has been implemented in the BoltzWann code.[94]

2.3   Lattice dynamics

2.3.1   Phonon dispersion

The preceding Section (2.2) gave an introduction of the theory needed to calculate the electrical thermal conductivity (κ_{el}) of a material. In addition to κ_{el}, heat transfer can also occur through, lattice waves (phonons), electromagnetic waves, spin waves, or other excitations[83]. The sum of all these contributions yield the total thermal conductivity of the material. This section introduces the theoretical background used in calculating the lattice thermal conductivity (κ_{latt}) of a material. In the same way that electrons transfer heat by propagating through the system lattice vibrations can propagate heat through a material. In a metallic system electron and hole carriers are the dominant contribution to heat transfer; on the other hand, in insulators κ_{latt} is dominant. In the regime in the middle belonging to semiconductors both κ_{el} and κ_{latt} have significant contributions to heat transfer.

The heat dissipated through the system due to κ_{latt} is the sum of all wave packets which consist of various normal modes of vibrations or phonons at specific frequencies depending on the material.[83] This leads to dispersion curves of the phonon frequencies as a function of the wavevector denoted as q. If atoms move coherently in the solid this leads to acoustic modes of vibrations at low frequencies. This can happen in three directions which gives 3 acoustic modes for the solid. If the atoms move out of phase the result is optical modes at higher frequencies. In general, optical modes have low group velocities and do not contribute significantly to κ_{latt}, although they may affect heat transfer by interacting with acoustic phonons through phonon-phonon scattering.[83] Both acoustic and optical modes are the result of displacements of atoms of in the system and can be described as a harmonic oscillator. In fact, the potential energy of the system can be

32

evaluated exactly, the potential energy as a function of distance can be described analytically as a Taylor expansion:

$$V(x) - V(x_0) = \left.\frac{dV(x)}{dx}\right|_{x_0}^{x} (x - x_0) + \frac{1}{2!}\left.\frac{dV^2(x)}{dx^2}\right|_{x_0}^{x} (x - x_0)^2 + \cdots$$

$$+ \frac{1}{n!}\left.\frac{dV^n(x)}{dx^n}\right|_{x_0}^{x} (x - x_0)^n$$

(2.55)

The derivative of the potential energy with respect to position (the first term in the expansion) should be zero as there should be no force on the atom. The potential energy can then be determined by calculating only second or higher terms in the expansion. In the harmonic approximation, Equation (2.55) is simplified to only include the quadratic term and all higher terms are assumed to be insignificant. This can be referred to as the force or spring constants (analogous to Hooke's law). To obtain the second-order force constants this work uses the finite displacement method,[95] where one atom is displaced and the force on all the other atoms is calculated. It is also important to note that the displacement is assumed to be small compared to the interatomic distance.

It is necessary to use a supercell approach where more than one cell is used to accurately describe the forces, as if one atom is moved there will be a force exhibited on a neighbouring unit cell. These forces can be represented by a force constants matrix (Φ) also known as the Hessian matrix.

$$F_{\alpha i} = \sum_{\beta, j} -\Phi_{ij}^{\alpha\beta} r_{\beta j} = M_i \ddot{r}_{\alpha i}$$

(2.56)

where α and β are the co-ordinate system and i and j are the atoms in the system. The Hessian matrix is given in real space but can be represented in q-space by the dynamical matrix:

$$D_{\alpha\beta}(i,j,\boldsymbol{q}) = \frac{1}{\sqrt{M_i M_j}} \sum_{\boldsymbol{R}} \Phi_{ij}^{\alpha\beta}(0,\boldsymbol{R}) e^{[i\boldsymbol{q}.(r(\boldsymbol{R})-r(0))]} \tag{2.57}$$

where the sum is taken over atoms in the first unit cell (0) and neighbouring unit cells ($\boldsymbol{R}$). Diagonalizing the dynamical matrix gives solutions to the eigenvalue problem as the square root of the eigenvalues of the dynamical matrix give the phonon vibrational frequencies. The phonon dispersion curves (frequency *vs.* $\boldsymbol{q}$) provide the basis for a first model of heat transport, using Debye's equation for heat transfer:

$$\kappa_{\text{latt}} = \frac{1}{3} C v \lambda \tag{2.58}$$

where κ_{latt} is obtained from the specific heat capacity (C) of the acoustic phonon modes, the group velocity (v) and the average mean free path (λ) is of the modes, which is the average distance travelled before a scattering event. The heat capacity at constant volume (C_v) is the change in internal energy of the phonon modes with respect to the change in temperature.[96] It is expressed as an integral over frequency and phonon band index (n) and its temperature dependence is represented by $k_B T$ giving

$$C_V = \left(\frac{\partial E}{\partial T}\right)_V = \sum_{n,\boldsymbol{q}} k_B \left(\frac{\hbar\omega(n,\boldsymbol{q})}{k_B T}\right)^2 \frac{e^{\left(\frac{\hbar\omega(n,\boldsymbol{q})}{k_B T}\right)}}{\left[e^{\left(\frac{\hbar\omega(n,\boldsymbol{q})}{k_B T}\right)} - 1\right]^2} \tag{2.59}$$

At very low temperatures well below the Debye temperature it can also be expressed as

$$C_v = 9Nk_B x^{-3} \int_0^x \frac{x^4 e^x}{(e^x-1)^2} dx \approx \frac{12\pi^4}{5} Nk_B \left(\frac{T}{T_D}\right)^3 \tag{2.60}$$

where N is the number atoms per unit cell, $x = \frac{T_D}{T}$, $T_D = \frac{h v_D}{k_B}$, T_D is the Debye temperature and v_D is the Debye cutoff frequency of the normal modes.[83] Alternatively

the equation can also be expanded to sum over each phonon mode and in each direction. The mean free path can be replaced with the phonon's group velocity multiplied by its relaxation time:

$$\kappa_{\text{latt}} = \frac{1}{3} \sum_n \int \frac{d\boldsymbol{q}}{8\pi^3} \, v_{n,\boldsymbol{q}}^2 \, \tau_{n,\boldsymbol{q}} C(\omega_{n,\boldsymbol{q}}) \qquad (2.61)$$

where the sum is over all the phonon bands and the integral is over all the $\boldsymbol{q}$ points in the Brillouin zone; $v_{n,\boldsymbol{q}}$ is the group velocity of a given phonon mode, $\tau_{n,\boldsymbol{q}}$ is the mode relaxation time and C is the mode heat capacity depending on the mode frequency $\omega_{n,\boldsymbol{q}}$ and the temperature.[96] To accurately determine κ_{latt} the relaxation time of each phonon mode needs to be calculated and is governed by the scattering of a phonon by other phonons.

If there were no phonon-phonon interactions and no scattering of phonons, heat transfer would be instantaneous and this is the result from the harmonic approximation. Scattering of phonons by other phonons as well as electrons play a vital role in thermal conductivity. This part of the theory describes the calculation of third order force constants and phonon-phonon scattering rates to calculate the lattice conductivity. Only phonon-phonon scattering rates are calculated, electron-phonon scattering rates are ignored. To calculate phonon-phonon interactions the potential energy of the crystal given in Equation (2.55) must be expanded to the cubic term. This term is referred to as the anharmonic force constants and takes into account the anharmonicity of the phonons.

2.3.2 Anharmonic behaviour and transport

Phonon-phonon scattering can occur by two processes: normal and Umklapp scattering events. When an Umklapp process occurs the total crystal momentum is not conserved, as a result the process is resistive. In a normal process, there is no net change

in crystal momentum and there is little contribution to heat flow (Figure 2.2). Normal processes do however lead to the transfer of energy between modes and a net flow of heat, acting to restore the equilibrium distribution.

(a) Normal process

(b) Umklapp process
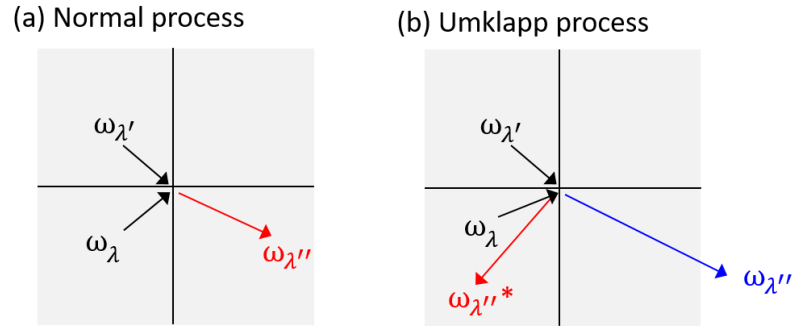
Figure 2.2. Absorption of two phonons ω_λ and $\omega_{\lambda'}$ to form one phonon $\omega_{\lambda''}$ in (a) a normal process where $\omega_{\lambda''}$ remains in the first BZ (shaded in grey) with no change in phonon momentum and in (b) where the absorbed phonon $\omega_{\lambda''}$ has the required momentum to leave the first BZ. $\omega_{\lambda''}$ which can be represented again in the first BZ ($\omega_{\lambda''}$*)

In a similar way to which Boltzmann theory was used to calculate electron transport in Section 2.2.1, it is used here to calculate phonon transport. It is important to note one difference related to the distribution of phonons. The phonon energy distribution follows Bose-Einstein rather than the Fermi-Dirac statistics, as described by Equation (2.30). Phonon have integer spins and are not restricted by the Pauli exclusion principle, which leads to the following distribution.

$$f_0 = \frac{1}{e^{(\frac{\varepsilon - \hbar\omega}{k_B T})} - 1}$$

(2.62)

where again f_0 is the equilibrium distribution. In f_0 the rate of scattering equals the rate of diffusion and there is not net heat transfer. In the presence of a temperature gradient, the BTE assumes the non-equilibrium distribution (f_λ) which is restored to f_0 by scattering

events. These are proportional to deviation from equilibrium given by the phonons group velocity and temperature gradient.[83, 97]

$$\left(\frac{\partial f_\lambda}{\partial t}\right)_{\text{scattering}} = \frac{f_\lambda - f_0}{\tau_{n,q}} = -(v.\nabla T)\frac{\partial f_0}{\partial T} \tag{2.63}$$

The single mode relaxation time approximation used in thermal conductivity calculations assigns a relaxation time to each phonon mode.[98] The flux carried by all the phonons is

$$Q = \sum_{n,q} f_\lambda \hbar\omega_{n,q} v_{n,q} \tau_{n,q} \tag{2.64}$$

Multiplying Equation (2.63) through by the relaxation time and expressing it in terms of f_λ, which can be substituted into Equation (2.64), leads to an expression for $\kappa_{\text{latt.}}$ κ_{latt} is the flux per unit of temperature difference and per metre across the material:

$$\kappa_{\text{latt}} = \frac{Q}{\nabla T} = \frac{1}{3}\sum_{n,q} \hbar\omega_{n,q} v_{n,q}^2 \tau_{n,q} \frac{\partial f_0}{\partial T} \tag{2.65}$$

It is possible, with currently available codes, to treat phonon transport at a higher level of theory than electron transport, in the sense that it is possible to calculate the relaxation times for each phonon mode.[97, 99] The ShengBTE code considers ∇T to be small. This assumption allows the deviation to the equilibrium distribution denoted as g_λ to be expanded linearly $f_\lambda = f_0 + g_\lambda$, giving

$$g_\lambda = -F_\lambda.\nabla T\frac{df_0}{dT} \tag{2.66}$$

F_λ has units of distance and within the relaxation time approximation (RTA) it is the mean free path of the phonon; which is the relaxation time of the mode multiplied by its velocity. When two and three-phonon processes are considered there is deviation from the RTA as new phonon modes can be created through emission processes (two phonons interacting

to form three phonons) or absorption processes (two or three phonons interactions leading to the absorption of a phonon. This deviation is represented by and additional term $\mathbf{\Delta}_\lambda$

$$\mathbf{F}_\lambda = \tau_\lambda^0 (\mathbf{v}_\lambda + \mathbf{\Delta}_\lambda) \tag{2.67}$$

$\mathbf{\Delta}_\lambda$ in turn depends on absorption (Γ^+) and emission (Γ^-) scattering rates but also on $\mathbf{F}_\lambda$ and therefore must be solved in an iterative manner.

$$\begin{aligned}
\mathbf{\Delta}_\lambda = \frac{1}{N} \sum_{\lambda'\lambda''}^{+} \Gamma_{\lambda\lambda'\lambda''}^{+} \left(\frac{\omega_{\lambda''}}{\omega_\lambda} \mathbf{F}_{\lambda''} - \frac{\omega_{\lambda'}}{\omega_\lambda} \mathbf{F}_{\lambda'} \right) \\
+ \frac{1}{N} \sum_{\lambda'\lambda''}^{-} \Gamma_{\lambda\lambda'\lambda''}^{-} \left(\frac{\omega_{\lambda''}}{\omega_\lambda} \mathbf{F}_{\lambda''} + \frac{\omega_{\lambda'}}{\omega_\lambda} \mathbf{F}_{\lambda'} \right) \\
+ \frac{1}{N} \sum_{\lambda'} \Gamma_{\lambda\lambda'} \left(\frac{\omega_{\lambda'}}{\omega_\lambda} \mathbf{F}_{\lambda'} \right)
\end{aligned} \tag{2.68}$$

where ω_λ is the angular frequency of the phonon mode. The third term in Equation (2.68) represents a scattering contribution from isotope disorder. As scattering rates are independent events (Matthiessen's rule) the total scattering rate can be expressed as the sum of all contributions.

$$\frac{1}{\tau_\lambda^0} = \frac{1}{N} \left(\sum_{\lambda'\lambda''}^{+} \Gamma_{\lambda\lambda'\lambda''}^{+} + \sum_{\lambda'\lambda''}^{-} \frac{1}{2} \Gamma_{\lambda\lambda'\lambda''}^{-} + \sum_{\lambda'} \Gamma_{\lambda\lambda'}^{-} \right) \tag{2.69}$$

where N is the number of $\mathbf{q}$-points on the sampled grid in the Brillouin zone. Scattering rates are calculated from the scattering matrix elements and represent scattering probabilities in going from the initial state to a final state for each of the allowed three phonon processes. These depend on the normalised eigenfunctions of the three phonons involved and the anharmonic third order force constants:

$$\phi_{ijk}^{\alpha\beta\gamma} = \frac{\partial^3 E}{\partial r_i^\alpha \partial r_j^\beta \partial r_k^\gamma} \tag{2.70}$$

where i,j,k represent atomic indices, α,β,λ are Cartesian coordinates. i runs over the central unit cell but j and k cover the whole system. Obtaining the third order force constants means going further than the harmonic approximation given in Equation (2.55) and continuing the expansion of the potential energy of the system to the cubic term. Again, the finite displacement method is used. Each atom is displaced and the force felt on all other atoms is calculated. To accurately calculate the force felt by each atom due to a displacement of a neighbouring atom a supercell approach is used to include the full set of forces. To reduce the number of interatomic force constants calculated only those that are symmetrically inequivalent configurations are considered. This is implemented in the thirdorder.py program.[100]

These calculations can then be used in the calculation of the lattice thermal conductivity which is expressed in terms of $\boldsymbol{F}_\lambda$.

$$\kappa_{\text{latt}}^{\alpha\beta} = \frac{1}{k_B T^2 \Omega N} \sum_\lambda f_0(f_0 + 1)(\hbar\omega_\lambda)^2 v_\lambda^\alpha F_\lambda^\beta \tag{2.71}$$

in Equation (2.67), $\boldsymbol{F}_\lambda$ is given as the deviation from the mean free path in the RTA. The deviation from the RTA and the corresponding extra contribution to κ_{latt} can be attributed to normal processes. In the RTA, normal processes are considered resistive and do not contribute to heat transport. This is generally the case and the deviation from the RTA is typically less than 10%.[98] In some systems such as diamond normal processes are significant and increase κ_{latt} by redistributing energy to other phonon modes, in such systems the RTA underestimates κ_{latt}.

2.4 Configurational disorder

Doping in solid solutions presents the added problem of generating a large number of possible configurations and increased computational analysis. To reduce the number of configurations modelled, the computer program Site Occupancy Disorder (SOD) can be used.[101] The method takes into account crystal symmetry and allows the number of possible configurations to be reduced by considering two configurations equivalent if they are related by an isometric operation.[101] These are geometric operations (*e.g.* translations, rotations or reflections) that keep all the angles and distances constant within the transformed object.

Using the crystallographic point group of the parent structure all the possible configurations are generated using matrix transformations. For a cell composition with n substitutions there would be $N_s!/n!(N_s-n)!$ possible configurations, where N_s is the total number of sites where substitutions can take place. The program then extracts only the symmetrically inequivalent configurations.

Each composition has a corresponding configurational energetic spectrum and its probability of occurrence is a weighted mean which can be described by a Boltzmann-like probability. It is calculated assuming zero external pressure and ignoring vibrational contributions, from the lattice energy E_m.[100,102]

$$P_m = \frac{\Omega_m}{Z} e^{\left(\frac{-E_m}{k_B T}\right)} \tag{2.72}$$

where $m = 1,..,M$ (M is the number of inequivalent configurations), Ω_m is the number of times that the configuration is repeated in the complete configurational space, k_B is the Boltzmann's constant, and Z is the configurational partition function which guarantees the sum of all the probabilities equals one.

$$Z = \sum_{m=1}^{N} \Omega_n e^{\left(\frac{-E_m}{k_B T}\right)} \qquad (2.73)$$

For any property investigated, it is possible to obtain a weighted average (A) based on its probability of occurrence of each configuration:

$$A = \sum_{m} P_m A_m \qquad (2.74)$$

SOD also allows an insight into the thermodynamics of the solid solutions. In these systems, the enthalpy of each configuration is simply its lattice energy, since zero external pressure is assumed and vibrational contributions to the enthalpy are ignored. The enthalpy per formula unit (H) at each composition is calculated as an average in the configurational space:

$$H = \frac{1}{N} \sum_{m=1}^{N} P_m H_m \approx \frac{1}{N} \sum_{m=1}^{N} P_m E_m \qquad (2.75)$$

where N is the number of formula units in the supercell. The configurational free energy can be obtained from the partition function as[100,102]

$$G = -\frac{1}{N} k_B T \ln Z \qquad (2.76)$$

The enthalpies of mixing for the system can be obtained by calculating the enthalpies of the pure systems and calculating the difference based on the weighted average over all the configurations.

3   Shandites

The electronic structure and transport properties of nonmagnetic $Ni_3Sn_2S_2$ and magnetic $Co_3Sn_2S_2$ are presented in this chapter as representatives of shandite family of chalcogenides. The effect of disorder on the electronic structure of $Co_3Sn_{2-x}In_xS_2$ solid solutions are also investigated. All computational work presented here has been performed by myself. The experimental work on $Ni_3Sn_2S_2$ has been performed by my PhD colleague Panagiotis Mangelis and the experimental work on $Co_3Sn_2S_2$ and disorder in $Co_3Sn_{2-x}In_xS_2$ solid solutions has been performed by a previous PhD student in Prof. Powell's group, Dr Jack Corps.

3.1   Introduction

A group of layered metal chalcogenides with the formula $A_3M_2X_2$ (A = Ni, Co, Rh, Pd, M = Pb, In, Sn, Tl, X = S, Se) adopts the shandite mineral structure.[3, 103, 104] The shandite structure, with $R\bar{3}m$ symmetry, consists of sheets of metal atoms (both A and M) in the form of a Kagome-like hexagonal network and stacked in an ABC sequence. The A site in the Kagome layer forms corner sharing A_3 triangles each of which is capped above or below by X atoms. The M site in the Kagome layer is in hexagonal 6-fold coordination to the A atoms. In between the A_3 triangles (between the layers) there is a second interlayer M site with antiprismatic geometry (Figure 3.1).[105]
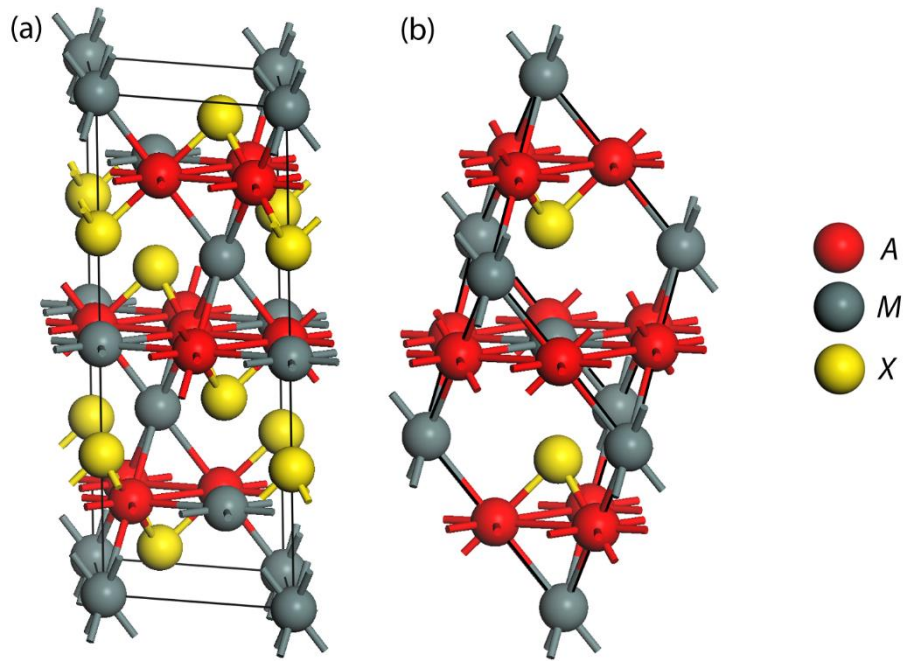
Figure 3.1. Hexagonal (a) and rhombohedral (b) unit cell of the shandites structure $A_3M_2X_2$ (A = Ni, Co, Rh, Pd, M = Pb, In, Sn, Tl).[105]

Shandites exhibit interesting electronic and magnetic properties including superconductivity $NiBi_2S_2$,[106] as well half-metallic ferromagnetism in $Co_3Sn_2S_2$.[107] $Co_3Sn_2S_2$ orders ferromagnetically with a Curie temperature of 177 K[107, 108] and a magnetic moment of 0.29 μ_B per Co atom at 5K as obtained by Vaqueiro *et al*,[104] also in agreement with experiments by Schnelle *et al*.[107] Interestingly, even at very low concentrations of Ni in $Co_{3-x}Ni_xSn_2S_2$, the Curie temperature is dramatically reduced with respect to $Co_3Sn_2S_2$. At $x > 0.2$ the compound becomes paramagnetic,[109] with the pure Ni phase being non-magnetic.[103] $Co_3Sn_2S_2$ is classified as a I_A half metal with its band gap in its minority spin channel.[107, 110] There is also some debate about the formal oxidation states of the constituent elements of these shandites. Gütlich *et al*.[103] report the nickel analogue as $Ni^0{}_3Sn^{2+}{}_2S^{2-}{}_2$, whereas in $Co_3Sn_2S_2$ and its substituted derivative Co_3SnInS_2, Sn has been reported as zero-valent.[111] Umetani *et al*.[112] report cobalt as mixed-valence

(Co(0), Co(II)) in $Co_3Sn_2S_2$, while Skinner *et al.*[113] conclude that zero-valent nickel is present in $Ni_3Pb_2S_2$.

Metal-semiconductor transitions which have been reported in $Co_3Sn_{2-x}In_xS_2$ ($0 \leq x \leq 2$) at around $x \approx 1.05$ show large changes in the Seebeck coefficient.[3] This may be due to the electron count[3] of this system and / or structural effects.[108, 111, 114] The pure Sn phase ($Co_3Sn_2S_2$) has an electron count of 47 per formula unit, compared to that of the In phase $Co_3In_2S_2$ with an electron count of 45 with both phases exhibiting metallic behaviour. At the mid-point of the series, Co_3SnInS_2 there is a metal-semiconductor transition.[114] The metal-semiconductor transition may also be due to structural disorder in the solid solutions.[114] Structural effects caused by In/Sn disorder are experimentally not easy to resolve as they cannot be easily distinguished by X-rays, neutron diffraction is required.[104, 115] Fujioka *et al.*[116] investigated Se doping of $Co_3SnInS_{2-y}S_y$ and report at $y \geq 0.6$ metallic behaviour is observed with an increase in electrical conductance but without the suppression of the Seebeck coefficient. They suggest Se doping results in stabilisation of In in the Kagome plane suggesting configurational disorder has a profound effect on the shandites properties in the solid solutions.

Understanding the reasons behind the electronic and magnetic properties of these systems is of importance to tuning their functionality especially for their use as candidate thermoelectric materials, where metal-semiconductor transitions lead to large changes in transport properties.[3, 117] The shandite systems typically contain heavy metal ions that may act as phonon scattering sites to limit its lattice thermal conductivity. Its constituents are also relatively cheap and abundant elements reducing the commodity price risk seen with rare elements.

This Chapter first discusses the electron and phonon transport properties of $Ni_3Sn_2S_2$ as a representative of the shandite family. Contrasting with the magnetic nature of Co shandites, $Ni_3Sn_2S_2$ has a nonmagnetic ground state, which has been confirmed by band-structure calculations and photoelectron spectroscopy,[103] as well as by direct magnetic susceptibility measurements.[109] The absence of magnetism in $Ni_3Sn_2S_2$ makes this compound a convenient starting point for the investigation of transport phenomena and thermoelectric behaviour in shandites. In contrast the Co shandites where the presence of spin polarization and magnetic excitations complicates the calculation of transport coefficients and the theoretical description of electron scattering, as electron-magnon interactions have to be taken into account.[118, 119]

3.2   Computational details

3.2.1   DFT calculations

Crystal structures were optimized using DFT calculations as implemented in the Vienna Ab initio Simulation Package (VASP).[120, 121] The projector augmented wave method was used,[73, 74] with electron levels up to Ni $3p$, Co $3p$, Sn $4p$, In $4p$, and S $2p$ kept frozen at their reference atomic state. The exchange correlation functional of Perdew-Burke-Ernzerhof (PBE),[69] based on the generalized gradient approximation (GGA), was employed. The number of plane waves was determined using a kinetic energy cutoff of 350 eV (30% above the highest of the standard values for the given set of elements) to ensure Pulay stress errors were minimized. Reciprocal space integrations were performed on a Gamma-centred grid of k-points with the smallest permitted spacing between them set to 0.3 Å^{-1}, which corresponded to a $7 \times 7 \times 7$ grid on the reciprocal lattice of the primitive cell ($Ni_3Sn_2S_2$) and a $5 \times 5 \times 2$ on the reciprocal of the 21-atom hexagonal unit-cell ($Co_3Sn_{2-x}In_xS_2$ with $0 \leq x \leq 2$). Test calculations showed that doubling the number of k-points in each direction led to total energy changes of less than 1 meV per formula unit.

For $Ni_3Sn_2S_2$, spin-polarized calculations were performed with different initializations of the magnetic moments but the calculations always converged to a nonmagnetic ground state, as expected from previous research.[103] The ionic positions were relaxed until the forces were less than 0.01 eV $Å^{-1}$ on each atom. A Bader analysis[122] of the charge density from VASP was performed using the code by Henkelman and coworkers.[123, 124]

Since the GGA often gives a poor description of the behaviour of d electrons in transition metal compounds, optimisation was also tested by including a Hubbard-type correction (PBE+U method) on the Co $3d$ orbitals (following Dudarev's approach[75] with an effective Hubbard parameter $U = 3.5$ eV, as used previously in mixed Co sulphides[125]). However, the uncorrected PBE results were in better agreement with experiment than the PBE+U results and therefor no U correction was used for subsequent calculations.

The disordered $Co_3Sn_{2-x}In_xS_2$ ($0 \leq x \leq 2$) phases were represented by a symmetry adapted ensemble of configurations, using the methodology implemented in the SOD (Site Occupancy Disorder) program,[101] and described in 2.4. Fractional site occupancies were calculated as average values over the ensemble.

The charge associated with each atom was calculated based on Bader analysis, which partitions the charge density in regions associated with each atom. Atoms are divided by the use of zero flux surfaces where the charge density is zero perpendicular to the surface which is found between atoms in a molecular system.[122]

3.2.2 Electron transport calculations

As a starting point for the electronic transport calculations, the band structure was recalculated using the WIEN2k code.[72] For this calculation, the Brillouin zone was sampled with a fine k-grid of $50 \times 50 \times 50$ points. For the basis set expansions the cutoff

parameters $l_{max} = 10$ and $R_{mt}K_{max} = 7$, while for the charge-density Fourier expansion the cutoff $G_{max} = 12$ was used; all these parameters were checked for convergence of the total energy. The radii of the muffin-tin spheres were set at the default values of 2.26, 2.50, and 1.85 bohrs for Ni, Sn, and S, respectively. For the $Co_3Sn_2S_2$ phase which is paramagnetic, spin-polarised calculations where performed in the ferromagnetic configuration on the primitive cell, again using the primitive cell with a fine k-grid of 50 × 50 × 50 points. Additionally, calculations were performed in the antiferromagnetic configuration using a 1 × 1 × 2 supercell of the conventional cell with 42 atoms to allow for equal up and down spins. In this case the Brillouin zone was sampled with a k-grid of 37 × 37 × 6 k-points which showed convergence.

The transport coefficients were then obtained from the bands by solving the linearized Boltzmann transport equation using the BOLTZTRAP code,[86] which interfaces with the WIEN2k output. BOLTZTRAP obtains the transport coefficients as functions of the electron chemical potential and temperature. Both the electrical conductivity (σ) and the electronic contribution to the thermal conductivity are calculated relative to the relaxation time (τ), which is assumed to be isotropic and constant in the reciprocal space at each temperature. Whereas the Seebeck coefficient can be calculated on an absolute scale, *i.e.*, it is independent of τ. The temperature variation of τ is discussed based on the comparison with experimental measurements of the electrical conductivity. At each temperature, the equilibrium value of the chemical potential corresponding to the undoped system, which deviates only slightly from the Fermi level. The effects of (dilute) doping are also considered by evaluating the transport coefficients and ZT at different chemical potentials corresponding different concentrations of electron excess or deficiency.

3.2.3 Phonon transport calculations

For the $Ni_3Sn_2S_2$ phase κ_{latt} was calculated by solving the Boltzmann transport equation using the method implemented in the ShengBTE code,[97, 99] which provides a full iterative solution. The second-order (harmonic) and third-order (anharmonic) force constants were obtained by the finite-displacement method, using energies from VASP calculations in a $3 \times 3 \times 3$ supercell of the primitive cell. The phonon dispersion curves and heat capacity were obtained from the second-order force constants using the PHONOPY code.[126] For the efficient calculation of the anharmonic force constants, harnessing the crystal symmetry, the thirdorder.py script was employed.[100] This required the evaluation of the DFT energies of only 364 configurations of atom displacements. The ShengBTE calculations were performed using a q-point grid of $13 \times 13 \times 13$, which was tested for convergence.

3.3   Results and discussion

3.3.1   Nonmagnetic Ni₃Sn₂S₂

C.   Crystal structure

While there is no debate that the $Co_3Sn_{2-x}In_xS_2$ crystalizes in the $R\bar{3}m$ spacegroup[3, 104, 108, 111] the $Ni_3Sn_2S_2$ has also been reported in the $C2/m$ spacegroup[127] as well as the $R\bar{3}m$ spacegroup[128]. XRD analysis performed by Panagiotis Mangelis confirmed that $Ni_3Sn_2S_2$ crystallizes in the rhombohedral space group $R\bar{3}m$ and the lattice parameters obtained from the DFT optimization are in good agreement with experiment, and with literature values[128] (Table 3.1). The small overestimation of the lattice parameters is typical of GGA-PBE calculations of metallic systems.[129] Another source of discrepancy is that the DFT results are obtained by minimization of the total energy at zero temperature (or more precisely, without considering vibrational effects, as zero-point effects were not included either), while the reported experimental parameters were measured near room temperature (293 K in this work and 297 K).[128] Still, the discrepancies are very small (+1.4% for a and +0.15% for c).

Table 3.1. Comparison of theoretical and experimentally determined crystal parameters of $Ni_3Sn_2S_2$. $z[S]$ is the z fractional coordinate of the S atom in special position 6c (0, 0, z) of space group $R\bar{3}m$

Parameter	This work		Ref. [128] Experiment
	DFT	Experiment	
a (Å)	5.540	5.46771(7)	5.4606(2)
c (Å)	13.208	13.1922(2)	13.188(1)
V (Å³)	351.06	341.55	340.56
$Z[S]$	0.2792	0.2820(2)	0.2820(2)

D. Electronic structure

The electronic band structure between high-symmetry points is shown in Figure 3.2. $Ni_3Sn_2S_2$ has a nonmagnetic metallic ground state with a low density of states at the Fermi level. The projection of the density of states on the Ni $3d$ orbitals shows that these contributions are almost completely below the Fermi level, which indicates a Ni^0 formal oxidation state with a $3d^{10}$ configuration.

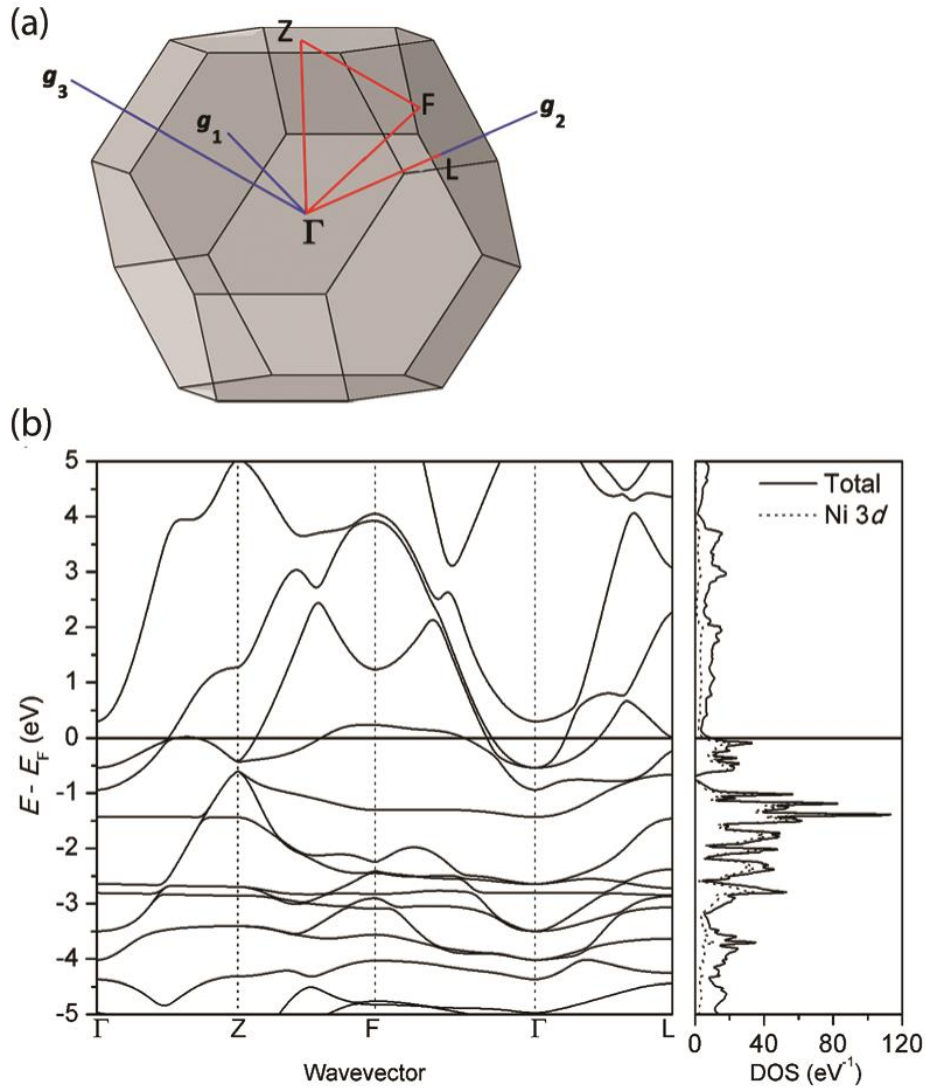**Figure 3.2. (a) First Brillouin zone of $Ni_3Sn_2S_2$ (rhombohedral setting), showing the high-symmetry k points Γ (0,0,0), Z (0.5,0.5,0.5), F (0,0.5,0.5), and L (0,0.5,0) used to plot the band structure. (b) Calculated band structure along high-symmetry paths and the corresponding density of states (both total and projected on the Ni $3d$ states).**

The 4s orbitals are about 5 eV above the Fermi level. The 3d^{10} configuration is typical of Ni^0 in inorganic molecular compounds like Ni(CO)$_4$.[130, 131] Bader analysis results are shown in Table 3.2 along with their electronegativity values on the Pauling scale. The results for the Co phases are also included in the table and are discussed in the following section. The neutral state of Ni seen in the density of states is consistent with the Ni Bader analysis. The Ni^0 valence state and the nature of the ground state are also in agreement with the findings in Ref. [103].

The magnitudes of the charges associated with the Sn and S atoms (±0.6–0.7) are also well below what would be expected from formal oxidation states, but still significantly different from zero: they are in between the values obtained for SnS (a polar covalent compound) and SnSb (an intermetallic compound). These results are in agreement with photoelectron spectroscopy and consistent with Mössbauer spectroscopy.[103, 113]

Table 3.2. Bader charge analysis of the shandite end member phases, the intermediate phase Co$_3$SnInS$_2$ at its most stable configuration and the calculations for SnS and SnSb are shown for comparison. Electronegativity values on the Pauling scale are also shown.

Atom (Electro-negativity)	Co (1.88)	Ni (1.91)	Sn (1.96)	In (1.78)	S (2.58)	Sb (2.05)
Ni$_3$Sn$_2$S$_2$	-	+0.05	+0.64	-	-0.71	-
Co$_3$Sn$_2$S$_2$	+0.04	-	+0.64	-	-0.70	-
Co$_3$In$_2$S$_2$	+0.03	-	-	+0.64	-0.69	-
Co$_3$SnInS$_2$	+0.06	-	+0.58	+0.67	-0.71	-
SnS	-	-	+0.96	-	-0.96	-
SnSb	-	-	+0.36	-	-	-0.36

E. Seebeck coefficient

Within the constant relaxation-time approximation [$\tau(k) = \tau$] in Boltzmann's transport theory, the Seebeck coefficient can be fully predicted from the DFT band structure, without introducing any empirical parameters. Therefore, the Seebeck coefficient constitutes a good test to the quality of the theoretical model. As the calculations were performed in the rhombohedral (**R**) setting a transformation was required to obtain the tensors in the hexagonal setting (**H**) and investigate any anisotropy.

$$[\mathbf{T}]_H = \mathbf{P}^{-1}[\mathbf{T}]_R\mathbf{P} \tag{3.1}$$

where

$$P = \begin{bmatrix} 0 & -1 & 1 \\ 1 & 0 & 1 \\ -1 & 1 & 1 \end{bmatrix}$$

Obtaining the Seebeck tensors in the hexagonal setting:

$$S = \begin{bmatrix} S_{xx} & 0 & 0 \\ 0 & S_{xx} & 0 \\ 0 & 0 & S_{zz} \end{bmatrix}$$

very little anisotropy is seen (e.g., $S_{zz}/S_{xx} = 0.992$ at 300 K). Since the crystal structure of shandites is clearly anisotropic, this result might seem a bit surprising, but it is noted that nearly isotropic Seebeck coefficients have been reported for other anisotropic crystals including Bi_2Te_3[132] and $SnSe_2$,[133] at specific ranges of temperatures and doping levels. This behaviour probably results from cancellations of different contributions to the anisotropy. It is worth noting here that the theoretical model assumes the relaxation time is fully isotropic. However, in some cases, the differences in scattering rates in different directions may be an additional source of anisotropy,[134] which has been ignored. Since there are no experimental data on single crystals to confirm the presence/absence of

anisotropy, the focus is on the calculated spherical average of the Seebeck coefficient, which can be compared to the experimental measurements in the polycrystalline material. The comparison between experimental and theoretical results is shown in Figure 3.3. Two sets of experimental results are reported, which were obtained using two different instruments (one for measurements below and the other for measurements above room temperature).
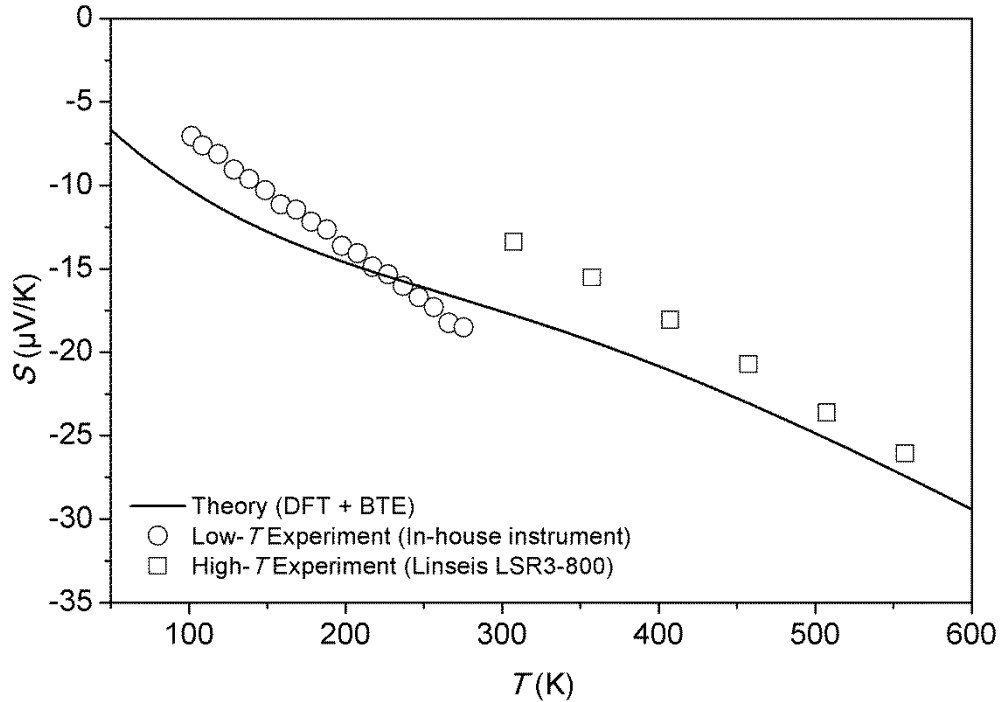
Figure 3.3. Experimental and theoretical Seebeck coefficients as functions of temperature.

The discontinuity at room temperature arises from the use of different instruments, and not from physical effects. For the whole range of temperatures there is excellent agreement between theory and experiment. $Ni_3Sn_2S_2$ exhibits a negative Seebeck coefficient with the absolute value increasing almost linearly with temperature.

F.   Electronic conductivity and scattering rates

In contrast to the Seebeck coefficient, the electronic conductivity can only be predicted per unit of relaxation time, *i.e.*, at this level of theory we can only calculate the ratio σ/τ. There have been some recent methodological developments for the calculation

53

of electron-phonon relaxation times from first principles,[135, 136] but the algorithms are not very mature yet and quite computationally demanding. By combining the theoretical results with the experimental measurements of electronic conductivity, the isotropic relaxation time as a function of temperature can be obtained. The σ/τ ratio has only a weak temperature dependence Figure 3.4a. For example, increasing the temperature from 400 to 500 K leads to an increase of less than 3% in the value of σ/τ. In Figure 3.4b the scattering rates $(1/\tau)$ required to exactly match the experimental conductivities as a function of temperature are shown. Figure 3.4c shows the experimental value of σ at room temperature is 2.4×10^6 S m^{-1} and decreases with temperature as expected for a metallic system. The scattering rates determined in this way increase linearly with temperature. This result can be interpreted in terms of Matthiessen's rule, according to which the total scattering rate is the sum of contributions from electron-electron scattering (proportional to T^2), from electron-phonon scattering (proportional to T above the Debye temperature of the material), and from impurity scattering (approximately independent of T).[87]
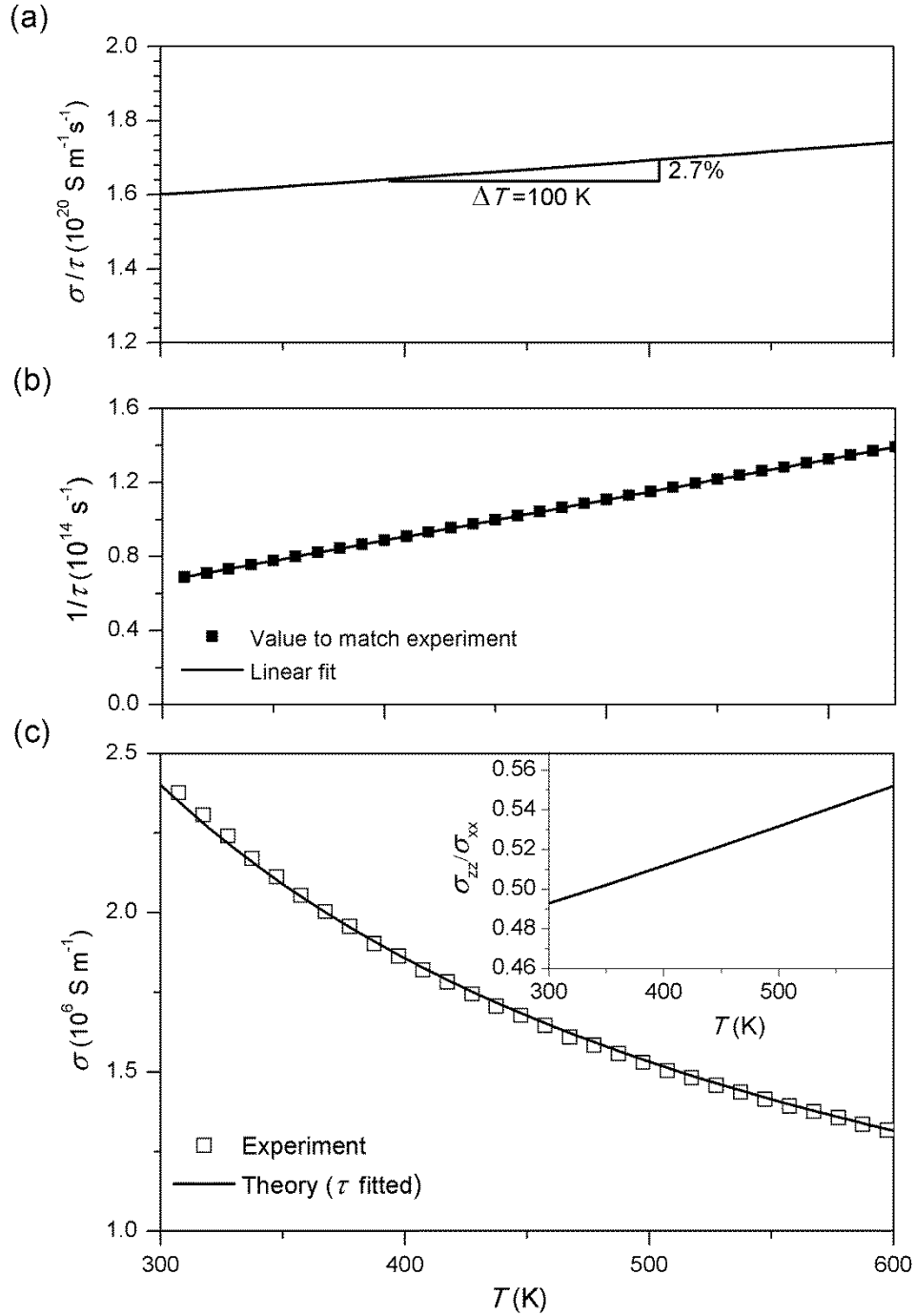
Figure 3.4. (a) Calculated electronic conductivity per unit of relaxation time (σ/τ). (b) Electron-phonon scattering rates obtained using the experimentally determined σ and the theoretically obtained σ/τ, and linear fitting of its temperature dependence. (c) Experimental electronic conductivity data and calculated values using fitted τ (T). The inset shows the ratio between the zz and xx components of the conductivity tensor.

In this case, given the linearity of the dependence it is clear that the electron-electron term can be omitted and the variation can be well fitted with the linear equation

$$\frac{1}{\tau} = a_0 + a_1 T \tag{3.2}$$

for which we obtain $a_0 = 9.82 \times 10^{11}$ s^{-1} and $a_1 = 2.19 \times 10^{11}$ s^{-1} K^{-1}. The electron-phonon

term dominates at the temperatures of interest here. For example, at 300 K the impurity

contribution represents less than 1.5% of the total scattering rate, and this reduces to 0.7%

at 600 K. The calculated relaxation time of 1.5×10^{-14} s at 300 K is reasonable and of the

same order as values obtained by the same procedure in other materials (e.g., for

Bi$_2$Te$_3$).[137] The linear dependence of the electron-phonon scattering rate with temperature

is as expected for temperatures of the order of and above the Debye temperature of the

material.[87] In the following section where the phonon dispersion of Ni$_3$Sn$_2$S$_2$ is analysed

an estimation of the Debye temperature of Ni$_3$Sn$_2$S$_2$ is given as 278 K, which is consistent

with the present analysis. For temperatures above Debye temperature and in the absence

of significant impurity contributions, both σ and τ are roughly inversely proportional to

temperature, which makes the ratio σ/τ almost constant, as seen in Figure 3.4a. Finally,

these calculations also provide access to individual components of the electronic

conductivity tensor. On the assumption of isotropic relaxation time, the ratio σ_{zz}/σ_{xx} as a

function of temperature is obtained. The inset of Figure 3.4c shows that there is significant

anisotropy in this case, with the conductivity within the Kagome plane (σ_{xx}) being around

twice the conductivity in the perpendicular direction (σ_{zz}). This is expected since the

Kagome plane contains a two-dimensional network of zero-valent metal (Ni) atoms which

locally increases the density of electronic states.

G. Electronic thermal conductivity

In contrast to calculations where both the electronic (κ_{el}) and lattice contributions

(κ_{latt}) to the thermal conductivity can be determined, in experiment only the total thermal

conductivity is measured. This section first discusses only the electronic thermal

conductivity (and its connection to the electronic conductivity σ). The discussion of the experimental total thermal conductivity will be presented below (Section H), together with results of the lattice thermal conductivity calculations. The κ_{el} values can also be obtained from the Boltzmann transport equation, but as in the case of σ only the values relative to the relaxation time (*i.e.*, κ_{el}/τ) can be determined. The relaxation time for electronic heat transport is not necessarily the same as the relaxation time considered above for the electronic conductivity, but for metals in the regime of temperatures of interest here (similar to or above the Debye temperature) the two relaxation times can be considered approximately equal.[87] In this case, it is expected that the ratio σ/τ follows the Wiedemann-Franz law, *i.e.*, it is simply proportional to temperature, with the proportionality constant being the Lorenz number ($L_0 = 2.44 \times 10^{-8}$ W.K^{-2}). Figure 3.5 shows that the calculated transport coefficients follow the Wiedemann-Franz law to a good approximation, although there are some deviations at higher temperatures, where the effective Lorenz number becomes somewhat higher than L_0 (by up to 10% at 600 K).
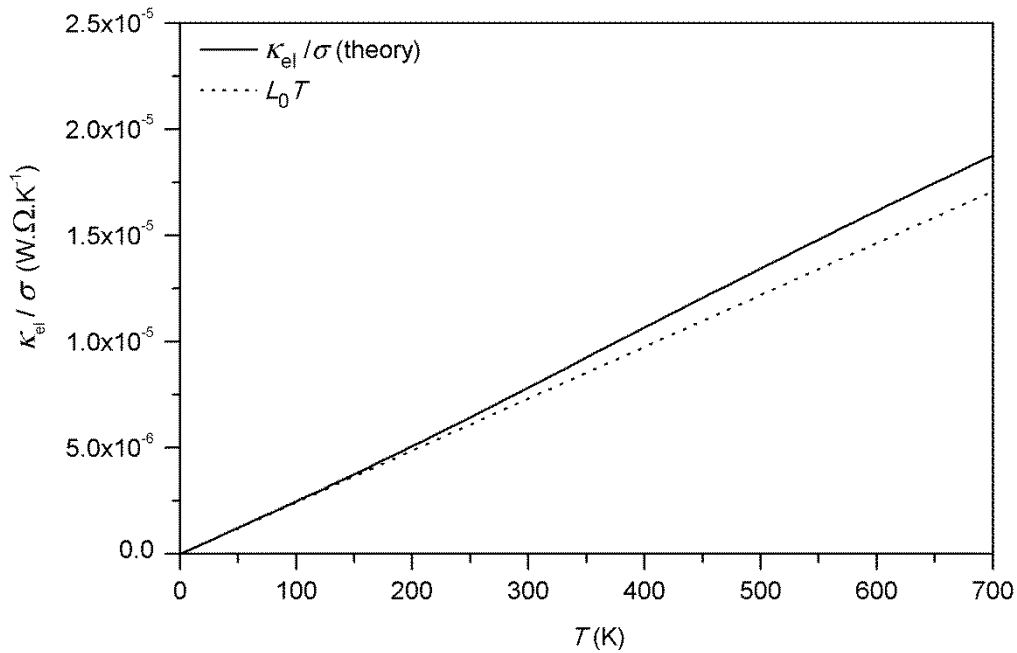

Figure 3.5. Ratio between the electronic contribution to the thermal conductivity (κ_{el}) and the electrical conductivity (σ) as a function of temperature, in comparison with the expectation from the Wiedemann-Franz law.

The predicted absolute value for the electronic thermal conductivity using the relaxation time determined from the experimental conductivity does not vary strongly with temperature. Values of 20.8 and 22.3 $Wm^{-1} K^{-1}$ are obtained at 300 K and 600 K respectively. This is expected from the Wiedemann-Franz law and the result in the previous section showing that σ is roughly inversely proportional to temperature due to increased scattering events at higher temperature. The anisotropy of the electronic thermal conductivity tensor was found to follow a very similar pattern as that of the electronic conductivity tensor.

H. Phonon structure and lattice thermal conductivity

To determine the total thermal conductivity, it is necessary to calculate lattice contribution which is the result of vibrations of atoms in the system. The first step is the calculation of the second order force constants in the harmonic approximation (2.55). The solution of which gives the phonon dispersion curves and allows the Debye temperature to be determined. The phonon dispersion curves along the high-symmetry directions in the Brillouin zone are shown in Figure 3.6.
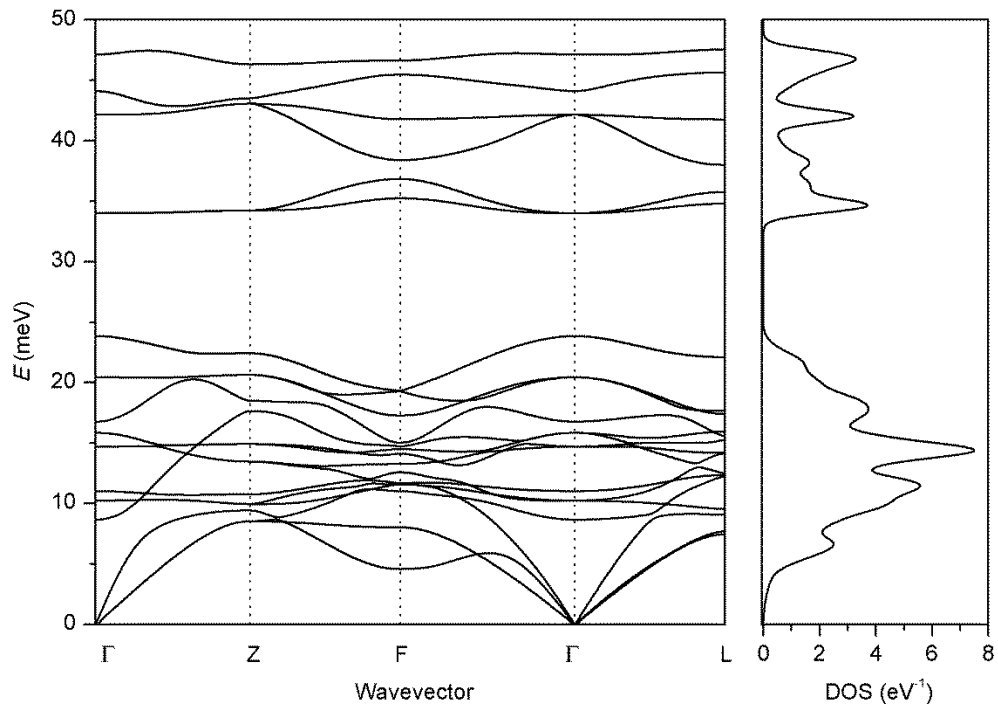
Figure 3.6. Phonon dispersion curves of Ni$_3$Sn$_2$S$_2$ along high symmetry paths in the Brillouin zone, and the corresponding phonon density of states.

Consistent with the primitive cell of 7 atoms there are 21 phonon modes: 3 acoustic and 18 optical branches. The vibrational density of states is divided in two groups; the lower one comprises 15 branches and the upper one comprises 6 branches, with a gap of about 10 meV between the two groups. From the phonon structure the specific-heat capacity of the solid as a function of temperature (ignoring for the moment anharmonic contributions) can be calculated and is shown in Figure 3.7.
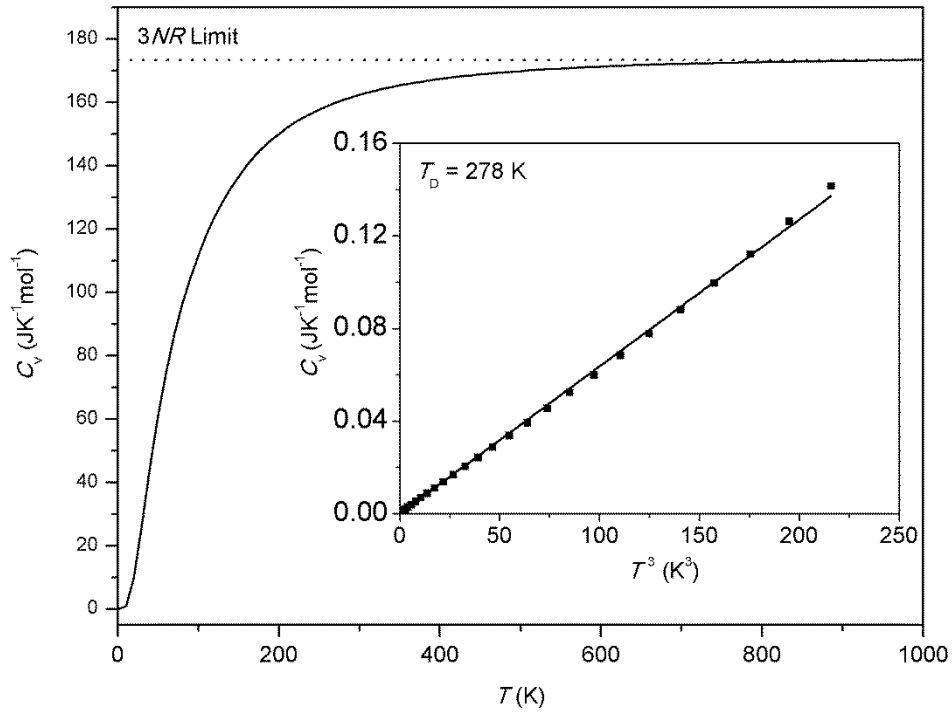
Figure 3.7. Specific-heat capacity of $Ni_3Sn_2S_2$ per mole of formula units. The limiting value at high temperature is 3NR where N = 7 is the number of atoms per formula unit and R is the gas constant. The fitting of the low-temperature values of the heat capacity to a Debye model (inset) is used to obtain the Debye temperature.

In the low-temperature limit, C_v is proportional to T^3.[71] and a Debye temperature of 278 K is calculated from Equation (2.60) (inset of Figure 3.7). From the anharmonic displacements the κ_{latt} can be calculated and is shown in Figure 3.8a as a function of temperature. At 300 K, it is approximately 2 Wm^{-1} K^{-1} and it slowly decreases with temperature down to 1 Wm^{-1} K^{-1} at 600 K. These values are very low, well below typical values for crystalline solids, and similar to what is found for disordered materials like amorphous silicon dioxide.[138]

60
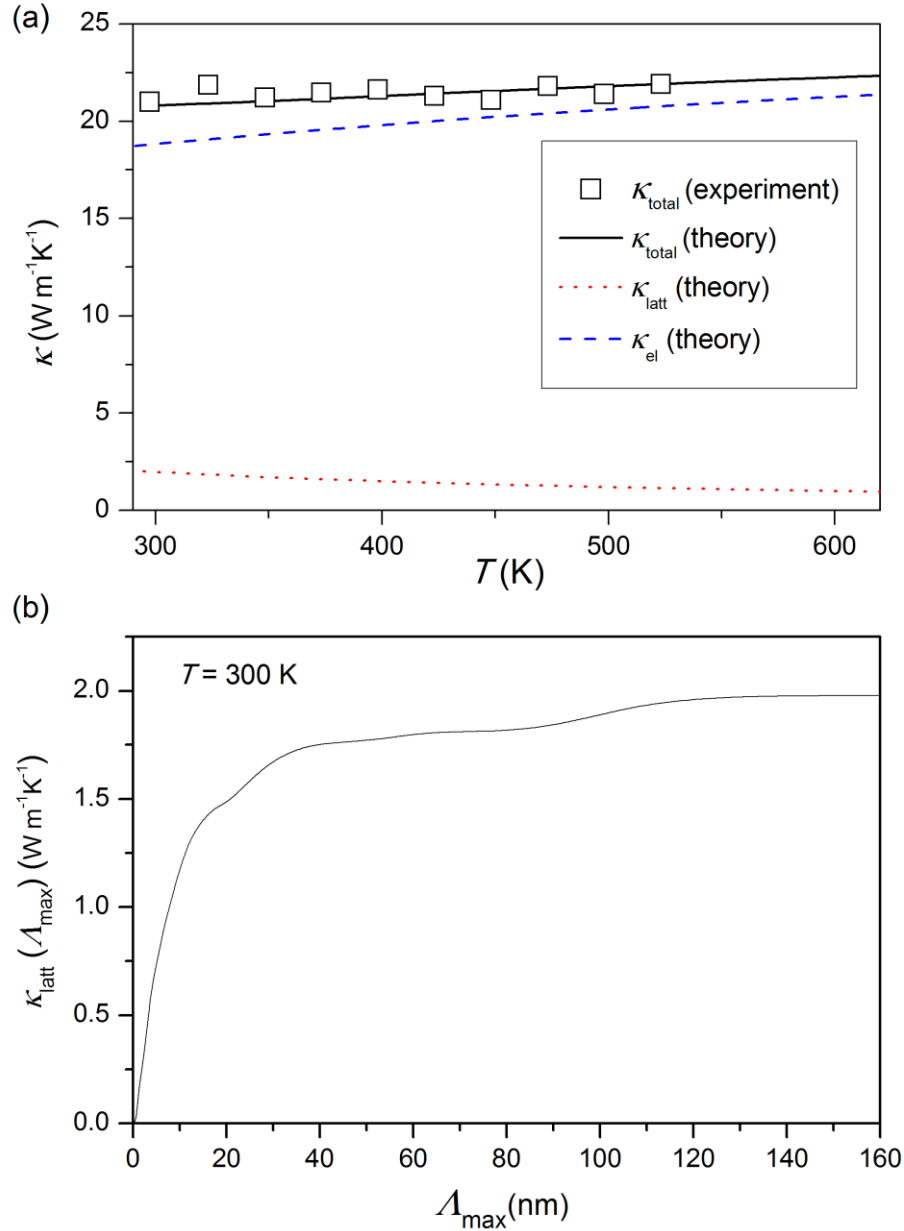
Figure 3.8. (a) Total thermal conductivities from experiment and theory, and calculated electronic (κ_{el}) and lattice (κ_{latt}) contributions vs temperature. (b) κ_{latt} at 300 K as a function of the maximum mean free path.

The origin of the low κ_{latt} is the very anharmonic nature of the vibrations in $Ni_3Sn_2S_2$. This is reflected in a high Grüneisen parameter obtained from these calculations, $\gamma = 1.55$ (in the high-temperature limit), which is about three times that of Si.[139] Lattice thermal conductivity calculations provide further useful information, including directional (tensorial) components as well as the contributions from different phonon mean free paths. The κ_{latt} tensor showed negligible anisotropy at all temperatures above 300 K. On the

other hand, from the mean-free-path analysis we find that nanostructuring is not a viable strategy for reducing thermal conductivity as this would require particle sizes below ~20 nm to achieve any significant effect (Figure 3.8b). In any case, from a point of view of thermoelectric applications, it does not make sense to focus on reducing the lattice thermal conductivity, because the most important contribution to heat transport comes from electrons. The total calculated thermal conductivity, as well as the electronic and lattice contributions, are shown in Figure 3.8a, in comparison with experimental measurements (only for the total thermal conductivity). κ_{latt} contributes just ~10% of the total thermal conductivity, with the remaining 90% resulting from electronic transport. The experimental total thermal conductivities are in excellent agreement with the theoretical values. However, it should be noted that the calculation of the electronic contribution κ_{el} involved the use of a fitted relaxation-time curve $\tau(T)$ to reproduce the electronic conductivity $\sigma(T)$. Because of the Wiedemann-Franz law, such fitting also guarantees a good theoretical value for κ_{el}. However, it is still remarkable that the calculated values of κ_{latt}, which were obtained without any fitting parameters, bring the total theoretical values of thermal conductivity to perfect agreement with experiment. Thus, the theoretical lattice thermal conductivity predictions are confirmed by the experimental measurements.

I. Thermoelectric figure of merit *ZT*

In order to summarize the thermoelectric behaviour of $Ni_3Sn_2S_2$, the thermoelectric figure of merit (*ZT*) of the material is calculated as a function of temperature using both the theoretical and experimental data (Figure 3.9a). Two theoretical *ZT* curves are given, one excluding and the other including the lattice thermal conductivity term. In the former case, the prediction is fully ab initio, because the relaxation time cancels out, and Equation (1.1) becomes

$$ZT \approx \frac{\sigma S^2 T}{\kappa_{\text{el}}} \approx \frac{S^2}{L_0} \qquad (3.3)$$

In fact, since κ_{latt} contributes only around 10% to the total thermal conductivity, its effect on ZT is very small, as can be seen in Figure 3.9a. The calculation of the ZT taking into account the lattice contribution to the total thermal conductivity is not fully predictive, as it involves the fitting of the relaxation times. In any case, the theoretical prediction agrees well with experiment, showing an increase with temperature that is approximately quadratic (because S has an approximately linear variation with temperature). The values of ZT in $Ni_3Sn_2S_2$ are too small for thermoelectric applications, which, as Equation (3.3) indicates, is mainly due to the low Seebeck coefficient.

A possible strategy to improve the Seebeck coefficient and ZT is via doping and this is now considered. It is important to note that doping is only considered here in the rigid band approximation where addition of carriers does not significantly affect the band structure. It is therefore only possible to discuss dilute doping with either a small excess or deficiency of electrons. Figure 3.9b shows the dependence of ZT on the concentration of doped charge carriers, which can be studied by varying the chemical potential, as shown in the figure inset. The ZT is predicted to increase with small concentrations of electron doping (negative doping charge density), although the magnitude of the increase is still modest. Clearly, a wider range of doping concentrations must be considered in trying to achieve a significant increase in ZT but cannot be rigorously done within the rigid band approach; it would instead require the dopant atoms to be explicitly included in the supercell.[140, 141]
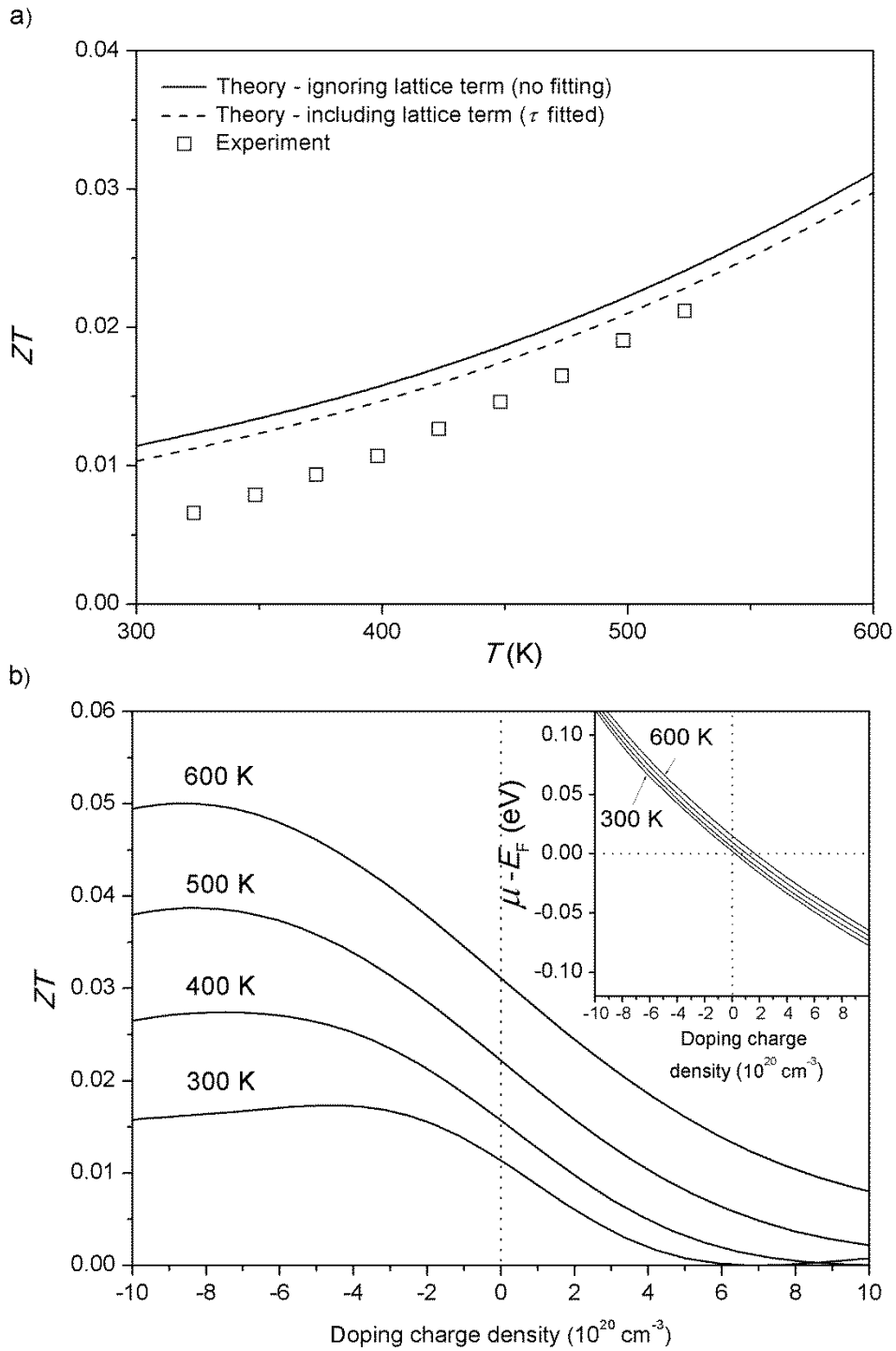
Figure 3.9. (a) Thermoelectric figure of merit (ZT) of Ni$_3$Sn$_2$S$_2$ from experimental and from theoretical data. (b) Effect of dilute doping on ZT (the inset shows the correspondence between the doping charge density and the chemical potential within the rigid band approximation).

3.3.2 Magnetic $Co_3Sn_2S_2$

A. Density of States

The relaxed parameters for the $Co_3Sn_2S_2$ crystal in calculations were a=5.381 Å and c=13.166 Å, compared to experimental room temperature values of a=5.370 Å and c=13.193 Å. Therefore, the PBE geometry is in excellent agreement with the experimentally determined one. The density of states of the two end member phases $Ni_3Sn_2S_2$ and $Co_3Sn_2S_2$ are shown in Figure 3.10. As discussed in the previous section the symmetrical electronic structure of $Ni_3Sn_2S_2$ clearly shows describes a nonmagnetic ground state and justifies the use of nonmagnetic DFT calculations. The asymmetry seen in the density of states of the $Co_3Sn_2S_2$ phase confirms its half metallic nature with a band gap in the minority spin channel.[107, 110] The calculation of the electronic and transport properties for the $Co_3Sn_2S_2$ phase must therefore take into account spin polarisation.
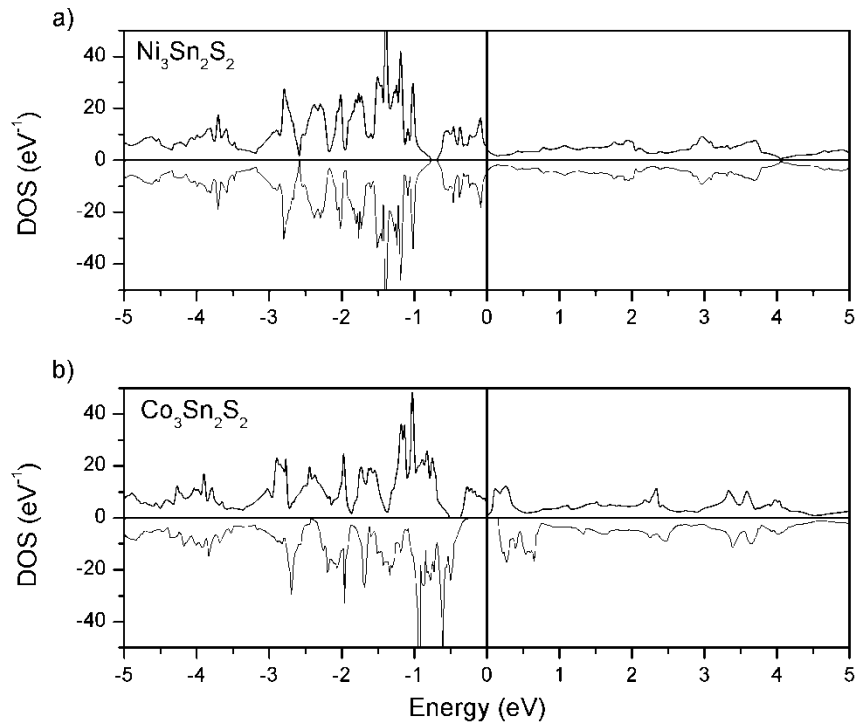
Figure 3.10. A comparison of the density of states of the end member phases a) $Ni_3Sn_2S_2$ and b) $Co_3Sn_2S_2$

B. Seebeck coefficient

The determination of the Seebeck coefficient (S) requires obtaining the group velocities as a function of energy. In the nonmagnetic case, S can be calculated directly using Equation (2.38). In the spin polarized case a further approximation needs to be made using the two-current model.[142] In the two-current model, spin-flip scattering is neglected and S is calculated as a conductivity-weighted average of the Seebeck coefficients of the up and down spin channels (S_{up} and S_{dn}):

$$S = \frac{\sigma_{up}S_{up} + \sigma_{dn}S_{dn}}{\sigma_{up} + \sigma_{dn}} \tag{3.4}$$

and the total conductivity is given as the sum of the respective conductivities of each spin channel.

$$\sigma = \sigma_{up} + \sigma_{dn} \tag{3.5}$$

This approximation neglects electrons moving from one channel to the other as the conductivity of each is treated independently. While it seems the two-current model maybe suitable for ferromagnetic materials where the spin channels are independent;[143] $Co_3Sn_2S_2$ is paramagnetic with a Curie temperature of 177 K,[107, 108] and therefore the applicability of the model should be questioned. The system was also modelled in the antiferromagnetic configuration that exhibits an equivalence between up and down spin channels, therefore resembling the paramagnetic state. The resulting Seebeck coefficients are shown in Figure 3.11 in comparison with experimental data.
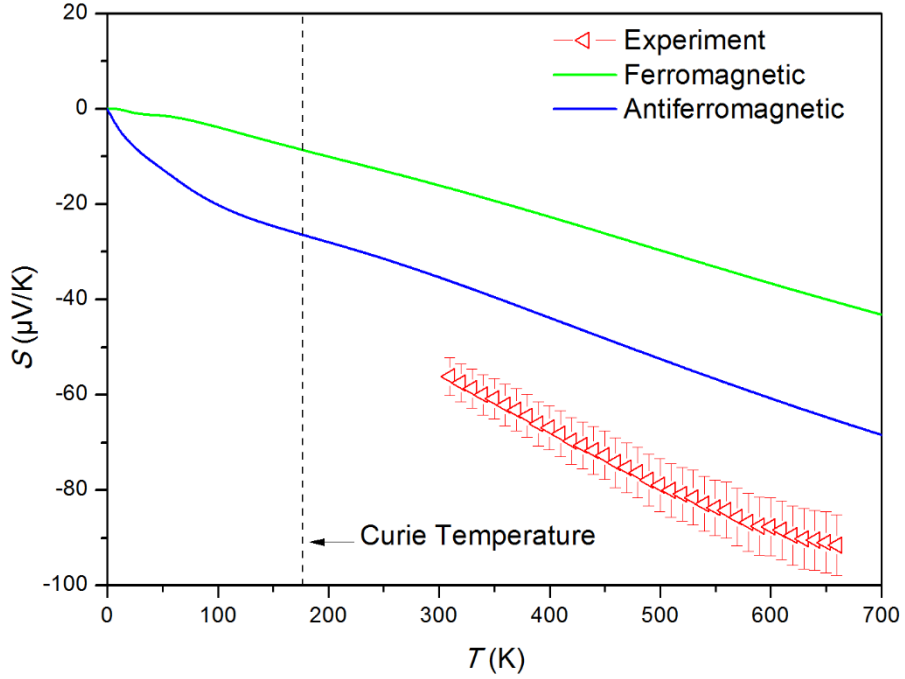
Figure 3.11. Theoretical Seebeck coefficients using the ferromagnetic and antiferromagnetic configurations and the experimental values as function of temperature.

The calculations correctly predict negative values of the Seebeck coefficient, that increase in absolute value with temperature. The results based on the ferromagnetic model quantitatively disagree with the obtained experimental results, whereas the results in the antiferromagnetic configuration provide better agreement: In both cases the calculated $|S|$ values are still considerably lower than the experimental values. We do not think that the problem is caused by the GGA approximation used in the PBE functional. The observation that the calculation of S in the antiferromagnetic configuration gives better agreement with experiment, points to the inaccuracy of these transport models when describing paramagnetic systems. In the Co phase the collective excitation of electrons from one channel to the other, which are known as magnons, have a significant effect on the charge transport scattering of the material. From here on, transport properties of $Co_3Sn_2S_2$ are given from the results obtained in the antiferromagnetic configuration.
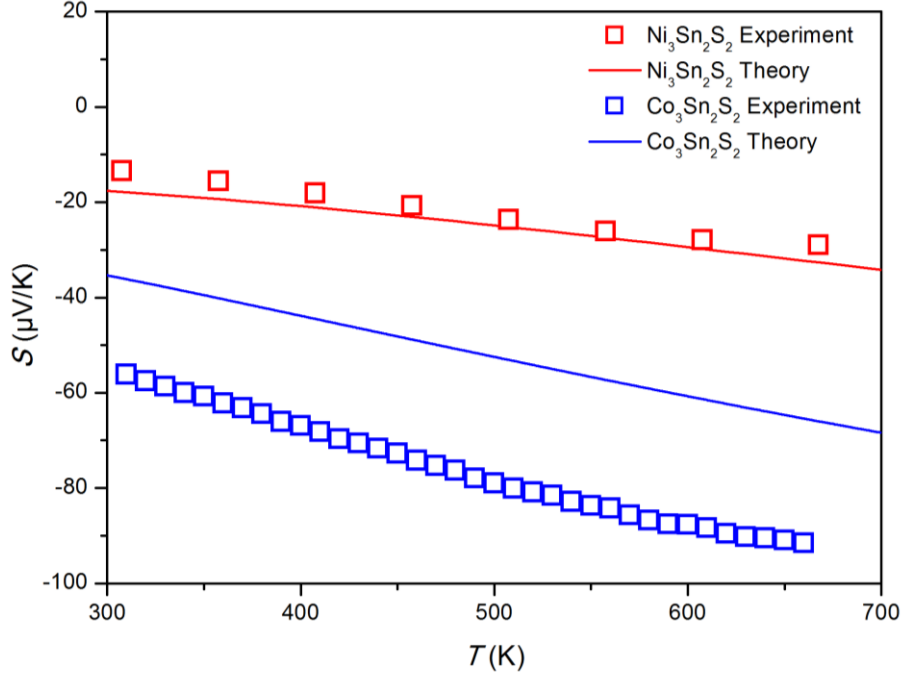
Figure 3.12. Comparison of theoretical and experimental Seebeck coefficients for $Ni_3Sn_2S_2$ and $Co_3Sn_2S_2$.

We now compare the properties of $Co_3Sn_2S_2$ and $Ni_3Sn_2S_2$. At room temperature, the Seebeck coefficient of the Ni shandite is three to four times smaller than that of the Co phase (approximately −50 μV/K).[117] This can be explained by the difference in the electronic structure of the two compounds. It is well known that semiconductors generally exhibit much higher Seebeck coefficients than metals.[144] For half-metals, the Seebeck coefficient is approximately given by the two-current model,[142, 143] *i.e.*, the conductivity-weighted average of the Seebeck coefficients of the two spin channels. Therefore, half-metallic $Co_3Sn_2S_2$ can be expected to have a higher Seebeck coefficient than fully metallic $Ni_3Sn_2S_2$, as observed.

C. Electronic conductivity and scattering rates

A comparison is shown between the calculated values of σ/τ for both $Ni_3Sn_2S_2$ and $Co_3Sn_2S_2$ in Figure 3.13. In both cases σ/τ remains about constant over the temperature range shown, which suggests that increasing the temperature in both cases

leads to a cancellation of effects caused by a reduction in the conductivity but also a reduction in the relaxation time. It seems however that for the Co phase the situation is rather more complicated as σ also remains constant as the temperature is increased (Figure 3.14).
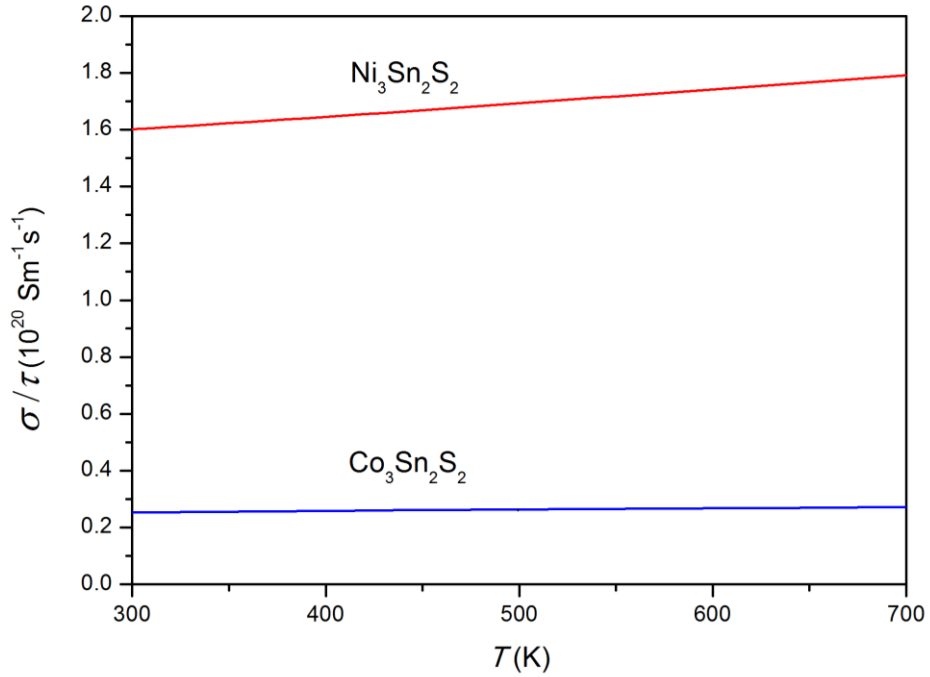
Figure 3.13. Comparison of σ/τ for Ni₃Sn₂S₂ and Co₃Sn₂S₂
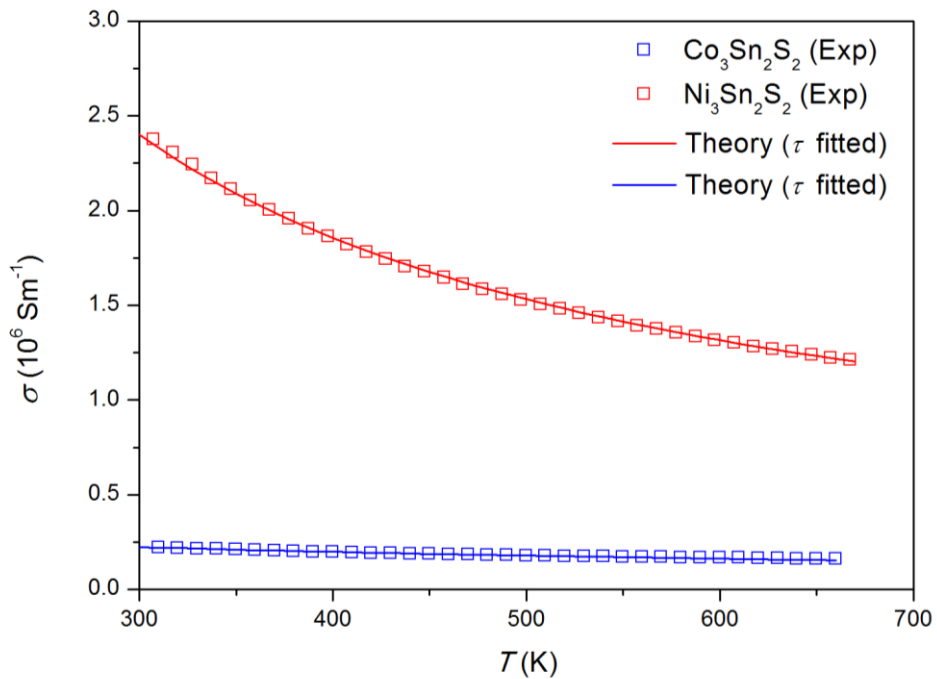
Figure 3.14. Conductivity of the Ni₃Sn₂S₂ and Co₃Sn₂S₂ as a function of temperature

The constant σ seen with respect to temperature in the Co phase may be attributed again to the two opposing effects in the different spin channels. One channel being metallic results in a decrease in conductivity as the temperature increases but the band gap seen in the minority spin channel results in an increase in σ with respect to increasing the temperature.
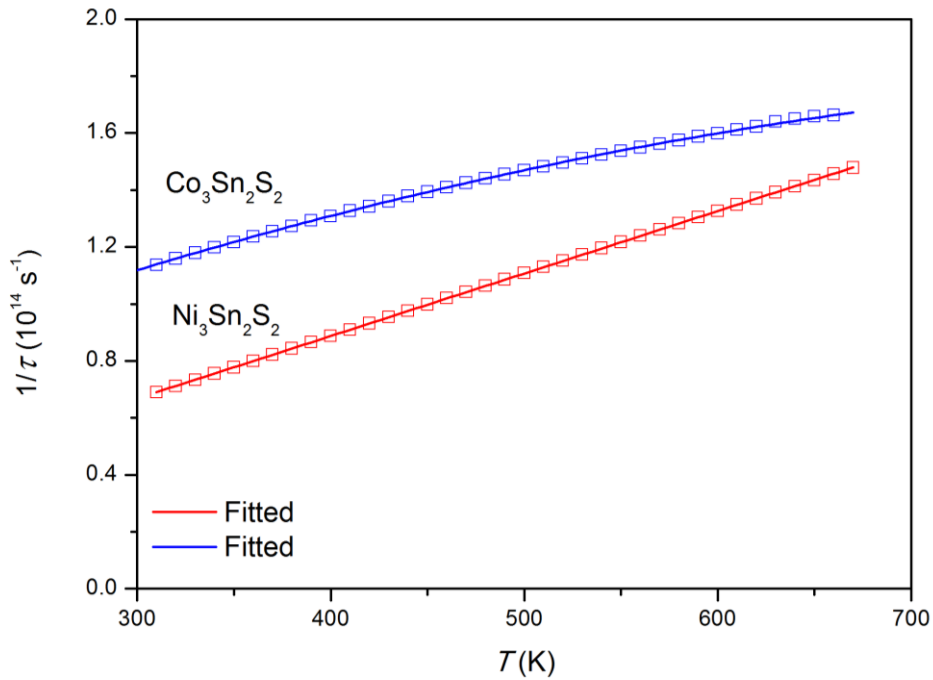
Figure 3.15. Fitted scattering rates for Ni₃Sn₂S₂ and Co₃Sn₂S₂

Figure 3.15 shows the scattering rates of $Ni_3Sn_2S_2$ and $Co_3Sn_2S_2$ as a function of temperature fitted to Matthiessen's rule as reported in the previous section 3.3.1.F. Whilst we see that the Ni phase is an excellent fit based on Matthiessen's rule there is some deviation from linearity for the Co phase. Although it is noted that Matthiessen's rule fails when the outcome of one scattering process has an influence of another scattering process or the τ is a function of k.[87] In both phases the results are approximated assuming τ is independent of k, but in the case of Co spin-flip scattering is ignored which may affect the deviation from linearity at higher temperatures. It may also be due to the non-linearity

of scattering rates in semiconductors as the Co-phase has a small band gap in the minority spin channel.

D. Thermoelectric figure of merit

The *ZT* for Ni$_3$Sn$_2$S$_2$ and Co$_3$Sn$_2$S$_2$ are shown in Figure 3.16. The experimental values are shown against calculated values when κ_{latt} is ignored in Equation (1.1). Using this method, the relaxation times cancels and it is possible to obtain a fully theoretical approximation to the *ZT*. It is noted that this method works when κ_{el} is significantly higher than κ_{latt} as in the case of metals. In semiconductors where both κ_{el} and κ_{latt} are significant this approximation would result in a considerable overestimation of the *ZT*. Of course, the cancellation of the τ term assumes that τ for both σ and κ_{el} are approximately equal. Whilst the Ni phase is in good agreement with experimental values, the *ZT* of Co phase is underestimated compared to experiment. The underestimation is attributed to the Seebeck coefficient which is underestimated in the Co phase. Although the calculation of transport properties for the Co-based paramagnetic system needs further refinement, the correct prediction of the half metallic nature of Co$_3$Sn$_2$S$_2$ suggests that the PBE description is reasonable. Therefore, we will investigate the effect of dopants on the electronic structure, gaining an insight into what possible effect this would have on the transport properties. This is explained in the next section with the Co$_3$Sn$_{2-x}$In$_x$S$_2$ solid solutions.

71
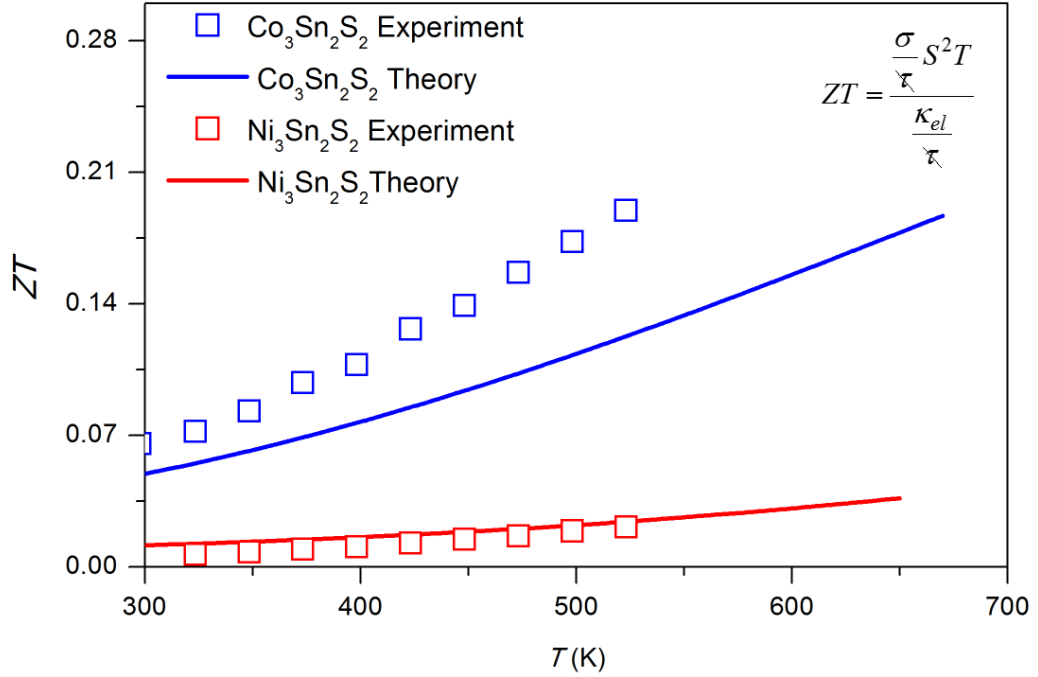
Figure 3.16. Experimental *ZT* of Ni₃Sn₂S₂ and Co₃Sn₂S₂ as well the theoretical values when κ_latt is ignored from Equation (1.1).

3.3.3   Co₃Sn₂₋ₓInₓS₂ solid solutions

A. **Lattice parameters**

To represent the disordered solids, a configurational ensemble was used, considering only inequivalent configurations as implemented in the SOD program (described in Section 2.4). Table 3.3 shows the total number of configurations and the number of inequivalent conformations for each composition. This analysis was performed using the PBE functional with and without the U correction. The calculated lattice parameters obtained with the U correction were found consistently higher than the calculation performed with no U correction. The PBE+U method also predicts a relatively strong variation of both a and c cell parameters at In rich compositions, in disagreement with experiment and PBE results. The results with no U correction were also in excellent agreement with the experimentally determined values (Figure 3.17).

Table 3.3. The total number of possible configurations and the number of inequivalent configurations from each cell composition in the unit cell of $Co_3Sn_{2-x}In_xS_2$.

Composition	Total number of configurations	Number of inequivalent configurations (N)
$Co_9Sn_6S_6$	1	1
$Co_9Sn_5In_1S_6$	6	2
$Co_9Sn_4In_2S_6$	15	4
$Co_9Sn_3In_3S_6$	20	6
$Co_9Sn_2In_4S_6$	15	4
$Co_9Sn_1In_5S_6$	6	2
$Co_9In_6S_6$	1	1

As the composition (x) is increased from 0 to 1, a decreases monotonically until the stoichiometric phase Co_3SnInS_2 ($x =1$) is reached. At compositions of x greater than one there is little variation in cell parameter a.
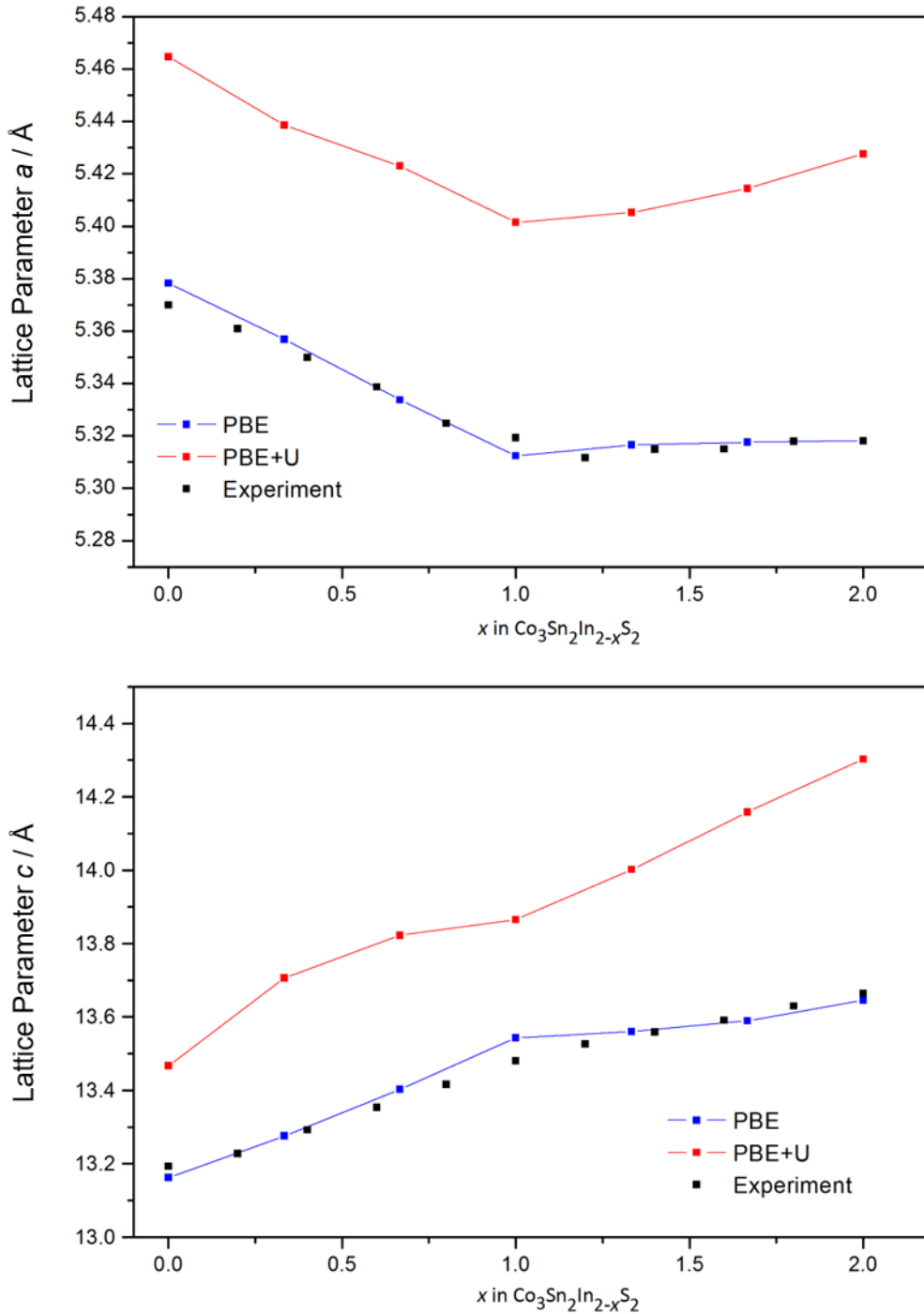
Figure 3.17. A comparison of computationally and experimentally determined lattice parameters of Co₃Sn₂-ₓInₓS₂.

The complete substitution of In for Sn results in only around a 1.6% change in volume of the unit cell. This could be attributed to the larger radius of In, but the compositional dependence of the lattice parameters suggests additional factors may play a role. The substitution of In for Sn leads to a reduction in the number of electrons in the

unit cell. Across the compositional range full substitution of In for Sn leads to a reduction of two valence electrons. To investigate the variations in electronic structure with composition, the electronic density of states was calculated for the most stable configuration for each composition.

B. Density of states

Previous experiments have shown that $Co_3Sn_2S_2$ has the electronic structure of a half metal[107] compared to that of a semiconductor in the half-doped ($x=1$) compound.[145] The density of states shown in left panel of Figure 3.18 clearly support previous results and also predict full metallicity in the pure-In ($x=2$) compound with a valence electron count of 45 per formula unit. Further examination of the calculated DOS indicates that the major contributors to the states just below the Fermi level are the Co-d_{xy} and Co-$d_{x^2-y^2}$ orbitals. This is consistent with the Bader analysis performed indicating a Co^0 valence across the various compositions as well as the results obtained for the Ni phase (Table 3.2). As x is increased these states are depopulated by In substitution and at $x = 1$, these states are completely depopulated. As In substitution is further increased the Fermi level is decreased to lower-lying states which are necessarily less antibonding in character, while leading to occupancy of an increasing fraction of the intralayer sites by the larger atoms. These competing factors may lie behind the effectively constants a lattice parameter at levels of substitution beyond $x = 1$.
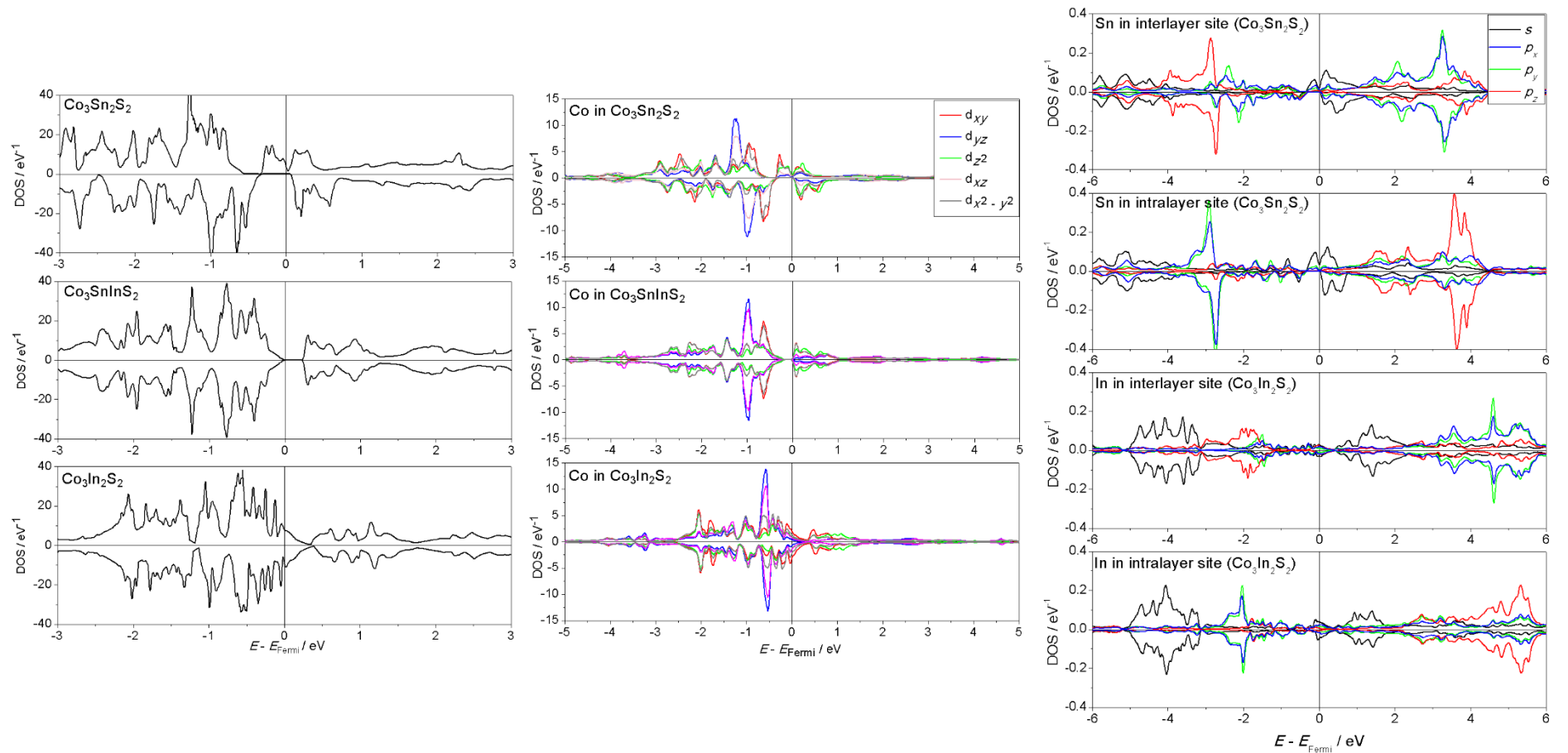
Figure 3.18. Total (left) and partial (projected on the Co 3*d* orbitals, middle) electronic density of states (DOS) for Co₃Sn₂₋ₓInₓS₂ (*x* = 0, 1, 2) determined from DFT calculations. Calculations for Co₃SnInS₂ were performed for the most energetically favourable configuration. On the right are the partial calculated DOS of the end member (*x* = 0, 2) phases projected on the 5*p* orbitals of the main group element at the interlayer (M(1)) and intralayer (M(2)) sites.

C. Cation distribution

Figure 3.19 represents the cation distribution showing the partitioning of In between the interlayer and intralayer sites for each overall composition. At full disorder (as the temperature approaches infinity) there is no preference for partitioning and In is equally distributed between the two sites. However, at low equilibration temperatures there is a clear preference for In to occupy the interlayer sites until they are saturated at composition $x = 1$ after which In begins to occupy the intralayer sites. Equilibrium distributions can be obtained as a weighted average over all configurations in the ensemble at any temperature using the equation

$$f_s = \sum_m P_m f_{s,m}$$

(3.6)

where P_m is the Boltzmann-like probability as described in Equation (2.72) and $f_{s,m}$ is the ratio between the number of In ions in sites of that type, and the total number of sites of that type.

The experimental results and simulations using the PBE functional at 1,073 K are in excellent agreement showing the preferential In occupancy of the interlayer sites. The PBE+U results are also shown and do show the same trend but with less quantitative agreement to the experimental results.
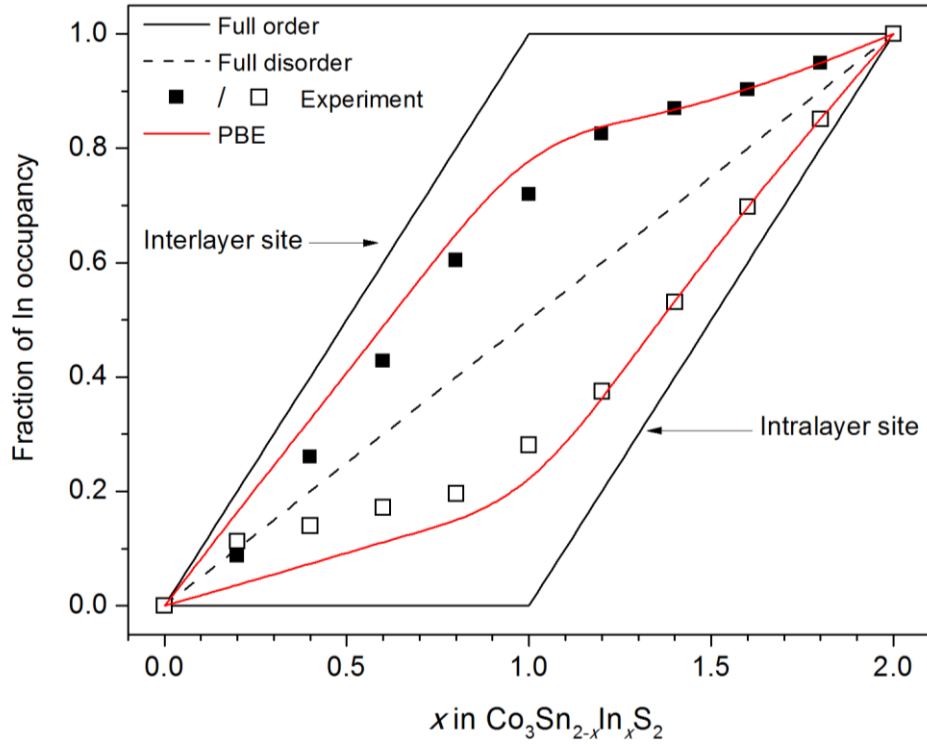
Figure 3.19. Compositional dependence of indium site occupancy factors associated with the interlayer and intralayer sites in Co₃Sn₂₋ₓInₓS₂ (0 ≤ x ≤ 2). Solid and open points denote experimental values for interlayer and intralayer sites respectively and the solid red line, the PBE result from DFT calculations. The variation of site occupancy factors corresponding to full ordering into the interlayer site and to a completely disordered structure are indicated by solid and dashed lines, respectively.

The clear preference of In for the interlayer site may lie in the differing bonding requirements at the two sites. The right panel of Figure 3.18 shows the partial DOS of the p-orbitals of the end members phases. At the interlayer site, the p_z orbital lies at a lower energy than the degenerate p_x / p_y orbitals, while at the intralayer site the opposite is the case. At the interlayer site the p_z orbital bonds to Co atoms in adjacent Kagome layers, whereas in the intralayer site bonding occurs within the Kagome layer through six 3-centre Sn or In - Co bonds involving both the p_x and p_y orbitals (Table 3.4). Both In and Sn with three and four valence electrons respectively are able to satisfy these bonding requirements. However, the requirement of two p-orbitals to be occupied in the intralayer site suggests that Sn with its extra valence electron, is better able to satisfy the bonding

requirements at this site. This would account for the preferential occupation of the interlayer site for In with one less valence electron. In only needs to occupy one p_z orbital at the interlayer site. The incomplete nature of the ordering suggests that the energy differences are small.

Table 3.4. Electron filling in the $Co_3Sn_{2-x}In_xS_2$ system. Sn has one extra valence electron compared to In and is stabilised in the intralayer site where it can occupy the p_x and p_y orbitals

Orbital	M(1) (interlayer)	M(2) (intralayer)
p_x	Vacant	Occupied
p_y	Vacant	Occupied
p_z	Occupied	Vacant

D. Thermodynamics of mixing

The free energies and enthalpies of mixing were calculated based on Equation (2.75) and the results plotted in Figure 3.20. The enthalpies of mixing were taken at the high temperature limit ($T \rightarrow \infty$) indicating full disorder and at the low temperature limit ($T \rightarrow 0$) indicating a fully ordered system. To compare calculated results with the experimental data the enthalpy and free energy of mixing were calculated at the common synthesis temperature of 1,073 K as well as the slightly lower value of 773 K. The results show that the fully disordered system has a more positive enthalpy of mixing compared to the fully ordered system. This supports the cation distribution results described in the previous section 3.3.3C. In the fully disordered system there would be a higher enthalpy of mixing due to a higher weighting of the of the higher-energy (less stable) configurations. At the common synthesis temperature, the enthalpy of mixing is in between the ordered and disordered system as expected. The free energy of mixing is also

plotted and the results show that the mixed system is more stable that then pure systems confirming that the solid solutions can be readily synthesised in thermodynamic equilibrium, without any tendency for phase separation.
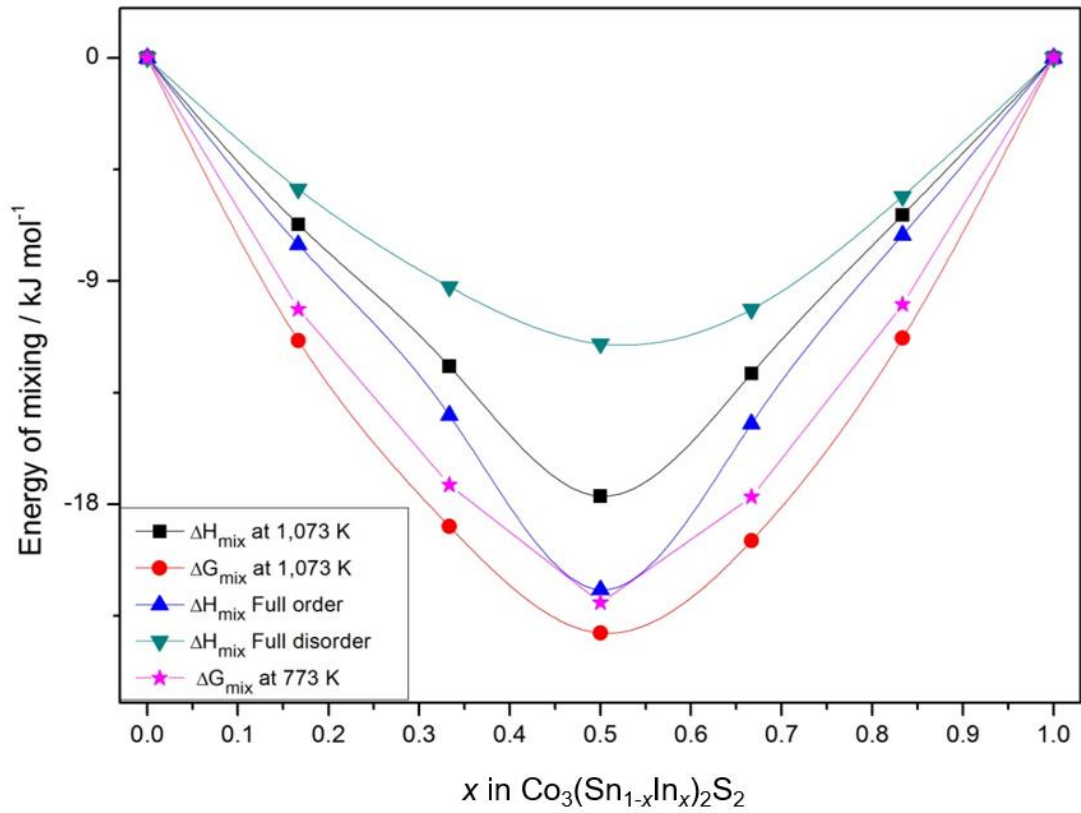
Figure 3.20. Energy and Enthalpy of mixing of $Co_3(Sn_{1-x}In_x)_xS_2$

3.4   Conclusions

A full theoretical study of the electronic phonon structure and transport behaviour of the nonmagnetic shandite-phase $Ni_3Sn_2S_2$ has been reported. The theoretical results, in particular the Seebeck coefficient and lattice thermal conductivities, which are predicted without any fitting parameters, are in excellent agreement with experiment. The dominant electron scattering mechanism is via phonons, and from the comparison of theoretical and experimental results we have obtained the temperature dependence of the electron-scattering rates. Pure $Ni_3Sn_2S_2$ is not a good thermoelectric material, as it has a very low thermoelectric figure of merit ($ZT \sim 10^{-2}$ at room temperature). Its lattice thermal conductivity is very low and contributes only $\sim 10\%$ of the total thermal conductivity. Therefore, for this material very little can be gained by nanostructuring or other strategies aimed at reducing heat transport by phonons. In fact, for this metallic shandite, ZT is mainly a function of the Seebeck coefficient. In order to improve ZT, a dramatic change in the Seebeck coefficient would be needed, which we show cannot be achieved by dilute doping. The effort in finding thermoelectric shandites should clearly focus on the half-metallic or semiconductor systems, where the Seebeck coefficients can be engineered to much higher values.

The theoretical calculation of the half-metallic paramagnetic $Co_3Sn_2S_2$ phase was also investigated using spin-polarised calculations in both ferromagnetic and antiferromagnetic configurations. The antiferromagnetic configuration gave a better description of the thermopower of the paramagnetic phase but the model was still not able to accurately predict the experimental values. This may be attributed to the failure of the models to describe spin-flip scattering events which are not included in our models.

Although the current models for predicting the electronic transport fail in the paramagnetic phase, it is interesting to compare the electronic structure of $Ni_3Sn_2S_2$ with

that of $Co_3Sn_2S_2$. The latter has a ferromagnetic ground state with half-metallic character, exhibiting a gap of approximately 0.3 eV for the minority-spin channel.[107] Despite that fundamental difference, the total charge-density distribution over the atoms is very similar for both compounds. In both $Ni_3Sn_2S_2$ and $Co_3Sn_2S_2$, the Ni and Co are found to be zero valent, while the atomic charges for Sn and S are also very similar in each case. With respect to doping of Sn with In a clear trend was seen with, In with one less valence electron preferentially occupied the interlayer site where only one *p*-orbital needed to be occupied rather than two in the intralayer site. Computational calculations also suggest that at a composition of equal In and Sn content the electron transport properties would be optimal, due to its intrinsic semiconducting nature. This has been confirmed by experiment. We did not attempt transport calculations in the solid solutions due to the difficulty in treating the scattering by atomic disorder in the structure.

4 Kesterite semiconductors: cation disorder and electronic structure and transport

An investigation of the cation distribution, electronic structure and transport properties of a family of quaternary chalcogenides with kesterite structure is presented in this chapter. All the computational work presented here has been performed by myself. The experimental work on cation disorder was performed by my PhD colleague Panagiotis Mangelis. Differently from the work presented in other chapters, which has been already published, the work presented here is still in progress and the interpretation is therefore preliminary. However, some clearly interesting results have already emerged, which we think are worth including in the thesis.

4.1 Introduction

The finding of efficient earth-abundant, non-toxic and low-cost materials for use in thermoelectric devices is key to their wide scale implementation. Kesterites are a family of quaternary chalcogenides that are being widely investigated for their use in solar cell devices.[146-149] They are based on the structure with formula unit A_2BCX_4 (A = Cu, Ag; B = Zn; C = Sn, Ge; X = S, Se) and also show promise as intermediate temperature thermoelectrics.[15, 150] These compounds form in a tetragonal structure, with the distribution of the A, B and C cations within a double zinc-blende cell.

Different cation configurations form the so-called stannite or kesterite structures or mixed structures. Figure 4.1 shows the difference between stannite and kesterite. The stannite structure is found in the $I\bar{4}2m$ spacegroup, the A cation occupies the $z = 0.25$ and 0.75 layers and the B and C cations alternate between the $z = 0$ and 0.5 layers. In the kesterite structure A and B cations are distributed on the $z = 0.25$ and 0.75 layers and again the B and C cations alternate between the $z = 0$ and 0.5 layers. In the mixed structure

both A and B cations are found on the $z = 0.25$ and $z = 0.75$ layers as in the kesterites. The difference is that the B cation is also found on the $z = 0$ and $z = 0.5$ layers.[151-153]
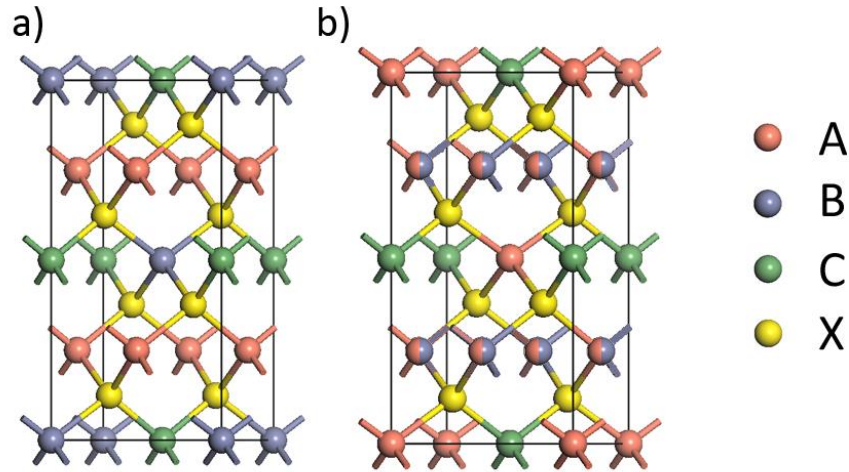
Figure 4.1. Representation of a) the stannite configuration and b) the kesterite configuration indicating the disorder in the $z = 0.25$ and 0.75 planes.

Different distributions of A and B cations in the kesterite structure leads to 3 additional configurations. These are shown in Figure 4.2 alongside the stannite and mixed structure. The configuration in Figure 4.2c with $I\bar{4}2m$ symmetry shows A and B cations alternating between adjacent $z = 0.25$ and 0.75 planes in the 2c and 2d Wyckoff positions. We refer to this structure as kesterite I, whereas in Figure 4.2d, A and B cations are fixed within the plane and adopt $P\bar{4}2c$ symmetry which we refer to as kesterite II. The final configuration with $P\bar{4}2_1m$ symmetry (Figure 4.2e) is where A and B cations are distributed in separate planes and we refer to this structure as kesterite III.[151-153]

Figure 4.2. Different possible configurations for the A₂BCX₄ system in the simplest tetragonal cell with 2 formula units: a) $I\bar{4}2m$ (stannite), b) P2 (mixed), c) $I\bar{4}$ (kesterite I), d) $P\bar{4}2c$ (kesterite II), e) $P\bar{4}2_1m$ (kesterite III).
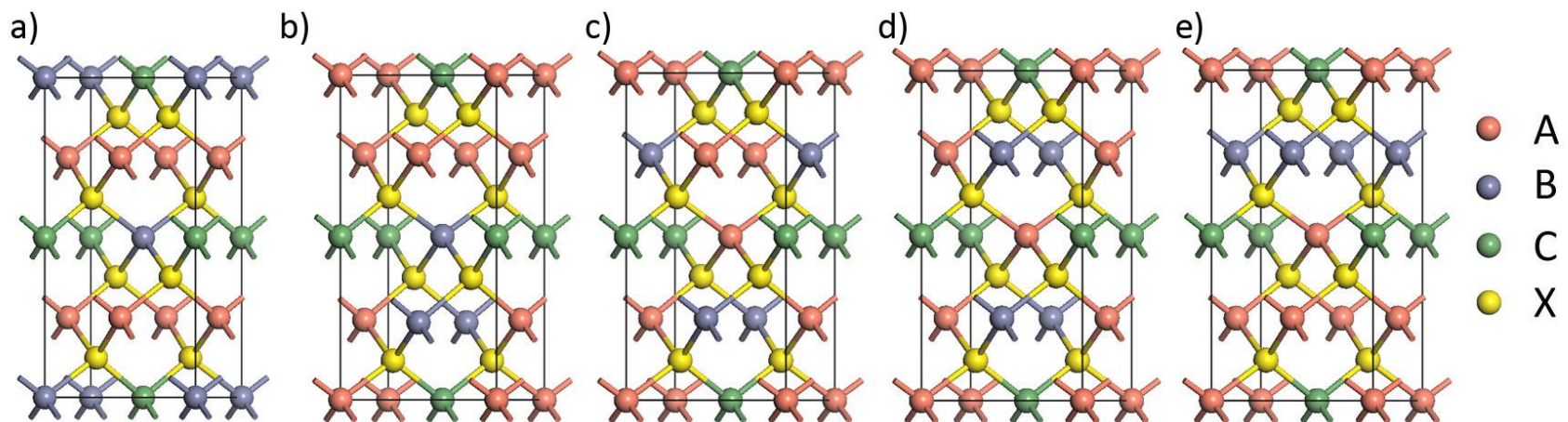
Atomic disorder plays an important role in thin-film solar cells made from $Cu_2ZnSn(S_{1-x}Se_x)_4$. It has been reported that disorder leads to band gap fluctuations that cause a low open-circuit voltage, limiting their efficiency.[12, 13,15, 151, 154] The disordered structure can be seen as a mix between the three kesterite structures, and experimentally it is categorized in the $I\bar{4}2m$ spacegroup.[155] In CZTS, theoretical work reports that at 70% ordering of Cu/Zn on the $z = 0.25$ and $z = 0.75$ planes, a large number of Cu/Zn antisite defects form, which result in band gap fluctuations of about 0.1 eV.[156] In experimental work for CZTS a critical ordering temperature of ~533 K has been reported.[157] Similar results have been found in CZTSe with an order/disorder transition temperature of 473 K being reported,[158] which is well below typical synthesis temperatures.[159, 160] Valentini et $al.$[161] report that disordered CZTSe has a band gap which is 0.2 eV lower than the ordered fully ordered configuration. In theoretical studies, it has been suggested that the small energy differences between the configurations,[147, 162] leads to a combination of the structures being present in experimentally prepared samples. Chen et $al.$[147] report a randomization energy of only a 9.1 meV / atom for the Cu + Zn layer, the result of the similar size of the Cu^+ and Zn^{2+} cations. There is also some debate about the Ag-based structures Ag_2ZnSnS_4 (AZTS) and $Ag_2ZnSnSe_4$ (AZTSe), which have been reported in the kesterite structure in theoretical studies,[163, 164] but also in the stannite configuration.[165, 166]

The substitution of S for Se in CZTS has also shown to affect the band gap of the structures and is likely to affect its transport properties. Experimentally the band gap for CZTS is around ~1.5 eV[167-174] and CZTSe ~1.0 eV.[175-177] Increasing the Se content results in a linear decrease in the band gap. The ability to tune the band gap is desirable for both photovoltaic and thermoelectric materials. Calculations by Chen et $al.$[162] and Zhao et $al.$[178] performed on $Cu_2ZnSn(S_{1-x}Se_x)_4$ suggested that S/Se are highly miscible and the

formation of the solid solution does not lead to significant changes in the Cu/Zn ordering in the material. Calculations performed by Zhao *et al*. show increasing the composition of Se, results in a reduction in the band gap which is due to a downshift of the conduction band rather than any significant change in the valence band maximum.[178] In $Cu_2ZnGe(S_{1-x}Se_x)_4$ solid solutions there is an added layer of complexity as a phase change in the structure leads to insulator - metal transitions that occur from around 450 K for the pure Cu_2ZnGeS_4 (CZGS) phase to 575 K for the pure Cu_2ZnGeS_4 (CZGSe) phase.[179] This effect can be seen in the Seebeck coefficient, as the temperature increases above 500 K, a change in the gradient as well as a local minimum are reported.[179, 180]

The work presented in this Chapter aims to understand the underlying mechanisms for ordering in the quaternary chalcogenides, the thermoelectric properties of CZTSe is also investigated.

4.2 Computational details

4.2.1 DFT calculations

Calculations were performed on the conventional $1 \times 1 \times 1$ unit cell (tetragonal cell with 2 formula units) containing 16 atoms. As the structures are non-magnetic, non-spin-polarized calculations were performed using DFT as implemented in VASP. Geometry optimizations were performed using the Heyd, Scuseria and Ernzerhof (HSE06)[76, 77] functional on a $2 \times 2 \times 1$ $\boldsymbol{k}$-mesh. Relaxation was performed until the forces on the atoms were minimized to less than 0.01 eV/Å. To obtain accurate electronic-structures, single-point calculations were also performed with the HSE06 functional, with a higher $\boldsymbol{k}$-point density. The projector augmented wave (PAW) method[73, 74] was used to describe the frozen core electrons and their interaction with the valence electrons, which were $4s^2 4d^9$ for Cu, $4s^2 4d^9$ for Ag, $4s^2 4d^{10} 4p^2$ for Ge, $5s^2 5d^{10} 5p^2$ for Sn, $4s^2 4d^{10}$ for Zn, $3s^2 3p^4$ for S and $4s^2 4p^4$ for Se. The kinetic energy cutoff for the plane wave basis set

expansion was set at 410 eV, this was about 30% above the standard value for the given PAW potentials. A $6 \times 6 \times 3$ Gamma centred **k**-mesh was used for integrations in the reciprocal space, giving 22 irreducible *k*-points and this was tested for convergence.

4.2.2 Electron transport calculations

The VASP computer program can be compiled to run with Wannier90. This allows the projections of the wavefunctions in real space and the overlap between the cell periodic part of the Bloch states at neighbouring **k**-points to be calculated. These can then be used to obtain maximally localized Wannier functions (MLWFs), which are needed to interpolate the band structure onto a fine **k**-grid.[181] The disentanglement method was used to freeze the bands around the Fermi level. The disentanglement window was chosen to be between -7 eV below the Fermi level and about 1 eV above the lowest conduction band. The bands within this inner window were kept frozen, whereas in the outer window the MLWFs are variable. The bands contained in the outer window are not relevant for transport properties as they are too far from the Fermi level. All bands below 7 eV from the Fermi level where excluded in the calculations. As the MLWFs in real space can be well represented by bonding orbitals. The band structure was relied upon to choose the initial Wannier projections using atom-centred Gaussian-type orbitals. The choice of A and B *d*-orbitals, C *s*-orbitals and X *sp3* orbitals where A_2BCX_4 (A = Cu, Ag; B = Zn; C = Sn, Ge; X = S, Se) gave a total of 64 WFs. These projections were then used in the iterative algorithm employed within Wannier90 to generate the MLWFs. The final spreads with this choice where real-valued and well-localized WFs. In each case the final spreads were around 0.5 Å for *d*-type orbitals and 2.0 Å – 4.0 Å for the *s* and *p*-type orbitals. Convergence of the spread was less than 10^{-5} $Å^2$ and all WF were real. Test calculations also showed that changing the number of chosen WFs had no effect on the band structure calculations, as long as the frozen window was kept constant as expected.

The MLWFs were then used as a basis set to interpolate the bands and band velocities as described in 2.2.2. The bands were interpolated on a $100 \times 100 \times 50$ $\boldsymbol{k}$-mesh and the transport properties obtained by solving the linearized Boltzmann transport equation using the BoltzWann code. In a similar manner to the BoltzTrap code BoltzWann uses the relaxation-time approximation and a "rigid band" approach to obtain the transport coefficients as functions of the electron chemical potential and temperature as described in Section 3.2.2.

4.3   Results and discussion

4.3.1   Cation disorder

The 5 possible configurations for the $1 \times 1 \times 1$ unit cell (tetragonal cell with 2 formula units) were generated using the SOD program and the probability of their formations are shown in Table 4.1 alongside multiplicity factors from experimental neutron diffraction measurements. The results clearly show no disorder in the Ag-containing structures. They are ordered in the kesterite I configuration as the probabilities of all the other configurations are zero and are not investigated further. In the Cu-containing structures there is disorder between the two kesterite configurations, again with the other structures having practically a zero probability of formation. To investigate the disorder in the Cu-containing structures calculations were performed in a $2 \times 2 \times 1$ supercell generating 255 possible inequivalent configurations. Out of these 255 configurations, only configurations with an equal number of A and B cations in the $z = 0.25$ and 0.75 planes (kesterite I and kesterite II) where investigated due to the large energy differences between those and the other configurations. This led to calculations being performed on 108 out of the 255 possible configurations. The formation probabilities are shown in Table 4.2. The results are consistent with the results obtained in the unit cell, suggesting that the nature of disorder in kesterites is simply a sort of

stacking disorder of the Cu/Zn planes, while Cu and Zn atoms are still highly ordered within the planes (checkboard pattern).

Table 4.1. Probability distribution at 300 K between the two kesterite configurations and the occupancy factors for each cation position in the $I\bar{4}$ spacegtoup from neutron diffraction measurements.

	Kesterite I	Kesterite II	Site Occupancy			
			2c	*2d*	*2a*	*2b*
CZGS	0.57	0.41	0.67(1) Cu 0.33(1) Zn	0.33(1) Cu 0.67(1) Zn	1 Cu	1 Ge
CZGSe	0.6	0.39	0.71(1) Cu 0.29(1) Zn	0.29(1) Cu 0.71(1) Zn	1 Cu	1 Ge
CZTS	0.57	0.38	0.945(9) Cu 0.055(9) Zn	0.055(9) Cu 0.945(9) Zn	1 Cu	1 Sn
CZTSe	0.60	0.37	0.92(2) Cu 0.08(2) Zn	0.08(2) Cu 0.92(2) Zn	1 Cu	1 Sn
AZTS	1.00	0.00	1 Ag	1 Zn	1 Ag	1 Sn
AZTSe	1.00	0.00	1 Ag	1 Zn	1 Ag	1 Sn
AZGS	1.00	0.00	No available experimental data			

Table 4.2. The probability distribution at 300 K between the two kesterite configurations in a 2 × 2 × 1 supercell).

	Kesterite I	Kesterite II
CZTS	0.82	0.18
CZTSe	0.86	0.14
CZGS	0.79	0.21
CZGSe	0.85	0.15

Comparing the relaxed lattice parameters (Table 4.3) the c / a value for the Ag structures is lower than for the Cu structures. This can be explained as the Ag^+ is bigger than the Cu^+ cation, but the c direction is more rigid due to the presence of the …S-(Sn,Ge)-S-Zn-S-… sequences. Table 4.4 compares the lattice parameters and c / a value for kesterite I and II and shows a lower c / a value for the kesterite I Ag structures.

Table 4.3. DFT results for the average cell parameters at 300 K and refined lattice parameters

	DFT calculations			Neutron Diffraction		
	a (Å)	c (Å)	c/a	a (Å)	c (Å)	c/a
CZTS	5.458	10.860	1.990	5.43218(3)	10.8308(1)	1.994
CZTSe	5.743	11.409	1.987	5.69544(5)	11.3417(2)	1.991
CZGS	5.364	10.512	1.960	5.34333(2)	10.51126(6)	1.967
CZGSe	5.657	11.079	1.958	5.60873(2)	11.04297(6)	1.969
AZTS	5.850	10.886	1.861	5.81261(3)	10.77886(7)	1.854
AZTSe	6.109	11.453	1.875	6.04419(3)	11.30653(9)	1.871
AZGS	5.772	10.439	1.809	No available experimental data		

Table 4.4. Calculated lattice parameters for kesterite I and II

	Kesterite I			Kesterite II		
	a (Å)	c (Å)	c/a	a (Å)	c (Å)	c/a
CZTS	5.461	10.854	1.988	5.458	10.856	1.989
CZTSe	5.744	11.406	1.986	5.744	11.405	1.986
CZGS	5.365	10.508	1.959	5.365	10.512	1.959
CZGSe	5.657	11.081	1.959	5.659	11.073	1.957
AZTS	5.850	10.886	1.861	5.836	10.932	1.873
AZTSe	6.109	11.453	1.875	6.098	11.490	1.884
AZGS	5.772	10.439	1.809	5.764	10.461	1.815

Table 4.5 shows the Bader charge analysis from the DFT calculations. In kesterite I, the interplanar Zn-Zn repulsion is lower than in kesterite II, due to shift between consecutive planes. This stabilisation is responsible for ordering in the Ag-series. The magnitude of this stabilisation decreases with the c/a value and is not seen with the Cu^+ series as the Zn-Zn repulsion decreases with an increase in the c/a value. Therefore, the stabilisation of configuration I is weaker in the Cu-series than in the Ag-series leading to disorder in the Cu-series.

Table 4.5. Bader Analysis

(Charges calculated using most stable configuration (kesterite I))

Formal charges	Total Electrons	AZTS	AZGS	CZTS	CZTSe	CZGS	CZGSe
Ag^{1+}	11	0.42	0.43				
Cu^{1+}	11			0.46	0.38	0.48	0.37
Zn^{2+}	12	0.97	0.98	0.95	0.81	0.94	0.83
Sn^{4+}	14	1.57		1.56	1.27		
Ge^{4+}	14		1.45			1.47	1.00
S^{2-}	6	-0.85	-0.82	-0.86		-0.85	
Se^{2-}	6				-0.71		-0.64

The relaxed lattice parameters and charges were then used to calculate the relative energies of the configurations using just the electrostatic interactions. This was performed using interatomic potentials with the General Utility Lattice Program (GULP).[182] The code calculates the lattice energy based on potential models or point charges of periodic systems. In this work, no potential models were used as the relaxed lattice parameters and charges were calculated at the DFT level, so the energies were calculated based solely on the point charges. The results are shown for the Sn phase and Ge phases in Table 4.6 and Table 4.7 respectively. The electrostatic-only energies are more similar for the two kesterite configurations in the Cu series, while in the Ag series kesterite I is clearly favoured. This confirms that the different behaviour of the Cu- and Ag- series is due to electrostatic factors.

Table 4.6. Electrostatic energies (calculated using GULP and the Bader charges from the ordered kesterite results)

	CZTS		AZTS	
	Electrostatic Energy (eV)	Relative (eV)	Electrostatic Energy (eV)	Relative (eV)
Kesterite I	-63.18	0.00	-57.56	0.00
Kesterite II	-63.13	0.05	-57.40	0.16

Table 4.7. Electrostatic energies (calculated using GULP and the Bader charges from the ordered kesterite results)

	CZGS		AZGS	
	Electrostatic Energy (eV)	Relative (eV)	Electrostatic Energy (eV)	Relative (eV)
Kesterite I	-63.60	0.00	-60.16	0.00
Kesterite II	-63.66	-0.06	-59.52	0.64

4.3.2 Band structures

The electronic band-structures of the series between high-symmetry points are shown in Figure 4.3. For all compounds the band-structures are similar, except for a band translation. The band-structures show that they are direct band-gap semiconductors. The substitution of S for Se acts to decrease the band gap, whereas the substitution of Cu with Ag or the substitution of Ge for Sn acts to increases. These results are consistent with experimental results which report a band gap for CZTS at around 1.5 eV[167-174, 183] and CZTSe ~1.0 eV (Table 4.8).[175-177] They also show the valence band maximum is not changed but rather the change in the band gap is the result of a shift in the conduction band with respect to the vacuum, in agreement with Zhao *et al*.[178]
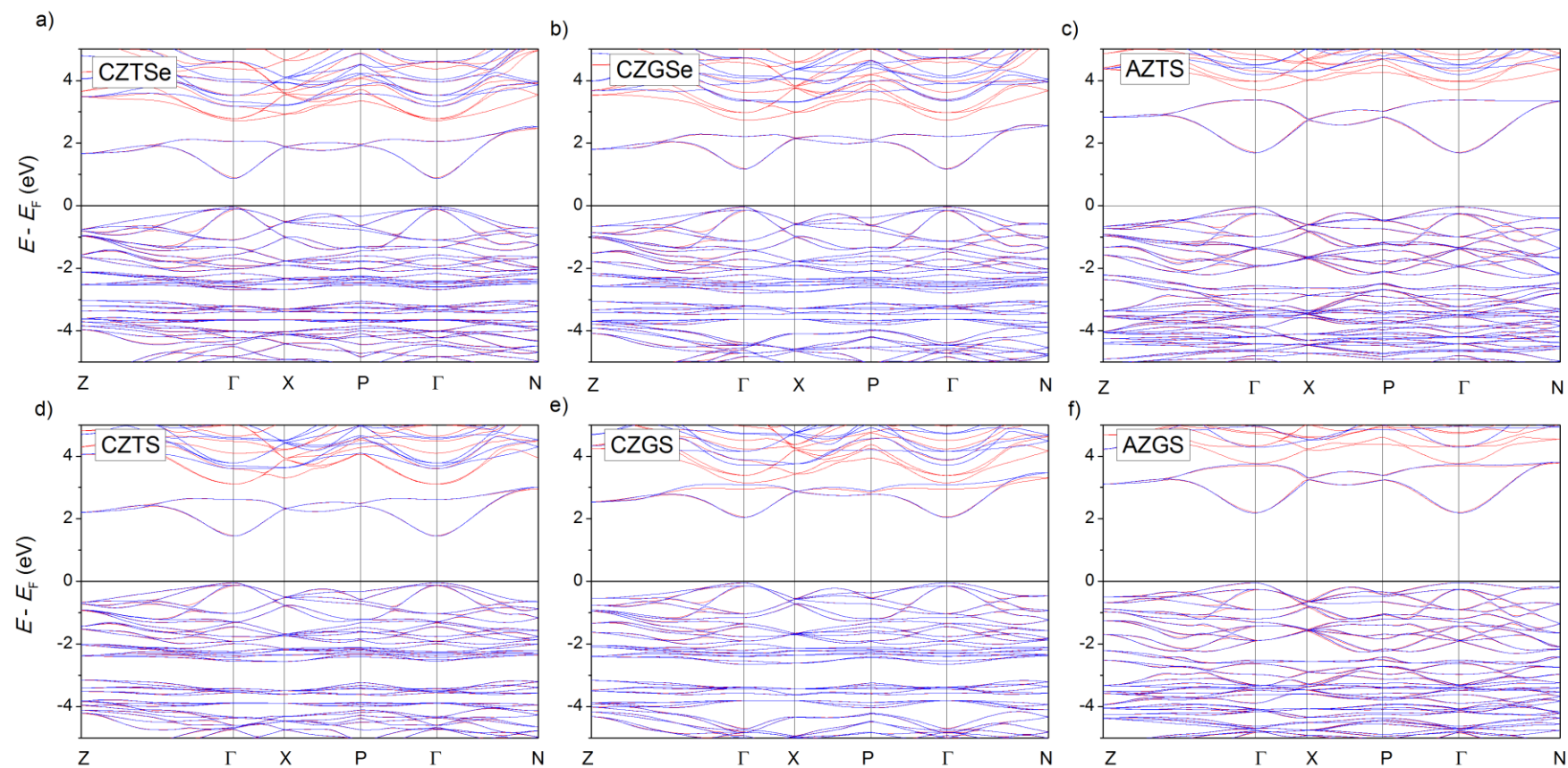
Figure 4.3. Band structure of kesterite I for each system, red lines are the original DFT calculated band structure and the blue lines are the Wannier interpolated band structure.

On further analysis for each composition the band gap is reported for kesterite I and II in Table 4.8. Consistent with experimental results the smallest band gaps are for the selenide compositions[175-177] with the largest band gaps seen in the germanium sulphides.[166, 184] Differences in the band gaps between the two kesterite system appear minimal for CZTS and CZTSe, but are more pronounced in the germanium and silver compositions. The band gap variations as a function of configuration supports the theory that disorder between configurations could cause the reduction in the open cell voltage seen in solar cells. In CZTS and CZTSe the difference is only around 0.03 eV; this small difference suggests there may be additional reasons for the reduction in the open-circuit voltage.

Table 4.8. Band gap analysis of different compositions of the A_2BCX_4 system (eV)

	Kesterite I	Kesterite II	Experiment
CZTS	1.49	1.46	1.47 - 1.51 [167-174, 183]
CZTSe	0.91	0.88	0.97-1.04 [175-177]
CZGS	2.09	2.04	1.88–2.20[166, 184]
CZGSe	1.26	1.17	1.40–1.43[184]
AZTS	1.74	1.56	2.00[166]
AZTSe	1.08	0.92	1.40[185]
AZGS	2.23	1.97	2.50[166]

4.3.3 Electron transport

The kesterite structures are promising as intermediate temperature thermoelectric materials, with potential operating temperatures in the region of 500-900 K.[14, 15] Theoretical work has shown that in direct-gap thermoelectric materials the optimum gap is in the region of nk_BT where n is between 6-10 or in some cases greater than 10, dependent on the dominant scattering mechanism in the material.[186] This gives an optimal band gap in the region of 0.3 – 0.7 eV. Taking this into consideration the Boltzmann transport analysis is performed only on the CZTSe system which has the smallest band gap of the calculated structures. The band gap is shown in Figure 4.4a which is in excellent agreement with experimental results (Table 4.8) and is consistent with the band structure (Figure 4.3).

A. DOS and the Seebeck coefficient

Boltzmann transport analysis is performed using the interpolated DOS (Figure 4.4a) and band-structure (Figure 4.3). The DOS shows a large asymmetry between hole and electron doping. As the chemical potential is shifted into the valence bands the number of holes increase rapidly due to the large gradient of the DOS. This is also reflected in Figure 4.4c which shows the relationship between the chemical potential and carrier concentration.

As in Section 3.3 the Seebeck coefficient can be fully predicted within the constant relaxation-time approximation. Figure 4.4b shows the Seebeck coefficient as a function of carrier concentration at 300 and 500 K. At the Fermi level and at 300 K the material is calculated as n-type. At 500 K, the reduction in the Seebeck coefficient is related to the larger smearing of the Fermi-Dirac distribution. A lower gradient in the

Fermi-Dirac distribution and a higher temperature reduces the Seebeck coefficient through Equation (2.38). As the chemical potential is reduced, there is a reduction in the number of electrons (n); which leads to an excess of holes (p) and the material is calculated as p-type (p-$n > 0$). As the chemical potential is reduced further there is a continued build-up of holes until a peak in the Seebeck coefficient is reached. Then the Seebeck coefficient decreases again, due to the increased conductivity of the carriers.

As the chemical potential is shifted into the valence band the number of holes increase rapidly. Figure 4.5a shows the Seebeck coefficient as a function of charge carrier concentration over a large range, whereas Figure 4.5b focuses on a narrower linear region which are in the region typically reported for this structure. At experimentally reported carrier concentrations (1×10^{19} to 3.1×10^{20} cm^{-3}), Figure 4.5 indicates that the compounds will exhibit a positive Seebeck coefficient (p-type) which is in line with experimental results.[159, 187, 188] The experimentally reported carrier concentrations are large for un-doped systems and the large differences reported maybe due to experimental measurement techniques,[174, 189-193] or the possibility of p-type secondary phases,[159, 168, 194] or the deviation from unity of Cu/Zn in the compositions, as reported by Chen *et al*.[195] The substitution of just one Cu for Zn in a $2 \times 2 \times 2$ supercell of 128 atoms ($< 1\%$) would lead to one additional electron with a resulting carrier concentration of around 3.3×10^{20} cm^{-3}.[195] To determine the effect of doping on the transport properties of CZTSe the analysis is performed within the rigid band approximation, where the density of states of the doped system keeps the same shape as that of the pure system.
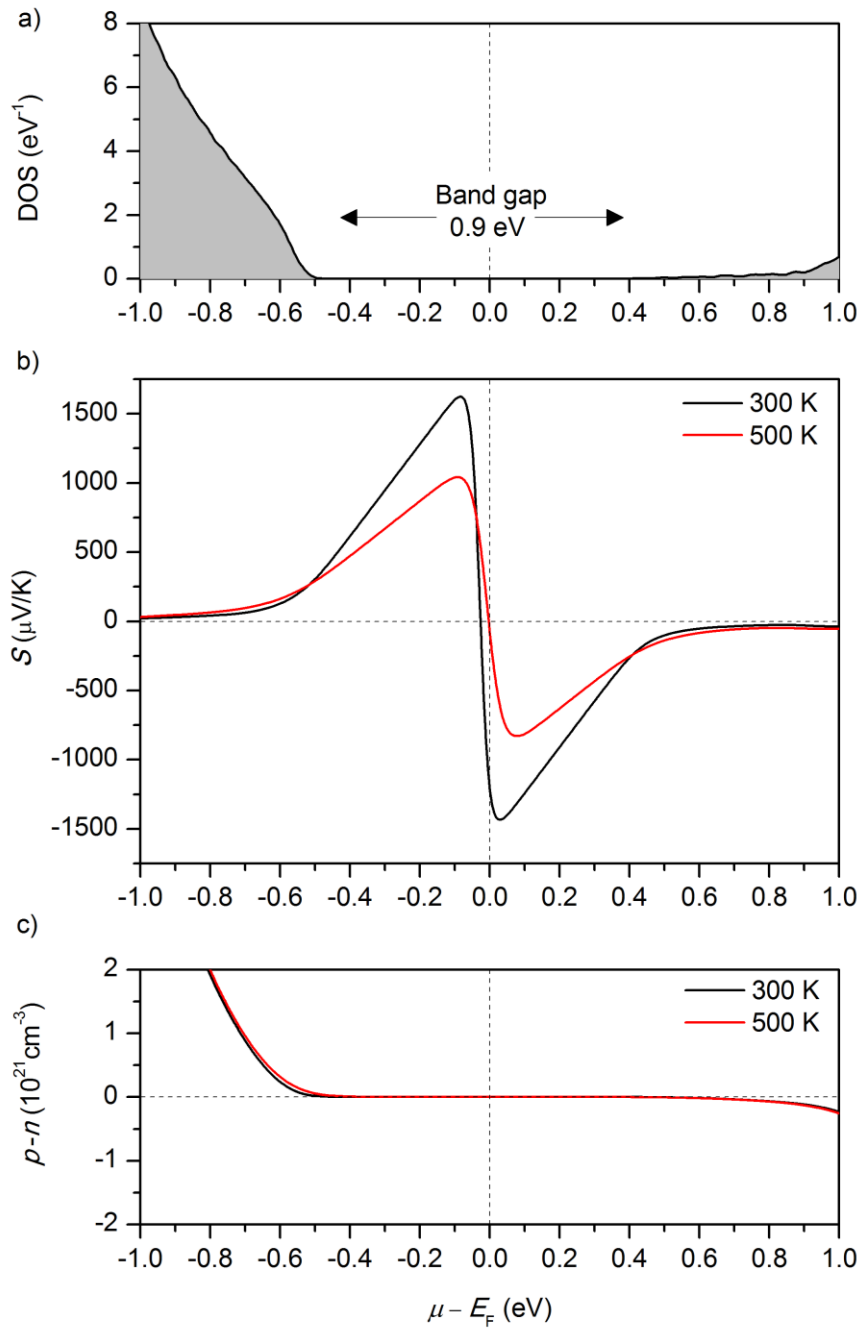
Figure 4.4. (a) Wannier interpolated DOS, (b) Seebeck coefficient, and (c) carrier concentration at 300 and 500 K as a function of chemical potential for CZTSe.
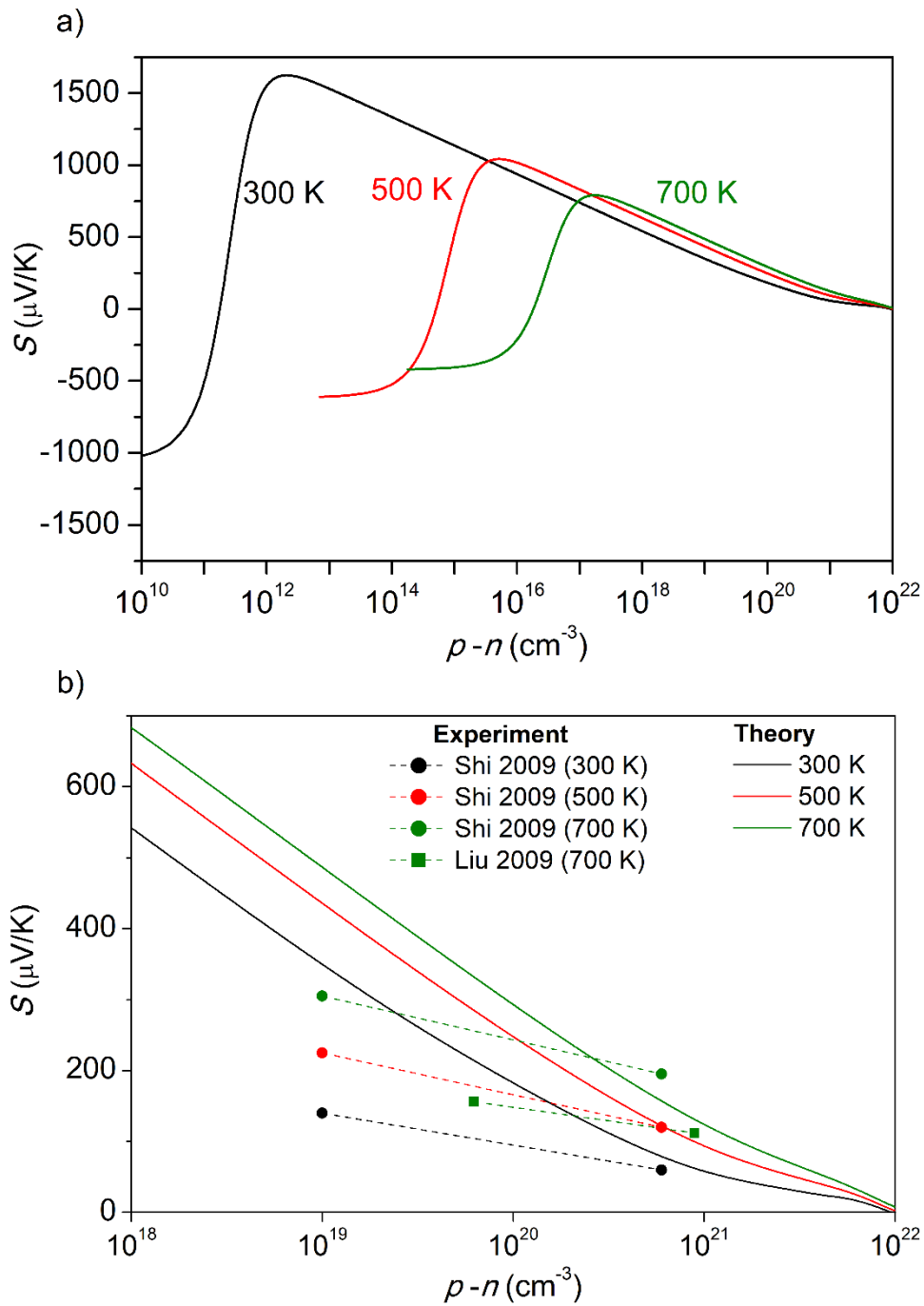
Figure 4.5. Seebeck coefficient against carrier concentration for CZTSe over (a) a large range of carrier concentrations and (b) only in the linear region. Experimental data taken from Ref [187] and [188].

Figure 4.5b focuses in on the linear region of variation of the Seebeck coefficient with log (p-n) and experimental data is also shown. In this region, a reduction in the carrier concentration leads to an increase in the Seebeck coefficient, these results are in semi-quantitative agreement with experiment. The increase in the Seebeck coefficient with temperature is also seen in both theory and experiment. Different experimental results do show large variations in the Seebeck coefficient, although the change in the gradient of the Seebeck coefficient with carrier concentration is higher in the calculations than in experiment. This may be due to second phases in experimental synthesis, ZnSe, CuSe and SnSe have all been reported experimentally.[159, 168, 194] ZnSe has a negative Seebeck coefficient and has an adverse effect on the total Seebeck coefficient due to negative charge carriers.[159] The difference in the gradient may also be due to the inaccuracy of the rigid band approximation used in our calculations. To explicitly include the effect of doping on the band structure, supercell calculations would be needed and could be performed in future work.

B. Electronic conductivity and scattering rates

As in Section 3.3 the electronic conductivity cannot be predicted explicitly, but is calculated per unit of relaxation time (σ/τ). The combination of our calculations with experimental measurements of the electronic conductivity are performed in order to analyze the behaviour of the effective isotropic relaxation time.

The σ/τ has only a very weak dependence on temperature (Figure 4.6a) but at the higher carrier concentration, σ/τ is higher due to the increased number of available carriers. As discussed in Section 2.2.1 and 3.3, in metallic systems and above the Debye temperature impurity scattering rates are independent of temperature and phonon

scattering rates increase linearly with temperature. In contrast to metals, in semiconductors, impurity scattering is proportional to $T^{-3/2}$, whereas phonon scattering is proportional to $T^{3/2}$. This follows from Equation (2.46), excluding the electron-electron scattering term which is negligible. To obtain a linear dependence, $T^{3/2}\tau^{-1}$ is plotted against T^3:

$$\frac{T^{3/2}}{\tau} = a_{im} + a_{ph}T^3 \tag{4.1}$$

The results are shown in Figure 4.6b with experimental data taken from Liu et $al.$[188] At each temperature the carrier concentration is fixed to that experimental carrier concentration. This represents the extrinsic doping found experimentally and the scattering coefficients are detailed in Table 4.9 and shown in Figure 4.6b.

Table 4.9. Scattering coefficients at varying carrier concentrations

	a_{im}	a_{ph}
6.2×10^{19} cm^{-3}	3.28×10^{17}	4.61×10^9
8.9×10^{20} cm^{-3}	2.04×10^{18}	1.64×10^{10}

Consistent with expectations at the lower carrier concentration of 6.2×10^{19} cm^{-3} lower scattering rates for both impurities and phonons are reported. The linear fitting at 6.2×10^{19} cm^{-3} is in excellent agreement with experiment, but the linear fitting at the higher carrier concentration (8.9×10^{20} cm^{-3}) is slightly inaccurate. This may be due to experimental errors in the measurement of the conductivity or carrier concentration, second phases present in the samples or the failure of the model within the rigid band approximation. This is further illustrated in Figure 4.6c where the fitted coefficients are used to obtain the conductivity as a function of temperature. The fitting at 6.2×10^{19} cm^{-3}

is in good agreement with experiment, but the fitting at 8.9×10^{20} cm^{-3} is slightly inconsistent with the experimental results. It is interesting to note the range of the scattering rates obtained. Across the whole temperature range from $300 - 700$ K the scattering rates for a carrier concentration of 6.2×10^{19} cm^{-3} varies from $0.9 - 1.0 \times 10^{14}$ compared to $3.7 - 4.5 \times 10^{14}$ at the higher carrier concentration of 8.9×10^{20} cm^{-3}. These scattering rates are consistent with scattering rates approximated to 1.0×10^{14} s^{-1} within the relaxation time approximation.
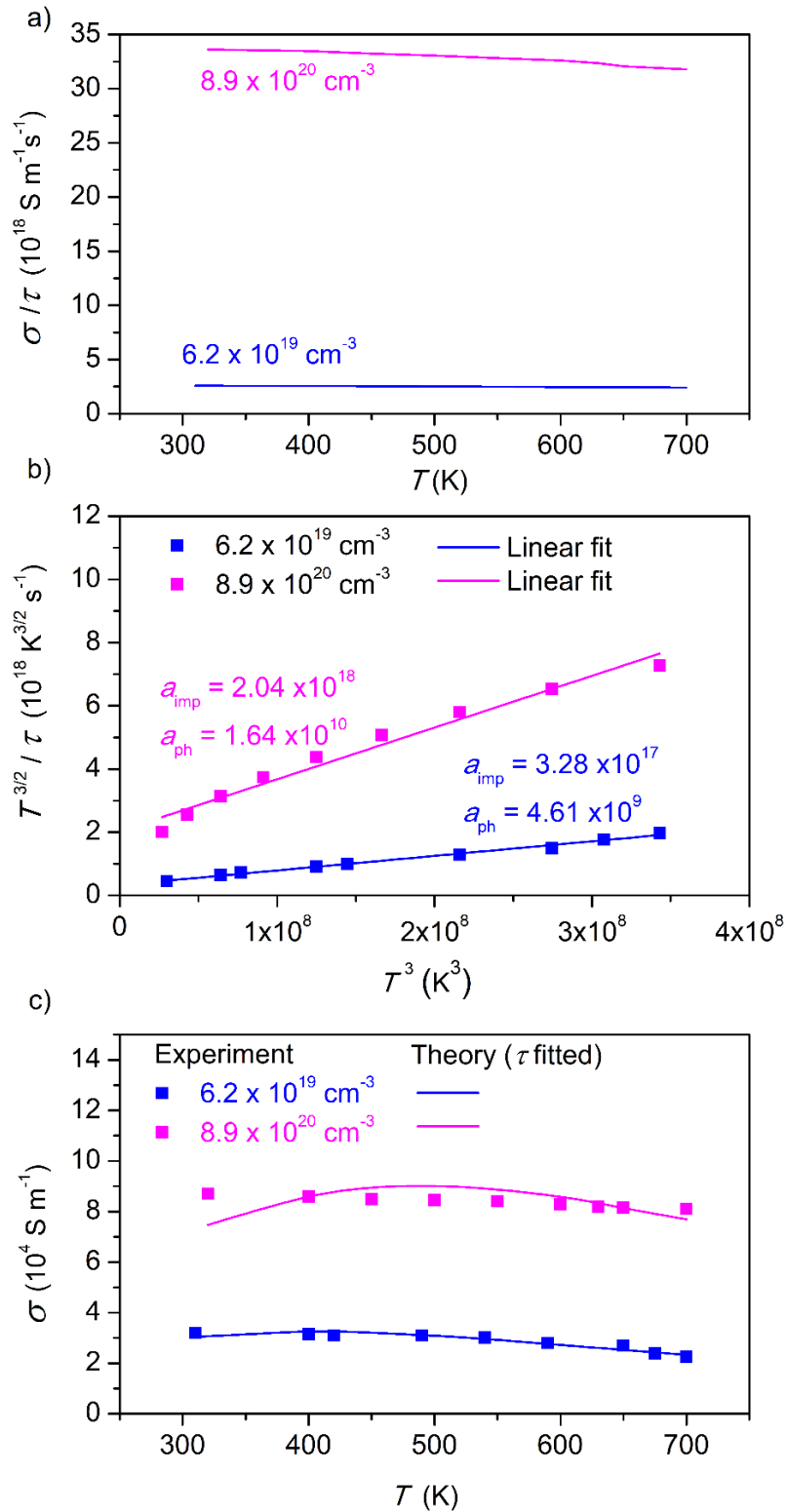
Figure 4.6. (a) Calculated electronic conductivity per unit of relaxation time (σ/τ). (b) Scattering rates obtained using the experimentally determined σ and the theoretically obtained σ/τ, and the fitting of its temperature dependence. (c) Experimental electronic conductivity data from Liu *et al.*[188] and calculated values using fitted τ (*T*).

C. Transport properties as a function of carrier concentration

The scattering coefficients at the two different carrier concentrations (Table 4.9) are linearly interpolated to obtain scattering rates as a function of p-n. The scattering rates determined in this way are then used to calculate σ and κ_{el} as a function of function of p-n and these results are shown Figure 4.7 and Figure 4.8 respectively.
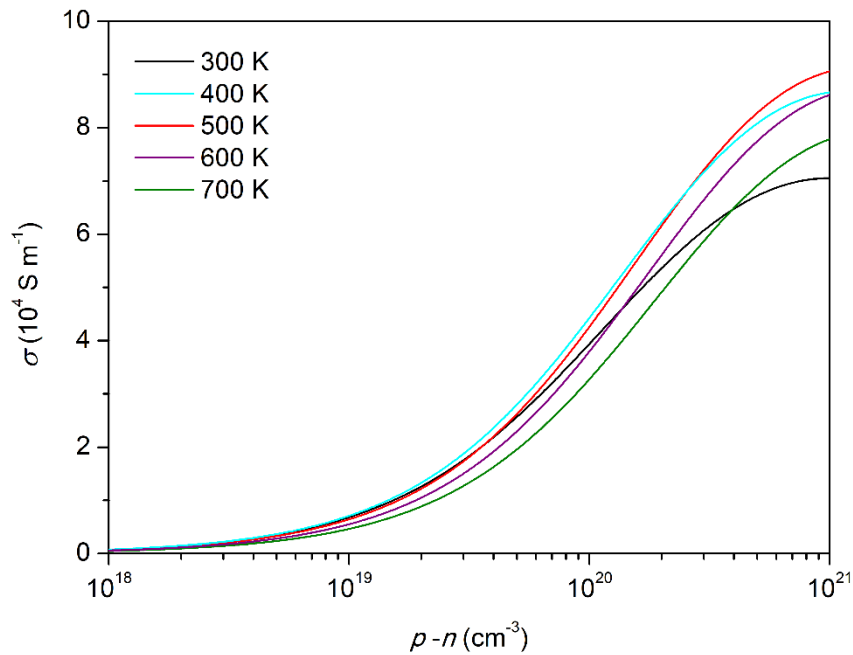
Figure 4.7. σ as a function of carrier concentration

Figure 4.7 shows that σ increases as a function of carrier concentration due to the increased number of available carriers. The rate of the increase decreases due to an increase in the scattering rates observed at higher carrier concentrations. The variation of σ as a function of T is due to the two competing scattering mechanisms, impurity and phonon scattering. At 300 K, the fitting of the scattering rates suggests impurity scattering has a more weight than at higher temperatures leading to lower conductivities. As the temperature increases impurity scattering becomes less significant due to its $T^{-3/2}$ relationship. In contrast at higher temperatures phonon scattering which has a $T^{3/2}$

relationship results in a decrease in σ, this can be seen at 600 K where there is a small decrease in σ and then a further increase at 700 K.

Figure 4.8 shows the electronic thermal conductivity as a function of carrier concentration. As the number of carriers increase, κ_{el} increases as expected. The variation with carrier concentration approximately follows the conductivity (Figure 4.7). Slight differences can be is due to the variation of the Lorenz factor which varies with carrier concentration (Figure 4.9).[8]
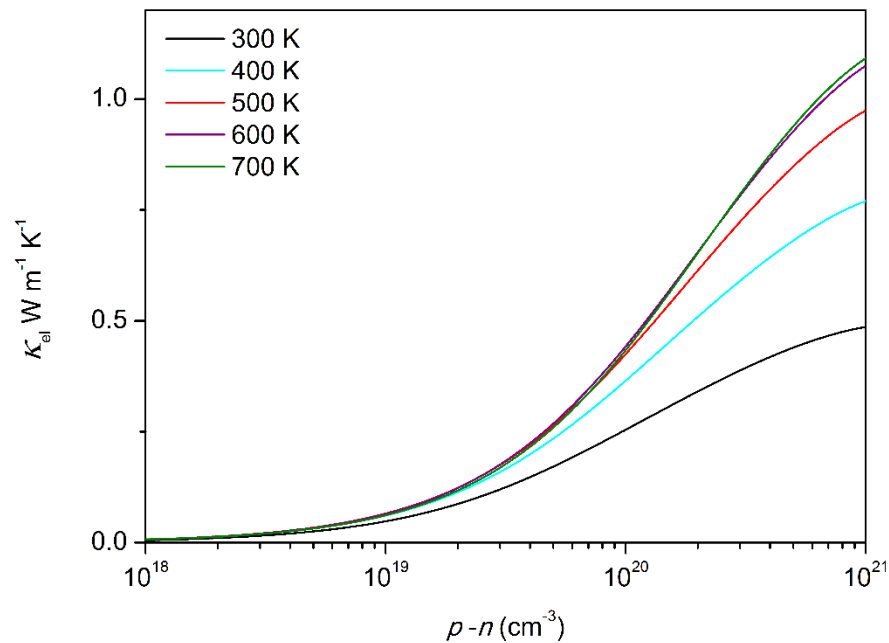
Figure 4.8. κ_{el} as a function of carrier concentration
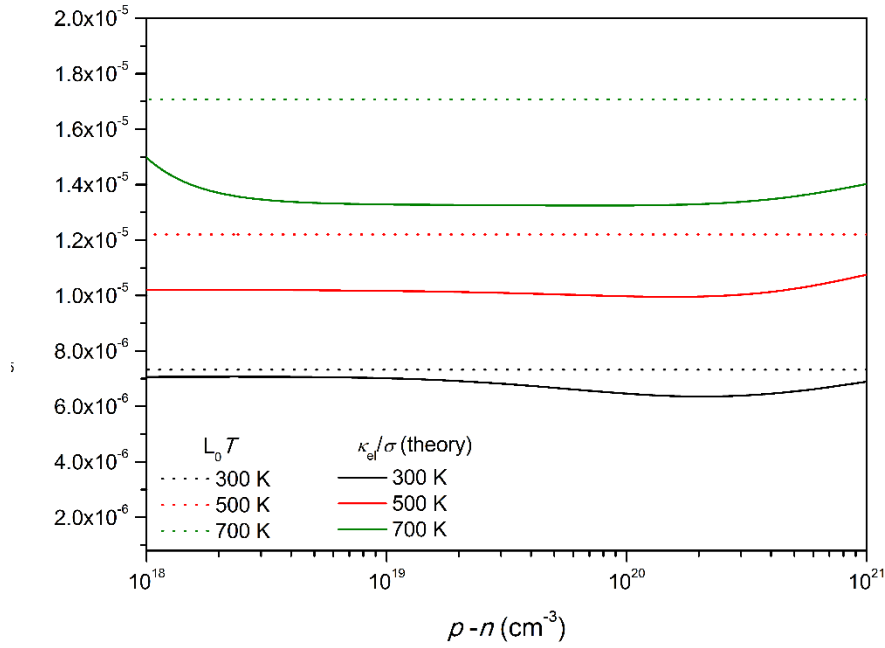
Figure 4.9. $\kappa_{\mathrm{el}}/\tau$ **shown as a function of carrier concentration. The Lorenz number multiplied by temperature is shown with dotted lines.**

The total thermal conductivity can be calculated by including the lattice contribution to the thermal conductivity under the approximation that there is no change in lattice thermal as the carrier concentration varies. Lattice thermal conductivities are taken by calculations performed by Skelton *et al.*[196] At 300 K Skelton *et al.* report the lattice thermal conductivity to be about 4 W m^{-1} K^{-1}, which would clearly be the dominant contribution to thermal heat transport. At higher temperatures as phonon-phonon scattering becomes more significant the lattice contribution decreases to around 2 W m^{-1} K^{-1} at 700 K is closer to the κ_{el} contribution. This contrasts with metallic systems where κ_{el} dominates thermal transport.

The thermoelectric behaviour of CZTSe can be summarized by calculating its *ZT*. and has been done as a function of carrier concentration at various temperatures (Figure 4.10). The *ZT* is mainly determined by the Seebeck coefficient which increases as the carrier concentration decreases. The peak in the *ZT* is seen at a carrier concentration of

around 1×10^{20} cm^{-3}. At higher carrier concentrations, the increase in the electrical conductivity is offset by the reduction in the Seebeck coefficient leading to a reduction of the *ZT*. As the gradient of the Seebeck coefficient as a function of carrier concentration is larger in the theoretical calculations compared to experiment[159, 187, 188] (Figure 4.5) the peak in the *ZT* in experiment would be shifted to higher carrier concentrations.
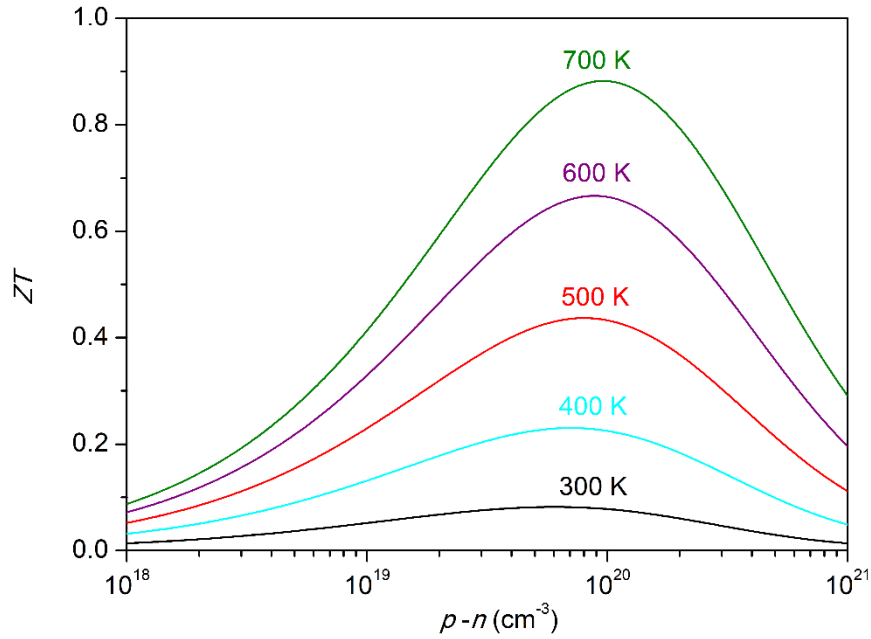
Figure 4.10. Theoretical *ZT* as a function of carrier concentration

4.3.4 Conclusions

A combined theoretical and experimental study of the ordering of the A and B cations in the quaternary chalcogenides has been reported. Theoretical results predict the Ag$^+$ structures to be fully ordered in the kesterite I configuration. These results are confirmed by neutron diffraction measurements. The *c* / *a* value is lower in the Ag$^+$ series than in the Cu$^+$ series. Zn-Zn repulsion is lower in the kesterite I configuration, due to a shift between consecutive planes. As Zn-Zn repulsion decreases with an increase in the *c* / *a* value the Ag-series is ordered but the Cu-series is disordered.

DFT calculations performed with the HSE06 functional obtained band gaps in reasonable agreement with experiment for the investigated structures and in the range of 0.9 – 2.2 eV. Band-structure calculations confirm the structures as direct band-gap semiconductors.

Configurational disorder has been suggested to lead to band gap fluctuations that cause a reduction in their open-circuit voltage, limiting their efficiency. This would not be expected in the Ag series as they have been found to be fully ordered. In CZTS and CZTSe calculated band gaps differ by only 0.03 eV which support to some degree a reduction in the open-circuit voltage due to the band gap. Other contributing factors are likely to play a role in their low open-circuit voltage. The first is the presence of neutral defect clusters such as $Cu_{Zn} + Zn_{Cu}$ which is supported by the clear disorder found in these structures and the second the presence of secondary phases like ZnSe, CuSe and SnSe, all of which have been reported experimentally.

For their use as intermediate thermoelectric materials the optimal gap would be in the region of around 0.3 – 0.7 eV, suggesting that the structures would not be good thermoelectric candidate materials without doping or further substitution. The investigation of CZTSe which has the smallest band gap suggests that its ZT can be improved by doping. The experimentally reported Seebeck coefficient generally has a smaller gradient as a function of carrier concentration than calculated in this work. This leads to the optimal ZT being shifted to higher carrier concentrations, where the increase in conductivity has more weight than the decrease in the Seebeck coefficient in the calculation of the ZT. This is nevertheless encouraging, with the confirmation that the ZT can be optimised through hole doping. This work also suggests a combined theoretical

and experimental approach to the optimisation of the ZT as a function of carrier concentration.

5   Porphyrin metal-organic frameworks (PMOFs)

In this Chapter, we present the results of a collaborative research effort for the theoretical investigation of porphyrin based MOFs. The DFT, electronic structure and band alignment calculations were performed by myself. Dr A. Rabdel Ruiz-Salvador performed the analysis of determining the distance from a pore centre to the framework atoms, which was used to pick the pore position furthest away from the framework atoms to calculate the vacuum potential. The free energy of cation exchange was done by Dr S. Hamad. The configurational disorder analysis using SOD and the calculation of the equilibrium probability distribution using an Ising model was performed by my supervisor Dr R. Grau-Crespo.

5.1   Introduction

The solar-driven synthesis of fuels, such as hydrogen[28, 197] or organic fuels like methanol,[16, 17, 198] offers great potential for clean and renewable energy, so there is a growing interest in pursuing alternative photocatalytic materials for the design of new efficient photocatalysts. MOFs are porous crystalline materials, created by joining organic linkers through coordination nodes, which can be either single metal atoms or metal-containing clusters. MOFs are being widely used in fields like adsorption, separation and catalysis due to their extraordinary properties and versatility.[57, 199-204] Their choice as photocatalysts is also stimulated by their diverse porous architectures,[200, 202] which confer them exceptional molecular adsorption properties.[202-204] The adsorbed reactant molecules can access the active sites embedded in a confinement field that favours the catalytic reactions[205]. Their porous structure and framework also allows for the possibility of storing produced gases. The properties of these MOFs can be tuned by changing factors such as topology, metal composition or the nature of the linkers.[206, 207] Understanding the impact these changes have on the electronic structure of MOFs is key

to optimising them for photocatalytic reactions. Recent studies have suggested that there is great potential in optimising the electronic structure by chemical and structural changes in MOFs. Gascon *et al.*[208] showed that the band gap of MOF-5 could be lowered by modifying the linker properties. The magnetic and optical properties can also be tuned by the composition of the metal centres.[209, 210]

In contrast to semiconductor photocatalysts, in terms of their electronic behaviour, MOFs are typically regarded as molecular-like catalysts.[211] Fateeva and co-workers[62] investigated the properties of a MOF containing porphyrins connected through phenyl-carboxyl ligands and AlOH species, referred to as Al-PMOF. The structure of this PMOF is shown in Figure 5.1 in its conventional orthorhombic configuration. The metal can either be located at the centre of the porphyrin (porphyrin metal centre) or as the linker site (octahedral metal centre). Fateeva and coworkers[62] showed that the optical and photocatalytic properties of this PMOF is mainly determined by its linker, they observed a strong absorption band at 415 nm (2.99 eV) and four lower energy bands, which are characteristic of the free porphyrin molecule in solution. In agreement with work by Rosseinsky *et al.*[62]

In solution the metalation of the porphyrin molecule can in principle be modified by the presence of metal (M) cations within the ring,[212] For example, metalation of Al-PMOF with Zn has been investigated to improve the efficiency of photocatalytic water splitting,[62] while CO_2 conversion is improved by Cu incorporation,[213] as well as by the modification of the linker atom.[208] Metalation of the porphyrin units by Zn and Cu has also been shown to enhance photocatalytic water splitting[62] and CO_2 conversion[213] respectively.
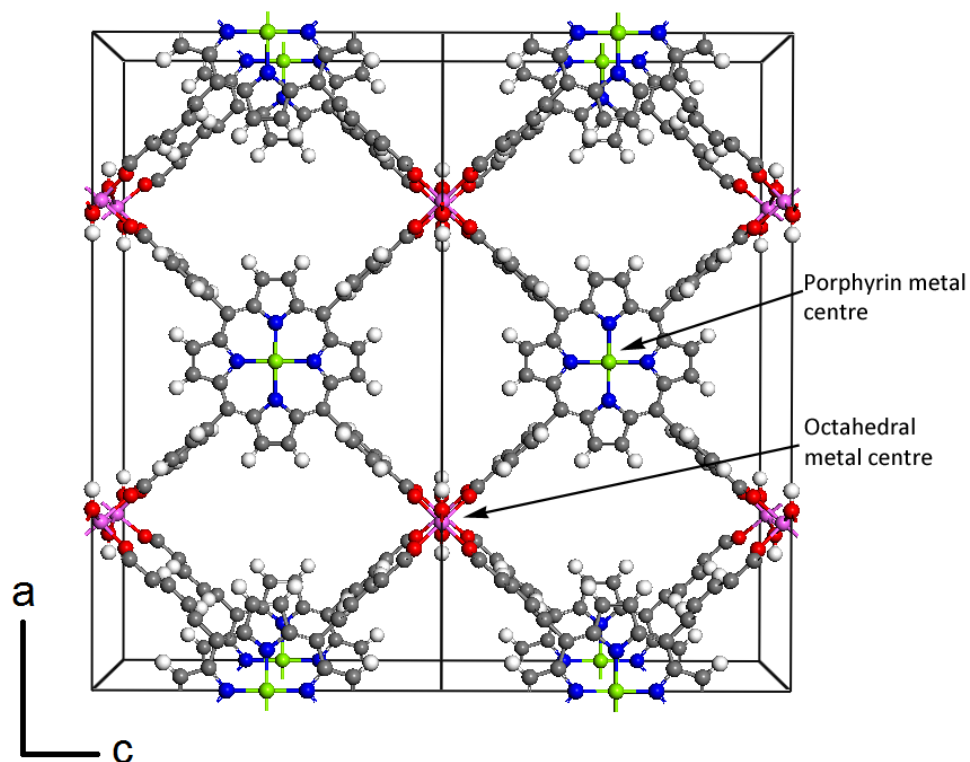
Figure 5.1. Perspective view of the conventional unit cell (doubled for clarity) for the porphyrin-based MOF investigated in this study, indicating the positions of the octahedral metal centre and the porphyrin metal centre. Colour code: gray = carbon, white = hydrogen, red = oxygen, blue = nitrogen, magenta = octahedral metal centre, green = porphyrin metal centre.

To exhibit photocatalytic activity for water splitting the absolute band edges and band gap are important factors in their suitability and efficiency as photocatalysts. To investigate possible optimisation of the band edges this chapter focuses on two modifications to the Al-PMOF and the subsequent changes on its electronic properties. The first is the modification of the metallated Al-PMOF with different porphyrin metal centres, where Fe, Co, Ni, Cu are considered as alternatives to Zn and also compared to the di-protonated Al-PMOF. The second is the modification of the octahedral metal centre using Fe instead of Al in the Al-PMOF. This is motivated by the recent experimental success in incorporating iron at both the porphyrin centres and the octahedral sites,[63] as well as by the well-known ability of transition metal cations to contribute both occupied and unoccupied d levels around the Fermi energy, thus allowing band gap control. We

compare the effects of substituting Fe in the porphyrin and in the octahedral metal centres, as well as in both simultaneously. Finally, we will argue that the optimal electronic properties for photocatalysis, in terms of band gaps and band edge positions, is obtained from partial substitution of the Al cations by Fe in the octahedral sites, while keeping Zn at the porphyrin centres.

5.2   Computational details

5.2.1   Porphyrin metal centre substitution

In order to maximise computational resources calculations were performed on the primitive cell of the PMOF containing half the amount of atoms as the conventional orthorhombic cell (space group Cmmm)[62] (Figure 5.1), leading to only one porphyrin per cell. Inside the porphyrin, bonding to the N atoms, the metal centre was modified to include either two hydrogens, or a late $3d$ transition metal cation (Fe^{2+}, Co^{2+}, Ni^{2+}, Cu^{2+} or Zn^{2+}). DFT calculations were performed using the PBE functional,[69] and during relaxation forces on the atoms were minimized until they were all less than 0.01 eV/Å.

For each of the metal ions, all possible spin states were considered. For Fe^{2+} (d^6 ion) there can be 0, 2 or 4 unpaired electrons, which correspond to low-spin (LS), intermediate-spin (IS) and high-spin (HS) configurations. For Co^{2+} (d^7) there can be either 1 (LS) or 3 (HS) unpaired electrons, whereas for Ni^{2+} (d^8) there can be either 0 (LS) or 2 (HS) unpaired electrons. Finally, there is one possible spin state for Cu^{2+} (d^9) with one unpaired electron, whereas Zn^{2+} is not spin-polarized. In each calculation, the difference in the number of up- and down-spin electrons was constrained to the corresponding integer number given above. As there is only one metal atom per cell, all the spin-polarized calculations correspond to ferromagnetic configurations. Considering the relatively large distance between magnetic metal ions (ca. 6.7 Å in the direction perpendicular to the porphyrin plane) and the absence of common ligands, it can be

expected that the strength of the magnetic coupling will be very small and that the actual structure is paramagnetically disordered at room temperature. The weak magnetic coupling implies that there must be very small energy differences associated with magnetic ordering in these structures, and therefore the simulation results should be independent on the magnetic order assumed.

In order to obtain accurate electronic structures single-point calculations on the relaxed structures (with the most favourable spin state for each composition), were performed with the screened hybrid HSE06 functional.[76, 77] which generally provides bandgaps in closer agreement with experiment than those from GGA functionals.[78] The projector augmented wave (PAW) method[73, 74] was used to describe the frozen core electrons and their interaction with the valence electrons, *i.e.* those in level $4d$ for Fe, Co, Ni, Cu and Zn, and $2s2p$ for C, N and O. The kinetic energy cutoff for the plane wave basis set expansion was set to 520 eV. A Γ-centred grid of $\boldsymbol{k}$-points was used for integrations in the reciprocal space, where the smallest allowed spacing between k-points was set at 0.5 Å^{-1}, giving rise to 3 irreducible points in the Brillouin zone corresponding to the primitive cell.

5.2.2 Octahedral metal centre substitution

Similarly, to the porphyrin metal centre substitution the primitive cell was used. Geometry optimizations were performed using the PBE functional,[69] but in this case van der Waals (vdW) corrections were included *via* the DFT-D2 method of Grimme.[80] The difference was introduced for this later work[214] in response to referee's comments to the earlier work. In practise, the introduction of vdW corrections has very little effect on our conclusions.[215] During relaxation, forces on atoms were minimized until they were all less than 0.01 eV/Å. Calculations were performed using the non-spin-polarized Zn^{2+} ion as well as the Fe^{2+} ion in the porphyrin metal centre. For the Fe^{2+} in the porphyrin metal

centre the lowest most stable spin state was used. In all calculations were Fe atoms were present, a Hubbard correction was applied to the Fe $3d$ orbitals, using Dudarev's approach[75] based on a single parameter U_{eff}, which was set to 4 eV. This value has been reported to provide a good description of the electronic structure of iron oxides.[216, 217]

With respect to the octahedral metal centre where there are two atoms per unit cell. Al^{3+} and Fe^{3+} where used or a mixture of the two. For calculations involving Fe all calculations were performed using spin polarisation and all possible spin states at the Fe centres were calculated. As with the porphyrin metal centre, the calculations were performed in the ferromagnetic configuration. Single point calculations were performed with the HSE06 functional.[76, 77] The PAW method was used to describe the frozen core electrons using the same settings as previously described for the porphyrin metal centre substitution as well as the same energy cutoff and k-spacing.

5.2.3 Band structures

The band structure was also investigated at the PBE+U level for the octahedral metal centres. A Γ-centred grid of k-points was used for integrations in the reciprocal space, where the smallest allowed spacing between k-points was set at 0.2 Å^{-1}, which corresponds to 18 irreducible points in the Brillouin zone. This grid is much denser that the one used for the HSE06 calculations, where the spacing was 0.5 Å^{-1} corresponding to only 3 irreducible points.

An additional linear mesh of 6 points along each interval in the high-symmetry paths was employed to plot the band structures. The reciprocal space coordinates of the high-symmetry Brillouin zone points are: Γ (0,0,0), S (0,0.5,0), R (0,0.5,0.5), Z (0,0,0.5), Y (-0.5,0.5,0), and T (-0.5,0.5,0.5).

5.2.4 Band alignment

As in other periodic DFT codes, the band energies in VASP are given with respect to an internal energy reference (the average potential in the crystal). To obtain absolute band energies which can be used to compare to the potential of the hydrogen and oxygen evolution reactions it is necessary to align the band energies to the vacuum scale.

Evaluating the average potential within a small sphere (radius of 0.3 Å) at different positions in the pore and by finding the point that is farthest apart from the framework atoms (the pore "centre"), where the potential is locally flat (no electric field), a good approximation to the vacuum level can be found. This follows the methodology proposed by Butler *et al.*[82] to calculate the vacuum level in MOF structures and led to MOF ionization potentials in good agreement with experiment.[82] A Python code provided by these authors was employed in these calculations to obtain the potentials.[218]

5.3 Results and discussion

5.3.1 Substitutions at the porphyrin metal centre

A. Crystal structure

Metal cation substitution can occur at two distinct sites. At the porphyrin metal centre (M^{2+}) or at the octahedral metal centre (A^{3+}) of the PMOF. To specify each PMOF composition the notation (A^{3+}, M^{2+})PMOF is used. The first substitutions were performed at the porphyrin metal centre keeping the octahedral site fixed as an Al^{3+} cation and these are discussed first.

Upon replacement of the two H atoms at the porphyrin metal centre with the transition metal atoms, only small variations of cell parameters were observed (Table 5.1), with overall cell volume contractions between 0.1% and 0.6%. The calculated cell parameters are close to the experimentally measured values reported for (Al^{3+}, Zn^{2+})PMOF and (Fe^{3+},

Fe^{2+})PMOF.[62, 63] The metal-nitrogen interaction seems to be the main factor controlling the small changes of the cell volume. The calculations systematically overestimate all the cell parameters in comparison with experiment in Ref. [62] by an average of ~1%. However, the calculations are able to reproduce well the small variations observed experimentally in the cell parameters from the protonated to the Zn-substituted structure: a small contraction of the *a* parameter, a small expansion of the *c* parameter, while the *b* parameter remains roughly the same. Overall, a small contraction of the cell volume by is observed in both the experiment (0.31%) and the calculations (0.13%) upon Zn substitution.

Table 5.1. Calculated lattice parameters, cell volume and the two perpendicular N-N distances inside the porphyrin. All structures adopt the orthorhombic space group *Cmmm* (65), where α=β=γ=90⁰. Available experimental values at room temperature are given in parenthesis.

Cation	a (Å)	b (Å)	c (Å)	V (Å3)	d [N-N] (Å)*
2H⁺	32.196	6.722	16.964	3671.6	4.06/4.22
	(31.967)†	(6.6089)	(16.876)	(3565.3)	-
Fe²⁺	32.072	6.720	16.957	3654.8	3.96/3.96
Co²⁺	31.968	6.720	16.989	3649.3	3.92/3.93
Ni²⁺	31.996	6.723	16.964	3649.2	3.91/3.91
Cu²⁺	32.079	6.717	16.976	3658.0	4.02/4.03
Zn²⁺	32.061	6.726	17.004	3667.0	4.09/4.10
	(31.861)†	(6.601)	(16.895)	(3553.1)	-

* In the metal-substituted porphyrins, the reported d(N-N) corresponds to twice the cation-N distance. †Experimental data at room temperature for the taken from Section 8.5 of the supplementary information of Ref. [62].

B. Thermodynamics of metal substitutions from aqueous solution

To discuss the stability of the material with the different metal cation (M^{2+}) substitutions, we have calculated the enthalpies and free energies for the process of cation exchange with aqueous solution, according to the following reaction:

$$2H–MOF + M^{2+}_{(aq)} \leftrightarrow M–MOF + 2H^{+}_{(aq)} \qquad (5.1)$$
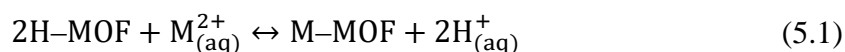
using a mixed theoretical-empirical approach for the treatment of the aqueous cations. For each cation, the enthalpy in aqueous solution is approximated using the following quantities: a) the DFT energy of the neutral atom in the gas phase, calculated with VASP at the experimental spin groundstate, using a large supercell and the same functional and

precision parameters as in the MOF calculations; b) the sum of the experimental first and second ionization energies,[219, 220] which is the energy needed to ionize the neutral atom to a M^{2+} cation (of course, only the first ionization energy is used in the case of hydrogen); and c) the experimental hydration enthalpy,[221] which is the enthalpy change in the process of moving the M^{2+} cation from the gas phase to aqueous solution. The addition of these three contributions gives the enthalpy of the aqueous cation, which will be used in the calculation of the enthalpy change of reaction (5.1), ΔH. On the other hand, the reaction free energy ΔG can be estimated as:

$$\Delta G = \Delta G_0 + k_{\mathrm{B}} T \ln \left(\frac{[\mathrm{H}^+]^2}{[\mathrm{M}^{2+}]} \right) \tag{5.2}$$

where ΔG_0 is calculated using the same procedure as for ΔH, but employing the experimental hydration free energies of the cation (instead of the hydration enthalpy), *i.e.*, considering the entropy contribution to hydration.[222] The second term, where k_{B} is Boltzmann's constant, takes into account the effect of the relative concentrations of the cations in aqueous solution. The obtained values for ΔH and ΔG_0 are reported in Table 5.2. As shown in Figure 5.2, the variation with cation concentration and pH is relatively weak. Increasing the solution pH (*i.e.* decreasing the proton concentration) or increasing the metal concentration in solution, makes the exchange reaction slightly more favourable.

The calculated free energies for reaction 5.1 are negative for all the cations at any reasonable concentration of the cations in aqueous solution and pH values, which indicates that immersing the 2H-MOF in an aqueous solution of M^{2+} cations would lead to spontaneous exchange with the cations from the solution substituting the protons at the centre of the porphyrin rings. The exchange process is partly driven by entropy effects. Indeed, the enthalpy change, ΔH, of the exchange process for Fe^{2+} is positive, and it is

the introduction of the hydration entropy effect through the hydration free energy what makes the exchange spontaneous. This analysis suggests that the substitution of these metals in the porphyrin-based MOF should be straightforward in experiment. This is agreement with the observed experimentally easy introduction of Cu^{2+} at porphyrin metal centres in Al-PMOF.[213] The preference for particular spin states, which can be seen from Table 5.2, will be discussed below in terms of the electronic structure.

Table 5.2. Enthalpy and free energy change of the process of exchanging the two protons at the centre of the porphyrin by a M^{2+} cation, for the various possible spin moments (μ). LS, low-spin. IS, intermediate-spin. HS, high-spin. Bold font is used to highlight the most stable spin state for each composition.

Cation	Spin State	μ (μ_B)	ΔH (eV)	ΔG_0 (eV)
Fe^{2+}	LS	0	0.61	-0.82
	IS	**2**	**0.20**	**-1.23**
	HS	4	0.91	-0.52
Co^{2+}	**LS**	**1**	**-2.16**	**-3.28**
	HS	3	-1.34	-2.46
Ni^{2+}	**LS**	**0**	**-3.05**	**-4.60**
	HS	2	-1.93	-3.48
Cu^{2+}	-	1	**-5.86**	**-6.86**
Zn^{2+}	-	0	**-4.52**	**-5.58**
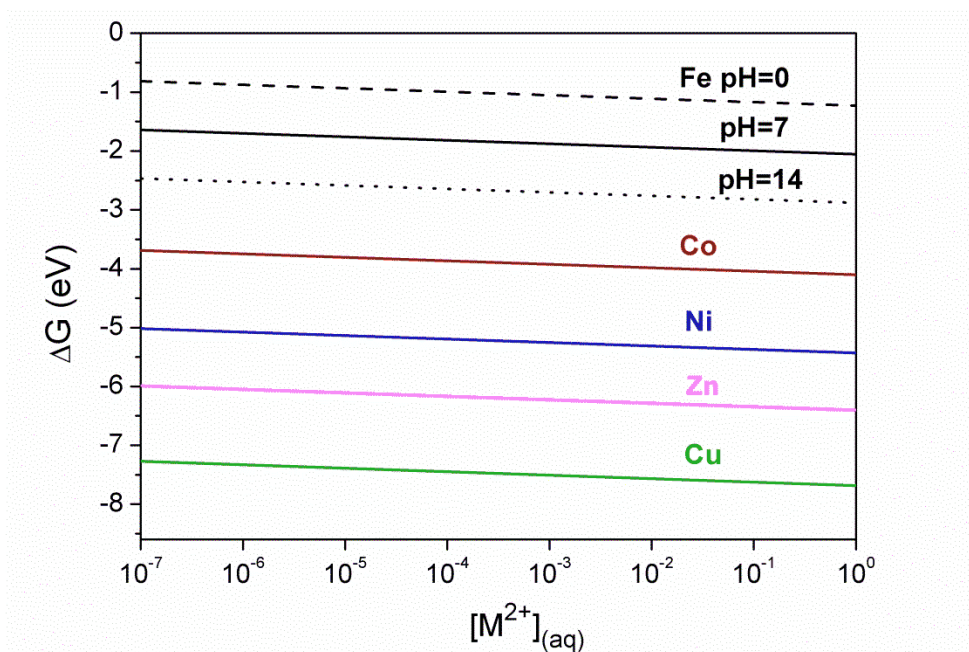
Figure 5.2. Free energy of the cation exchange reaction (as shown in Equation 5.1), as a function of type of cation, cation concentration in solution and pH (at room temperature). All solid lines correspond to values at pH=7. For Fe we also show the two lines corresponding to pH=0 and pH=14. For the other cations, the variation with pH is the same as in the case of Fe, so for clarity reasons only the results at neutral pH are shown.

C. Electronic structure

The total electronic density of states (DOS) and their projections on the $3d$ orbitals of the metals are shown in Figure 5.3. All structures are semiconductors, with bandgaps in the range between 2.0 and 2.6 eV. A bandgap of around 2 eV is generally considered to be ideal for single-semiconductor water splitting photocatalysis.[22] Anatase TiO_2, one of the most widely investigated photocatalysts for water splitting, has a bandgap of 3.2 eV,[223] which has to be engineered via doping in order to favour the absorption of the visible component of the solar spectrum.[224, 225] MOFs with adequate band alignment for photocatalysis were reported by Butler *et al.*,[82] although the calculated bandgaps were wider (above 3 eV in all cases).

Figure 5.3. Electronic density of states (DOS) of the protonated and metal-substituted porphyrin MOFs.

Porphyrin ligand field theory can be used to explain the metal $3d$ contributions to the DOS. Although the position of porphyrin as a ligand in the spectrochemical series is considered to be ambiguous, it is known that in metallo-porphyrins with square planar
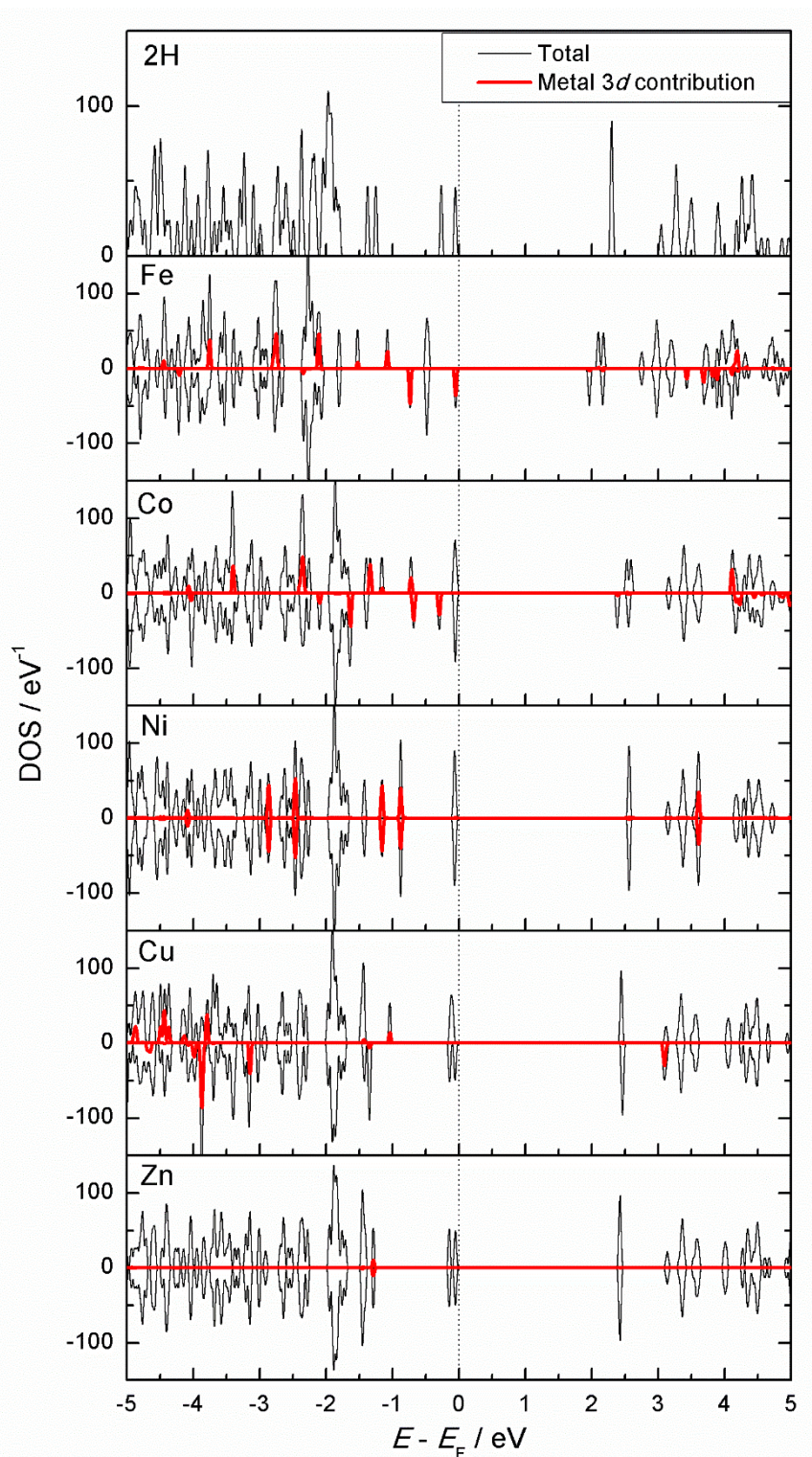
coordination of divalent cations, the porphyrin tends to act as a strong field ligand.[226] That

means that the $d_{x^2-y^2}$ level is very high up in energy compared with the others, as shown

schematically in Figure 5.4. But in this MOF, the degeneracy of the two lower d levels is

broken, because the crystal does not have the 4-fold rotation axis that would be present

in the isolated gas-phase porphyrin. The distortion could be then referred to as rectangular

distortion, to indicate the lowering of the symmetry to a 2-fold rotation axis.
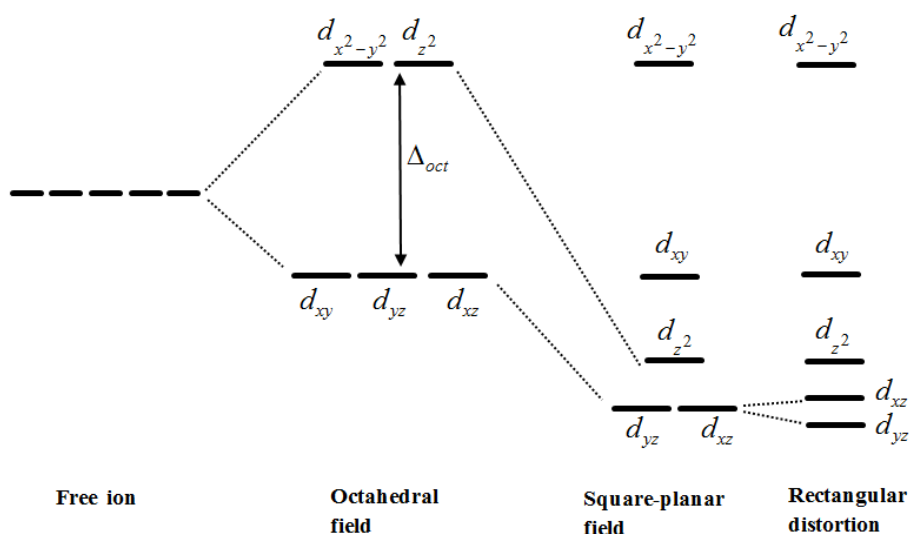
Figure 5.4. Scheme of the splitting of *d* orbitals in a square planar field, and the effect of a rectangular distortion.

Making use of the splitting of levels shown in Figure 5.4, the spin state of the MOF for

each cation can be explained:

a) Fe^{2+} (d^6). The most favourable configuration is an intermediate-spin state with

magnetic moment $\mu(=2S) = 2$ per Fe^{2+} cation. The high-spin state ($\mu=4$) is forbidden by

the strong splitting, since it would require the promotion of an electron to the high-lying

$d_{x^2-y^2}$ level. But the separation between the rest of the d levels is not strong enough to lead

to low-spin state. Following Hund's rule, the favourable state is therefore the

intermediate-spin one ($\mu=2$), with the d_{yz} and d_{xz} levels doubly occupied and d_{xy} and d_{z^2}

singly occupied. The intermediate-spin groundstate of Fe^{2+} in porphyrin is consistent with previous theoretical results for porphyrin molecules.[227]

b) Co^{2+} (d^7). This cation has one electron more than Fe^{2+}. For that reason, the d_{z^2} level is doubly occupied and the only unpaired electron is in the d_{xy} level, leading to a low-spin state ($\mu=1$).

c) Ni^{2+} (d^8). In this case the four low energy levels are doubly occupied in the low-spin state ($\mu=0$). The high-spin state ($\mu=2$) would require the promotion of one electron from the d_{xy} level to the $d_{x^2-y^2}$ level, making it energetically unfavourable.

d) Cu^{2+} (d^9). There is only one possible spin state for this cation ($\mu=1$), since the four low energy levels are filled and one electron occupies the $d_{x^2-y^2}$ level.

e) Zn^{2+} (d^{10}). In this case, the five d orbitals are filled, so $\mu=0$.

We can see in Figure 5.3 that all materials (except Fe-Al-PMOF) have similar values of bandgap, between 2.3 eV and 2.6 eV. This constant bandgap is determined by the frontier orbitals of the porphyrin. But Fe atoms introduce the d_{xy} levels into this otherwise unoccupied region (close to the valence band), leading to a decrease in bandgap to 2.02 eV. In this case the bandgaps of the materials clearly make them good candidates to carry out photocatalytic reactions, since they would be able to absorb most of the solar radiation. However, in order to assess the ability of a material to perform photocatalytic water splitting or carbon dioxide reduction, we also need to investigate if the semiconductors exhibit the correct alignment of the bands with respect to the half-reaction potentials, which we do in the following section.

D. Band edge positions with respect to electrode potentials

For a photocatalytic reaction to occur, the material needs to have the correct band gap, as well as the correct alignment of the bands with respect to the electrode potentials. Investigating this alignment requires knowledge of the absolute values of the electronic energy levels (*i.e.* with respect to vacuum). However, periodic DFT calculations provide only relative values with respect to an internal reference level, typically the average electron potential in the solid. To solve this problem, Butler *et al.*[82] suggested a method to estimate the vacuum level in porous structures, based on calculating the potential at different positions within the pores.

The alignment of the bands with the vacuum level allows us to explore the thermodynamic feasibility of the photocatalytic processes. A single-semiconductor photocatalyst requires certain important characteristics in its electronic structure. For example, for the water splitting reaction, the positions of the conduction and valence band edges should straddle the redox potentials for water photolysis,[21-23] *i.e.* the valence band edge should be below the energy of the oxygen evolution reaction (OER) Equation (1.3) and the conduction band edge should be above the energy corresponding to the hydrogen evolution reaction (HER) Equation (1.4).

The energy scale has the opposite sign of the potential scale, so lower energy means higher potential, and *vice versa*. The bandgap must be wider than 1.23 eV (difference between the HER and the OER levels). After loss mechanisms are accounted for, a minimum bandgap of 2 eV or more is generally necessary,[22] but the bandgap should not be too wide, in order to allow the adsorption of photons from the visible part of solar radiation. It is known that, in the vacuum scale and at pH=0, the HER level is located at -4.44 eV, and the OER level is located at -5.67 eV.[228] At temperature T and pH > 0, these energy levels are shifted up by pH×($k_B T × ln10$). By referencing the electronic levels with

respect to the vacuum level (taken here as the electron potential at the centre of the largest pore), the band edges of the semiconductor can be obtained to analyse whether they are in a favourable position to catalyse the solar splitting of water under a given set of conditions. In the case of carbon dioxide conversion to fuels (e.g. methane, CH_4, methanol, CH_3OH, or formic acid, HCO_2H), the position of the conduction band of the semiconductor photocatalyst has to be above the redox potential for the CO_2 reduction half-reaction, which depends on the specific fuel produced. Since the CO_2/CH_4, CO_2/CH_3OH and CO_2/HCO_2H levels are above the HER (H^+/H_2) level, the photocatalyst for the CO_2 reduction reactions requires a minimum bandgap that is wider than for water splitting.

Figure 5.5 shows the bandgaps and band edge positions of the six material compositions studied in this work, with respect to the vacuum level, as calculated using the HSE06 functional. The values of the redox potentials (at neutral pH and room temperature) for the species appearing in the water splitting reaction and for the reactions in which carbon dioxide is reduced to produce methane, methanol, and formic acid, are also shown in the figure: $E(H_2O/O_2)$=-5.26 eV; $E(H^+/H_2)$=-4.03 eV; $E(CO_2/CH_4)$=-3.79 eV; $E(CO_2/CH_3OH)$=-3.65 eV; $E(CO_2/HCOOH)$=-3.42 eV.[229]
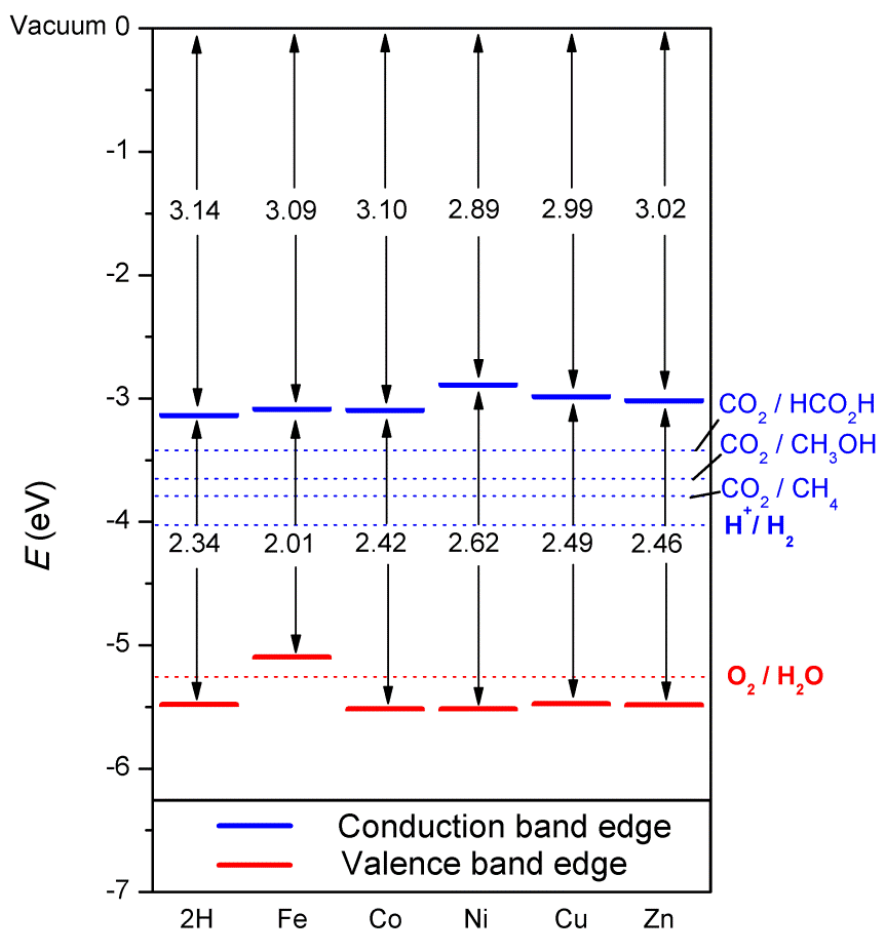
Figure 5.5. Bandgaps and band edge positions with respect to the vacuum level, as calculated with the HSE06 functional. Energy levels corresponding to redox potentials of water splitting and carbon dioxide reduction reactions producing methane, methanol, and formic acid at pH = 7 are also shown with dotted lines.

For all materials, the conduction band edge is at roughly the same position (ca. -3 eV in the vacuum scale), which is above the energies corresponding to the H^+/H_2 and CO_2/CH_xO_y levels. That means that the MOF would be thermodynamically able to donate an excited electron from the conduction band for the reduction half-reactions to proceed. The conduction bands are slightly higher than desired for water splitting, but they are in a nearly ideal position for the carbon dioxide reduction reactions.

As for the oxygen evolution half-reaction, in all materials, except Fe-Al-PMOF, the valence band edge lies at about -5.5 eV in the vacuum scale, below the energy of the

O_2/H_2O level. In the case of Fe-Al-PMOF, it lies slightly (~0.2 eV) above. Of course, due to the approximations made in our calculations, such small energy differences are not reliable. But it is clear that the valence band edge for all compositions is in the correct energy range in the absolute scale. Small deviations from the ideal band edge positions in a semiconductor with the adequate bandgap can always be corrected via the application of a weak bias voltage in a photoelectrochemical device, shifting both band edges with respect to the redox levels (applying a voltage increases device complexity and also consumes energy, so a large bias voltage should be avoided). For example, in a recent first-principles screening of materials for water splitting photocatalysts, Wu *et al.* set the threshold of the allowed bias voltage to 0.7 V.[230] Our present calculations show that the Al-PMOF, in all the different compositions explored here, would be able to operate as single-semiconductor photocatalyst with little or no bias voltage applied at neutral pH.

5.3.2 Substitutions at the octahedral metal centre

A. Crystal structure and relative stabilities

When considering substitutions at the octahedral metal centre two different metal cations were considered at the octahedral sites (A^{3+} = Al^{3+} or Fe^{3+}) or a mixture of the two as well as considering both Zn^{2+} and Fe^{2+} as the porphyrin metal centre. In these calculations vdW corrections were also included and the main geometric properties of the structures are shown in Table 5.3. Including the vdW correction led to a smaller change in the cell volume (0.5-0.8%) compared to when no vdW correction was applied. This reduced the difference between computational and experimental values from 3.2 to 2.5%. However, the results in terms of the final electronic structure are not significantly affected by the introduction of vdW corrections in this optimisation step. The cell parameters are noticeably affected by the nature of the cation in the octahedral centre (A^{3+}): the structures with Fe^{3+} in the octahedral site have ~5% higher cell volume than the structure with Al^{3+} in the octahedral site. This is in quantitative agreement with the relative values of the cell volumes found experimentally for (Al^{3+}, Zn^{2+})PMOF and (Fe^{3+}, Fe^{2+})PMOF.[62, 63] (Note that the latter experimental structure is not strictly equivalent to the one modelled in this work, because it has pyrazine ligands connecting the porphyrins in the direction perpendicular to the porphyrin planes; the presence of these ancillary ligands can be expected to have little influence on the crystal cell parameters). But the cell parameters are not significantly affected (less than 0.5%) by the nature of the porphyrin metal centre (M^{2+}), which can be expected from the fact that the M-N bond distances at the porphyrin centres are much less variable, due to surrounding rigid structure of the porphyrin, than the A-O distances at the octahedral centres. The AO_6 octahedra exhibit D4h distortions, with two A-O distances (apical) of slightly shorter length than that of the equatorial A-O

distances. The magnitude of the D4h distortion, as given by the ratio between the apical

and equatorial distances, is not affected by the nature of the metal centre (Al or Fe).

Table 5.3. Calculated lattice parameters, cell volume and the two perpendicular N-N distances inside the porphyrin. All structures adopt the orthorhombic space group *Cmmm* (65), where α=β=γ=90⁰. Available experimental values at room temperature are given in parenthesis.

Porphyrin Centre (M^{2+})	Octahedral Centre (A^{3+})	a (Å)	b (Å)	c (Å)	V (Å³)	d [M-N] (Å)†	Apical d [A-O] (Å)	Equat d [A-O] (Å)
Zn^{2+}	Al^{3+}	32.079 (31.861)*	6.687 (6.601)	16.977 (16.895)	3641.5 (3553.1)	2.04	1.86	1.93
Zn^{2+}	Fe^{3+}	32.297	6.927	17.156	3837.9	2.04	1.96	2.04
Fe^{2+}	Al^{3+}	32.020	6.687	16.958	3631.1	2.00	1.86	1.93
Fe^{2+}	Fe^{3+}	32.249 (32.355)**	6.932 (6.835)	17.138 (16.896)	3830.9 (3736.5)	2.00	1.96	2.04

† Average over 4 bonds in the square-planar coordination. *Experimental cell parameters for the (Zn^{2+}, Al^{3+})-PMOF are taken from Section 8.5 of the supplementary information of Ref. [62] **Experimental cell parameters for the (Fe^{2+}, Fe^{3+})-PMOF are taken from those of structure 4B in the supplementary information of Ref. [63] (not identical to the one modelled here due to the presence of ancillary pyrazine ligands in the experimental structure).

The relative thermodynamic stabilities of these crystal structures can be discussed in terms of their total energies in comparison with reference phases, for example, the A_2O_3 oxide phases. Since both Al_2O_3 and Fe_2O_3 with corundum structure are stable phases where the metal cations are octahedrally coordinated to oxygen as in the PMOF, the hypothetical cation exchange reaction is considered:

$$(Al^{3+}, M^{2+})PMOF + Fe_2O_3 \rightarrow (Fe^{3+}, M^{2+})PMOF + Al_2O_3 \qquad (5.3)$$
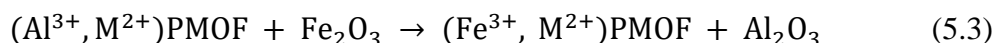
which corresponds to reaction energies of 0.35 eV per metal A atom when Zn is at the porphyrin centre, and 0.14 eV when Fe is at the porphyrin centre. The difference between the two values, is interesting, as it suggests that the substitution of Fe in octahedral position is easier if Fe is also present in the porphyrin centre. The experimental synthesis of this structure using $FeCl_3$ indeed leads to Fe occupying both the octahedral and the porphyrin centres.[63]

B. Electronic structure

In the previous Section (5.3.1C) the electronic structure of the "parent" compound $(Al^{3+}, Zn^{2+})PMOF$ and of the compound with Fe substituted in the porphyrin metal centres was described (Al^{3+}, Fe^{2+}). These calculations were repeated with the vdW correction in order to establish a comparison with the new materials considered in this study. The electronic density of states of $(Al^{3+}, Zn^{2+})PMOF$ (Figure 5.6a) showed a band gap of ~2.5 eV. This is consistent with the previous calculations suggestion the geometrical structure has little effect on the electronic properties of these materials. Similar values are also calculated for the $(Al^{3+}, Fe^{2+})PMOF$.
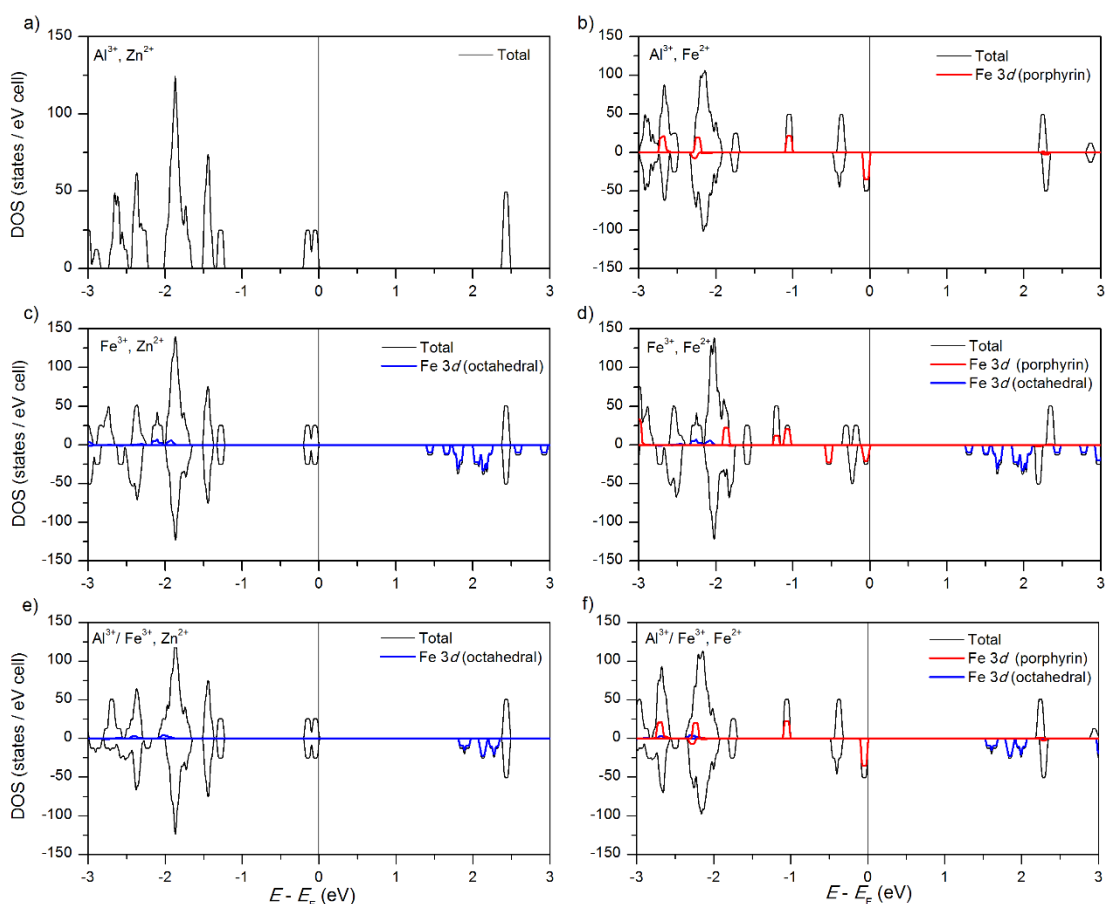
Figure 5.6. Electronic density of states, as obtained with the screened hybrid functional HSE06, for (a) the "parent" structure (Al^{3+}, Zn^{2+})PMOF; (b) for the structure with Fe in the porphyrin metal centres, (Al^{3+}, Fe^{2+})PMOF; (c) for the structure with Fe in the octahedral metal centres, (Fe^{3+}, Zn^{2+})PMOF; (d) for the structure with Fe both in the porphyrin and the octahedral metal centres, (Fe^{3+}, Fe^{2+})PMOF; (e) for the structure with a mixture of Al and Fe at the octahedral centres, (Al^{3+}/Fe^{3+}, Zn^{2+})PMOF, and (f) for the structure with a mixture of Al and Fe at the octahedral centres, and Fe in porphyrin metal centres, (Al^{3+}/Fe^{3+}, Fe^{2+})PMOF. Positive and negative DOS correspond to a and b spin components, respectively.

Both the valence and conduction band edges in (Al^{3+}, Zn^{2+})PMOF are contributed by the porphyrin, the occupied $3d$ orbitals of Zn lie far below the Fermi level. The substitution of Fe at the porphyrin centres, forming (Al^{3+}, Fe^{2+})PMOF, reduces the band gap by ~0.2 eV, which is due to the appearance of a β-spin Fe $3d$ level just above the occupied porphyrin levels (Figure 5.6b). The most stable spin state was found to be the intermediate spin consistent with the previous results.

As shown in Figure 5.6c, substituting the Al^{3+} cation by Fe^{3+} in the octahedral metal centre (forming (Fe^{3+}, Zn^{2+})PMOF) does have a much stronger effect on the bandgap, which is now reduced to 1.5 eV. In the (D4h-distorted) octahedral FeO_6 coordination, Fe^{3+} adopts a high-spin state ($\mu=5$) where all the α-spin levels are occupied and all the β-spin levels are empty. The lowest-lying β-spin levels fall below the porphyrin lowest-unoccupied orbitals, thus narrowing the band gap with respect to the PMOFs with Al^{3+} in the octahedral centre. The observation that the conduction band edge is now contributed by levels from a reducible metal species ($Fe^{3+} \rightarrow Fe^{2+}$) is important from the point of view of potential photocatalytic applications, because it makes easier the creation of an excited state with electron – hole separation, via the promotion of an electron from the porphyrin ligand to the metal node. This ligand-to-metal charge transfer (LMCT) is an essential element for the realisation of photocatalysis in MOFs.[231, 232]

Finally, the simultaneous substitution of Fe into both the porphyrin and the octahedral metal centres, forming (Fe^{3+}, Fe^{2+})PMOF as in the experimental work by Fateeva et al.,[63] leads to a reduced band gap of 1.3 eV. Figure 5.6d shows that this effect results from a combination of the two effects described above: Fe^{2+} in the porphyrin centre raises the valence band edge by introducing an occupied $3d$ level, while Fe^{3+} in the conduction band lowers the conduction band edge by introducing an empty $3d$ level. This effect can also be seen in the band structure performed at the PBE+U level of theory (Figure 5.7) a similar DOS can be seen for the PMOFs although in each case the band gap is smaller by about 0.5-0.6 eV. However, the trend is consistent and in the (Al^{3+}, Fe^{2+})PMOF it is clear that the reduction in the band gap is again due to the β-spin Fe $3d$ level just above the occupied porphyrin levels consistent with the HSE06 results

While Fe substitution seems like a promising approach to engineer the electronic band structure of PMOFs for photocatalytic applications, the absolute positions of the

band edges need to be determined in order to see if they are favourable for the photocatalytic reactions of interest.
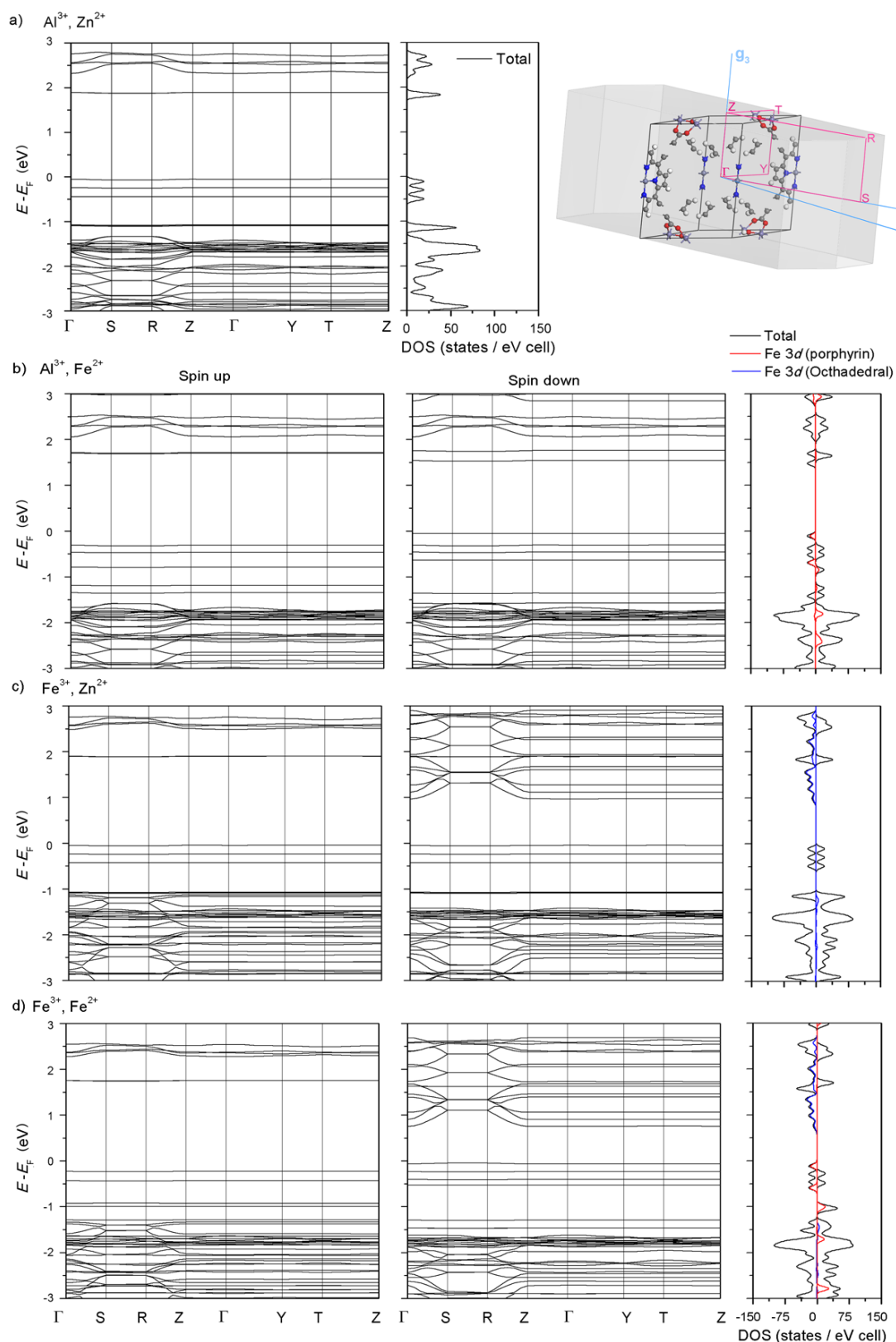
Figure 5.7. Electronic band structures and density of states (DOS) calculated using the PBE+U method for a) the "parent" structure (Al³⁺, Zn²⁺)PMOF; b) for the structure with Fe in the porphyrin metal centres, (Al³⁺, Fe²⁺)PMOF; c) for the structure with Fe in the octahedral metal centres, (Fe³⁺, Zn²⁺)PMOF; and d) for the structure with Fe both in the porphyrin and the octahedral metal centres, (Fe³⁺, Fe²⁺)PMOF.

C. Estimation of the vacuum potential

The vacuum potential was again calculated using the method proposed by Butler *et al.*[82] and the potential at different positions along the pores was calculated. The vacuum potential was calculated by choosing the zero-gradient point that was farthest apart from the framework atoms.
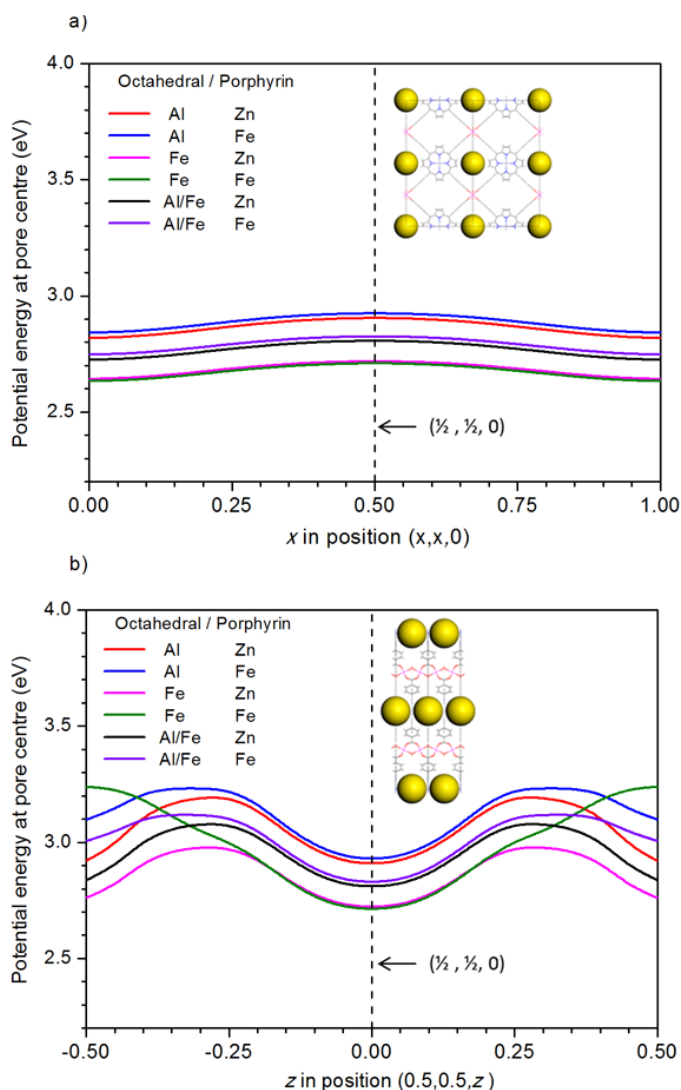
Figure 5.8. Electrostatic potential energy at the pore centre, as calculated with HSE06 functional along a) pores perpendicular to the porphyrin planes (coordinates (x,x,0) in the primitive cell), and b) pores parallel to the porphyrin plane (coordinates (0.5,0.5,z) in the primitive cell). The vertical dashed line in both figures corresponds to (0.5, 0.5, 0), which is the point farthest apart from all atoms in the structure and is used to estimate the vacuum potential in this work. It is represented as large yellow spheres within the PMOF structures in the inset figures (shown in the conventional cell for clearer visualisation).

The PMOF structure in this study has large pores perpendicular to the porphyrin planes, which in the primitive cell have centres with coordinates $(x,x,0)$. These pores intersect other pores, parallel to the porphyrin planes, which have centres with coordinates $(0.5, 0.5, z)$. The calculated electrostatic potential energies along these pore centres are shown in Figure 5.8. It is clear that the intersection point $(0.5, 0.5, 0)$ between the two sets of pores is a zero-gradient point which is a good candidate to represent the vacuum region.

A further check measuring the distance between this point and the closest framework atoms gave ~6.2 Å. In contrast, other candidate points, like $(0.5,0.5,0.5)$ (where the symmetrically equivalent pores along $(x,0.5,0.5)$ and $(0.5, y,0.5)$ intersect), are closer to atoms in the structure (5.2 Å). The point $(0.5,0.5,0)$ of the primitive cell (which corresponds to positions $(0,0.5,0)$ or $(0.5,0,0)$ in the conventional cell) was taken as the "vacuum" reference level (Table 5.**4**), and this value was subtracted from the calculated energy levels to put them in an (approximately) absolute scale. This is again consistent with the point used in the analysis of substitution in the porphyrin metal centre (section 5.3.1)

Table 5.4**. Potential energies at the vacuum (with respect to average potential in crystal).**

Octahedral centre	Porphyrin centre	Potential energy at pore centre (eV)
Al	Zn	2.90
Al	Fe	2.92
Fe	Zn	2.72
Fe	Fe	2.71
Al/Fe	Zn	2.71
Al/Fe	Fe	2.81

D. Band alignment with respect to electrode potentials

With the bands aligned to that of the vacuum level, it is possible to analyse the suitability of the band positions for the photocatalysis of solar fuel synthesis from H_2O or CO_2. These positions are shown in Figure 5.9. The positions, in the vacuum scale, of the energy levels corresponding to the oxidation and reduction reactions involved in water splitting and in carbon dioxide reduction to produce methane and methanol, at pH = 7 (potentials at finite pH are shifted from the values at pH = 0, by $2.30 \times pH \times k_B T$).
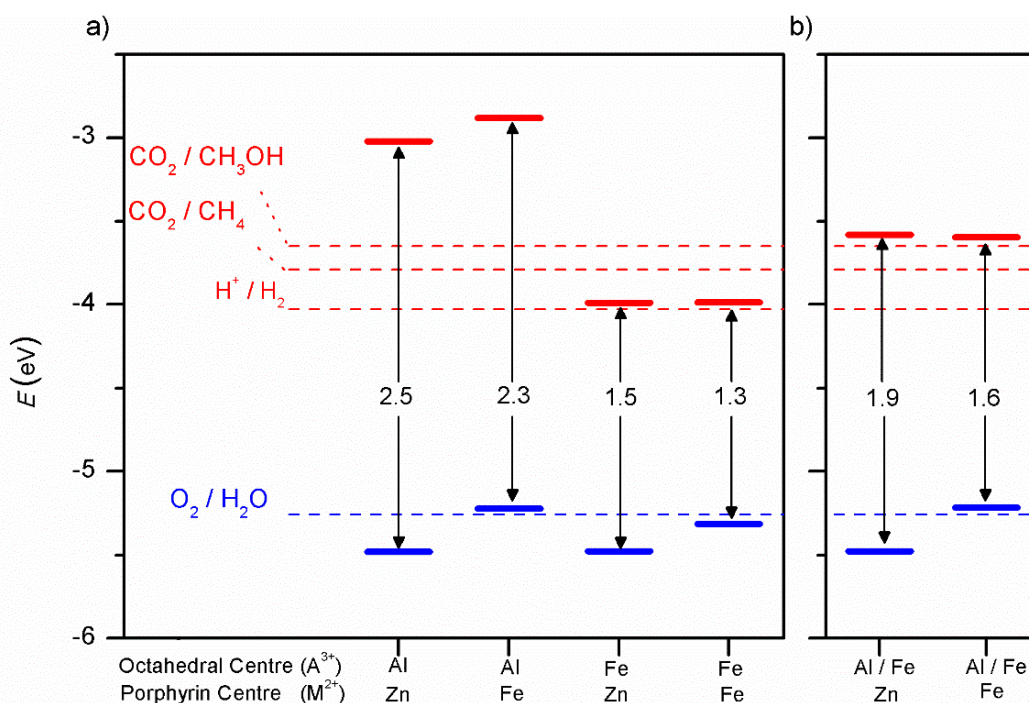
Figure 5.9. Band gaps and band edge positions with respect to the vacuum level, as calculated with the screened hybrid functional HSE06. The energy levels corresponding to redox potentials of water splitting and carbon dioxide reduction reactions producing methane and methanol at pH = 7 are also shown with dotted lines.

The parent material (Al^{3+}, Zn^{2+})PMOF can in principle catalyse both types of reactions (water splitting and carbon dioxide reduction), since the valence band edge is below the OER level and the conduction band edge is above the levels for the different reduction reactions. However, the conduction band edge is a bit too high for the water splitting reaction, for which the optimum band gap is around 2 eV (*i.e.* it is the minimum

gap that could be used, taking into account the need for additional potential beyond the 1.23 eV per electron required to drive the oxidation and reduction reactions).[22]

Substituting Zn by Fe in the porphyrin centres lowers the band gap, as discussed above, but unfortunately it does so by raising the absolute position of the valence band edge, which is not desirable because it pushes that edge above the OER level. On the other hand, substituting Al by Fe in the octahedral centres lowers the conduction band edge, but in this case by a bit too much, resulting in band gaps (1.5 eV for $(Fe^{3+},$ $Zn^{2+})PMOF$ and 1.3 eV for $(Fe^{3+}, Fe^{2+})PMOF$) that are too narrow to simultaneously drive the oxidation and reduction reactions in water splitting.

While the absolute band edge positions reported here are only approximate due to the simple methods involved, it is clear that the band edges are in the desired energy range in the absolute scale. In fact, deviations from the ideal band edge positions in a semiconductor can be corrected via the application of a weak bias voltage, which shifts both band edges with respect to the redox levels, as long as such deviations are small. But the band gaps reported in the materials discussed so far in this work are either a bit too wide or too narrow for water splitting photocatalysis.

E. Properties of mixed PMOF with both Al and Fe in octahedral centres

With the aim of finding a material with a band gap closer to the optimal value for water splitting, mixed systems have been considered (50% Al^{3+}, 50% Fe^{3+}) each occupying one of the two octahedral metal centres were Zn^{2+} or Fe^{2+} were considered in the porphyrin metal centre. In standard semiconductors, the band gap of mixed compounds varies continuously, although generally not linearly, between the pure end-members.[233, 234] Therefore, any band gap in between that of the pure systems can be obtained by choosing the appropriate composition, as long as the mixed composition is

thermodynamically stable. The concept has recently been realized in some organic semiconductors, despite the stronger localization of their electronic states.[235] It is therefore interesting to see whether we can obtain an intermediate value of the band gap from mixing the wide-gap and narrow-gap materials.

The high computational cost of screened hybrid functional calculations means that calculations were restricted to small simulation cells. The simplest ordered mixed structure can be created by substituting one of the two Al atoms in the primitive cell to form $(Al^{3+}/Fe^{3+},M^{2+})$PMOF. Since the two octahedral sites are equivalent, there is only one symmetrically independent configuration of Al and Fe distribution in the primitive cell. To investigate other possible configurations the larger conventional orthorhombic cell containing four octahedral sites must be used. In this case there are six ways of distributing two Fe and two Al atoms over these sites, but only three configurations, which are shown in Figure 5.10, are found to be symmetrically independent (using the SOD program).[101] In configurations 1 and 2, Fe and Al alternate along the b direction (perpendicular to the porphyrin planes), within the one-dimensional chains of corner-sharing octahedra. In contrast, configuration 3 contains one Al-only chain and one Fe-only chain. Configuration 1 has the lowest energy, but the energy of configuration 2 is very close ($E_2 - E_1 = 20$ meV), whereas the energy of configuration 3 is somewhat higher ($E_3 - E_1 = 80$ meV), These results indicate that the main factor controlling the stability of the configurations is the distribution of Fe/Al along the one-dimensional chains of corner-sharing octahedra. Since the energy differences are small, it cannot be assumed that the system will exhibit the long-range order of configuration 1. Instead, there will be an equilibrium distribution of cations, with some tendency to Fe/Al alternation in the b direction. To obtain the probability distribution between the two configurations their DFT energies were mapped into a one-dimensional Ising model. At room temperature, the

equilibrium probability of Fe–Al pairs in nearest-neighbour positions at room temperature was determined to be $p = 73\%$. Therefore, configurations 1 and 2 (where $p = 100\%$) are better representations of the cation distribution than configuration 3 (where $p = 0$). This provides justification for the use of configuration 1 for the electronic structure and band alignment calculations of the mixed systems. It also has the added advantage over configuration 2 as it can be represented within the primitive cell (test calculations show that very similar results are obtained using configuration 2) saving computational costs. It is also reassuring that a formation energy of less than 1 kJ per mol of octahedral metal atom is obtained for the mixed system from the corresponding amounts of the pure compounds. This suggests that mixed structures should be stable towards phase separation (they would be stabilized with respect to the pure compounds by the configurational entropy). A more sophisticated and accurate treatment of the cation distribution would require larger supercells, but that becomes too computationally expensive at HSE06 level. Representing the mixed system using alternating Fe/Al ions along the chains of corner-sharing octahedra, even if not a perfect solution, is a good first approximation to explore the potential for compositional band gap engineering in PMOFs.
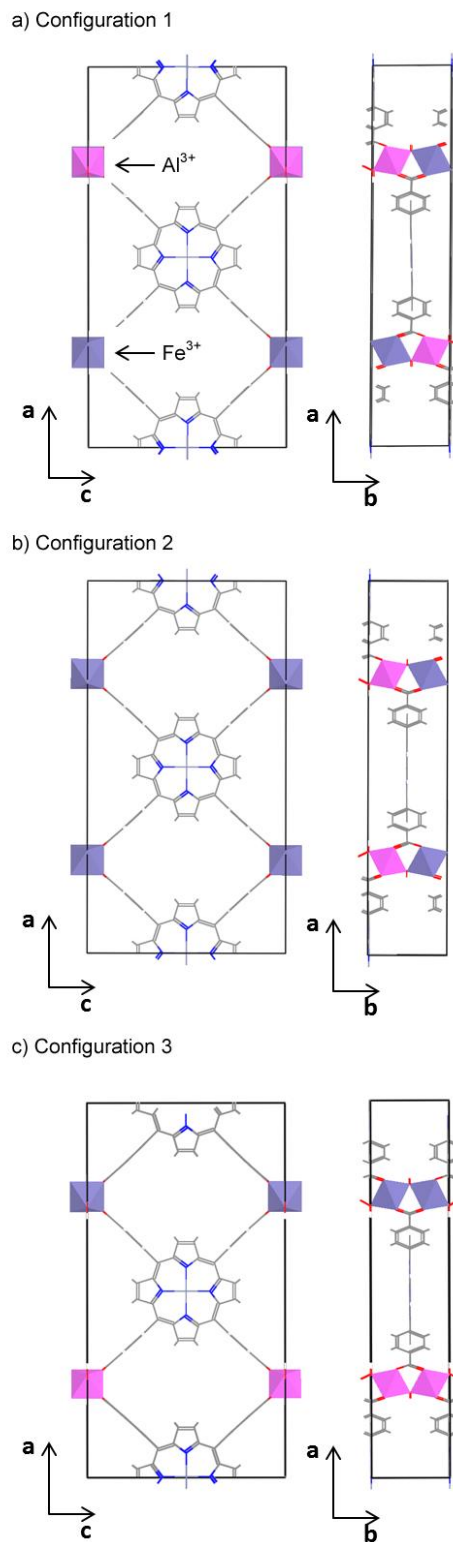
a) Configuration 1

b) Configuration 2

c) Configuration 3

Figure 5.10. The three symmetrically independent configurations of Fe and Al on the octahedral sites of the PMOF conventional (orthorhombic) cell.

Figure 5.9b shows that, indeed, the obtained band gap (1.9 eV) for $(Al^{3+}/Fe^{3+}, Zn^{2+})$PMOF is intermediate between that of (Al^{3+}, Zn^{2+})PMOF (2.5 eV) and that of (Fe^{3+}, Zn^{2+})PMOF (1.5 eV). The fact that it is not exactly the average of the values for the two endmembers, but a bit below, indicates a convex "bowing" of the band gap *vs.* composition curve, which is also common for standard semiconductor alloys.[233, 234] Comparing Figure 5.6e with Figure 5.6c we see that in the mixed compound the Fe $3d$ contributions to the DOS are more localized, and closer to the porphyrin lowest-unoccupied levels, than in the pure Fe compound, leading to a widening of the gap.

Figure 5.6e shows the result for the $(Al^{3+}/Fe^{3+}, Fe^{2+})$PMOF. In this case, as expected from our previous analysis, the valence band edge is contributed by filled Fe $3d$ levels from Fe^{2+} in the porphyrin, while the conduction band has moved to the same intermediate position as in $(Al^{3+}/Fe^{3+}, Zn^{2+})$PMOF. The alignment of the band edges with the redox potentials for photocatalysis is shown in Figure 5.9b. In the case of the $(Al^{3+}/Fe^{3+}, Zn^{2+})$PMOF, the band edges are in almost ideal position for water splitting, while the bandgap is perfect for absorption of visible light, which is a very encouraging result. In the $(Al^{3+}/Fe^{3+}, Fe^{2+})$PMOF system the valence band edge is a bit too high in relation with the O_2/H_2O redox potential. These results suggest that in order to create an intrinsic PMOF photocatalyst, it might be necessary to limit the Fe doping to the octahedral site, while preventing the Fe doping of the porphyrin site. Although experimentally Fe doping of the PMOF structure has been done at both sites simultaneously,[63] it is not anticipated that selective doping of the octahedral site would be too difficult an experimental challenge: several studies have demonstrated the viability of post-synthetic modification of the metal at the porphyrin centre in porphyrin-based MOFs.[236-238]

The alignment of the band edges with the redox potentials for photocatalysis is shown in Figure 5.9b. The mixed Al^{3+}/Fe^{3+}, Zn^{2+})PMOF composition exhibits the ideal band structure and alignment required for water splitting photocatalysis, while the bandgap is perfect for absorption of visible light. Furthermore, the nature of its valence and conduction band edges are also consistent with the ligand to-metal charge transfer (LMCT): photons would be absorbed by the porphyrin unit, and an electron would be excited to the reducible Fe^{3+} centres, allowing for electron–hole separation and potentially long recombination times. At the same time, the porous structure allows diffusion and access of the reactant molecules to the different sites, decreasing the need for high charge mobility towards the external surface, as expected for standard semiconductors. It is clear that this system shows promise as potential photocatalyst for water splitting and merits further investigation.

5.4 Conclusions

A thorough theoretical study of the electronic properties of porphyrin-based metal organic frameworks has been carried out, including both protonated, metallated (Fe^{2+}, Co^{2+}, Ni^{2+}, Cu^{2+}, Zn^{2+}) porphyrins and substitutions at the octahedral metal centres. Including the vdW correction led to a smaller change in the cell volume (0.5-0.8%) compared to when no vdW correction was applied. This was in better agreement with experiment, but had no significant on the electronic properties obtained.

With respect to the porphyrin metal centre when the materials are submerged in aqueous solution the protons would be spontaneously exchanged with the cations. The analysis of the electronic bands reveals that the bandgaps of all materials are in the favourable range for efficient adsorption of solar light (2.0 to 2.6 eV). The alignment of the bands is also favourable in all cases for the photocatalysis of water splitting and carbon dioxide reduction, which means that a device using these materials would require little or no bias voltage to function although may be a little high for efficient water-splitting. Although a band gap of 2.6 eV may be slightly too wide to take advantage of visible-light solar radiation.

Calculations also show small variations in the electronic band edges of the metal-substituted structures. The substitution of other late $3d$ transition metals (Co, Ni or Cu) at the porphyrin metal centre does not change the bandgap of the corresponding PMOFs to any significant extent, because their corresponding $3d$ levels fall below the highest occupied porphyrin levels.[215] The only exception is the Fe-substituted one, where an occupied d_{xy} state is introduced in the gap region above the valence band. The choice of metal at the porphyrin centre could be used to finely optimise other properties, e.g. molecular adsorption, affecting the photocatalytic process.

With respect to the octahedral metal centre, Fe substitutions have a more profound effect on the electronic properties of porphyrin-based metal organic frameworks. While Fe at the porphyrin metal centre has the effect of raising slightly the position of the valence band edge. Fe at the octahedral metal centre has the ability to lower significantly the position of the conduction band edge. This is due to the introduction of empty Fe $3d$ levels below the lowest unoccupied porphyrin levels. Fe is therefore an ideal dopant to engineer the band structure of these MOFs.

For their potential applications in photocatalysis of water splitting, the original structure with Al in the octahedral sites and Zn in the porphyrin centres has a band gap that is slightly too wide to take advantage of visible-light solar radiation, and not enough spatial separation of the highest-occupied and lowest unoccupied crystal orbitals. On the other hand, the structure with Fe in the octahedral sites has bandgaps that are too narrow for water splitting photocatalysis, and in particular a too low conduction band edge to be able to drive the reduction reactions. By partial substitution of Al with Fe at the octahedral sites, while keeping Zn at the porphyrin centres a very promising approach to improving the electronic structure has been demonstrated. Such structures seem to be stable with respect to decomposition into the pure phases, have a nearly ideal bandgap (1.9 eV) and correct band edge positions for water splitting photocatalysis, and have well-separated electron and hole localization regions, which could promote longer exciton recombination times. This study shows with some careful composition engineering, porphyrin-based MOFs could exhibit intrinsic photocatalytic activity in solar fuel synthesis reactions.

6   Zeolitic imidazolate frameworks (ZIFs)

This chapter focuses on another type of MOF, known as Zeolitic imidazolate frameworks (ZIFs). The methodology is similar to the previous chapter where the bands gaps and band edges of the MOFs were calculated to assess their functionality as photocatalysts. In this Chapter the periodic DFT calculations and band alignment of the ZIF structures were performed by myself. The electronic structures of the linkers in molecular form (with an attached proton) were calculated using Gaussian-09[239] and performed by a fellow project student in Grau-Crespo's group (Angus W. Collins) and by a collaborator in Seville (Prof. Norge Cruz-Hernández). The initial creation and structural optimisation of the hypothetical ZIF structures was performed by Dr A. Rabdel Ruiz-Salvador and Dr S. Hamad in Seville. The electronic structures of the linkers were calculated using the same HSE06 functional at PBE-optimized geometries.

6.1   Introduction

ZIFs offer an alternative to the porphyrin based MOFs discussed in chapter 5 for photocatalytic water-splitting. They are in fact a sub-family of MOFs which consist of a tetrahedrally-coordinated transition metal ion, such as Zn, Co or Cu connected by imidazolate linkers. This is similar to aluminosilicate zeolites (Figure 6.1), but in this case the transition metal takes the role of the silicon atom and the imidazolate linker takes the role of the oxygen linker. The metal-imidazolate-metal angle is about the same as the 145° angle found in the Si-O-Si bond in zeolites. The result is that ZIFs form similar topologies to those found in zeolites through self-assembly[240, 241]
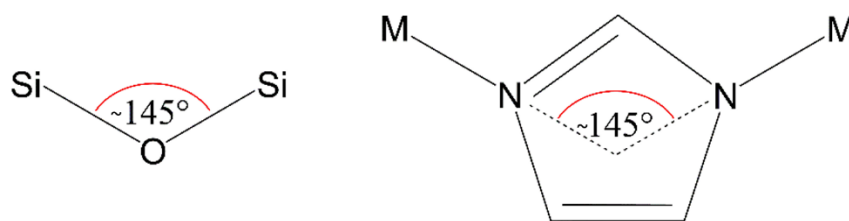
Figure 6.1. Similar geometrical angles of ~145° are found in the Si-O-Si bond in zeolites, and the metal-imidazolate-metal angle in ZIFs

Mixed ZIFs can also be engineered by mixing a wide range of different imidazole-based linkers within the same structure. Controlling the band gap and band alignment of ZIFs using a linker mix and match approach is an interesting method in optimizing the photocatalytic properties of ZIFs. ZIFs have also been shown to exhibit the required high chemical and thermal stability in aqueous solution.[240-242] While the most common ZIFs are those with a Zn transition metal ion, ZIFs containing Cu and Co are also reported experimentally.[241] This leads to a variety of different possibilities for the investigation of their photocatalytic properties; using imidazolate-based linkers, mixing linkers or changing the transition metal ion. In this work 12 linkers are selected, with the bare imidazolate linker being represented as Im. The full list of linkers are shown in Figure 6.2.
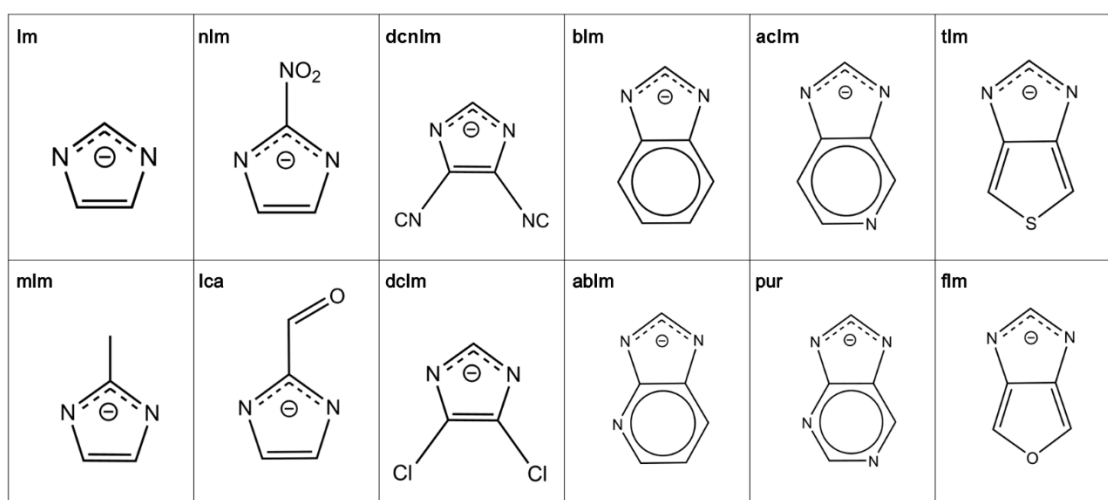
Figure 6.2. Imidazole-based linkers investigated for their photocatalytic properties in ZIFs.

The nomenclature in this work follows that reported by Phan *et al.*[241] The following functionalization's are made to the Im linker: added nitro (nIm), carboxaldehyde (Ica), or methyl (mIm) side chains at ring position 2; di-cyanide (dcnIm) or di-chlorine (dcIm) at positions 4,5; fused benzene (bIm), pyridine (abIm, acIm) or purine (pur) 6-membered rings; and fused thiophene (tIm) or furan (fIm) 5-membered rings (Figure 6.2). ZIF structures with some of these linkers have been reported before, including $Cu(Im)_2$, $Zn(Ica)_2$, $Zn(bIm)_2$, $Zn(mIm)_2$ and $Co(nIm)_2$ with sodalite (**sod**) topology, as well as $Zn(abIm)_2$ and $Zn(pur)_2$ with Linde Type A (LTA) topology.[241] So far, no ZIFs have been synthesized with tIm and fIm linkers, although these molecular units are reported in the patent literature.[243]

ZIF structures can be found in a variety of topologies but this work focuses on the **sod** topology which has several reported structures in the literature.[241, 242] The **sod** topology (Figure 6.3a) was chosen because of its flexibility to accept a wide range of chemical compositions, in terms of both linkers and metals.[241] Recently, ZIFs with **sod** topologies have been experimentally investigated and shown promise in the context of photocatalytic applications.[244, 245] Also, its primitive cell, containing 6 ZnX_2 formula units, where X stands for the imidazolate-based linker (Figure 6.3b) is small enough to allow an efficient screening of a range of compositions using quantum-mechanical calculations.
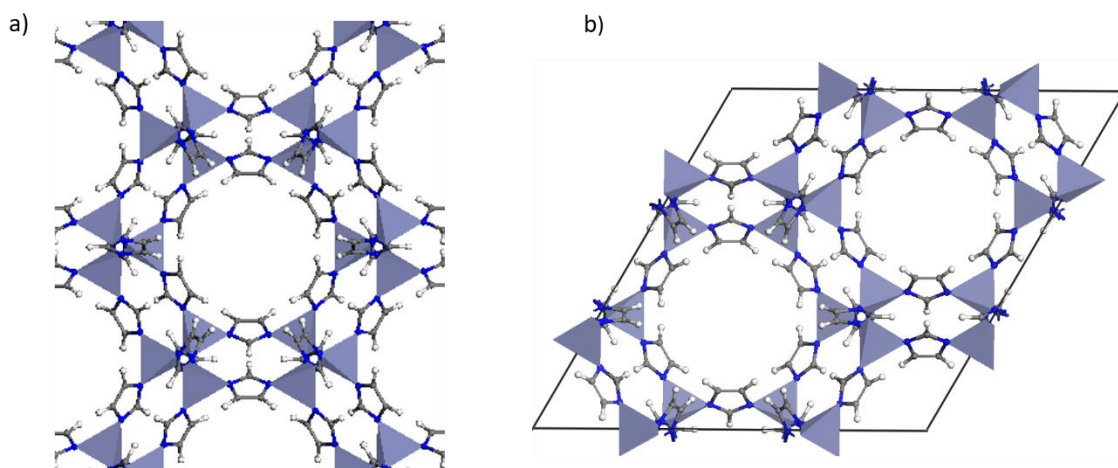
Figure 6.3. ZIF with composition ZnIm$_2$ (Im represents the bare imidazolate linker) and sodalite topology, a) seen along the direction of the largest pore and b) in its primitive rhombohedral arrangement. The tetrahedra are centered on Zn atoms; blue, grey and white balls represent N, C and H atoms respectively.

6.2   Computational details

The DFT calculations of the periodic structures were performed using VASP.[120] A cutoff of 520 eV was used for the plane wave expansion. Considering the large real-space dimensions of the cells, and the expected weak band dispersion, only the Γ-point of the Brillouin zone was used in the calculations. In a first step, full geometry optimizations were performed, including both atom positions and lattice parameters. No symmetry constraints were applied, calculations were performed on the rhombohedral cells with the cell angle slightly distorted from the special value (109.47°) corresponding to the body-centered cubic (bcc) structure. The reason for this is that, while some ZIFs with **sod** topology retain the ideal cubic structure (e.g. Zn(mIm)$_2$), others are known from experiment to distort into a less symmetric hexagonal form (e.g. Zn(bIm)$_2$), which corresponds to an angle different from 109.47° in the primitive rhombohedral cell.[246]

Since there are 12 linker sites in the primitive rhombohedral cell, the mixed solids with composition ZnXY can be arranged in multiple configurations of 6 X and 6 Y linkers. To generate the mixed configurations the starting point was two well-ordered structures

for each composition, in such a way that the symmetry of the mixed configurations is maximized (thus speeding up the calculation), and then the most stable of the two was analysed further. In the "undistorted" cubic sodalite structure (Figure 6.4a), all linker sites are equivalent. In the absence of any additional symmetry breaking (e.g. due to the molecular structure of the linker), the structure has 4 three-fold rotation axes along the cube diagonals, which define the main pores of the **sod** topology (Figure 6.4b). The primitive cell corresponding to the cubic sodalite structure is a rhombohedron with cell angle 109.47°. The hexagonal distortion occurs when the rhombohedral angle deviates from this ideal value, which leads to the hexagonal conventional cell in Figure 6.4c,d. There are two symmetrically distinct linker sites, represented by blue and red spheres in Figure 6.4c,d. Only one of the 4 main pore directions conserves the three-fold rotation symmetry, which is the one perpendicular to the basal plane of the hexagonal structure (Figure 6.4c). The rings defining this unique pore contain six symmetrically equivalent anion sites (blue in the figure). In contrast, the other three pores contain a mixture of 4 red and 2 blue sites in the ring, and do not have the original 3-fold rotation symmetry.
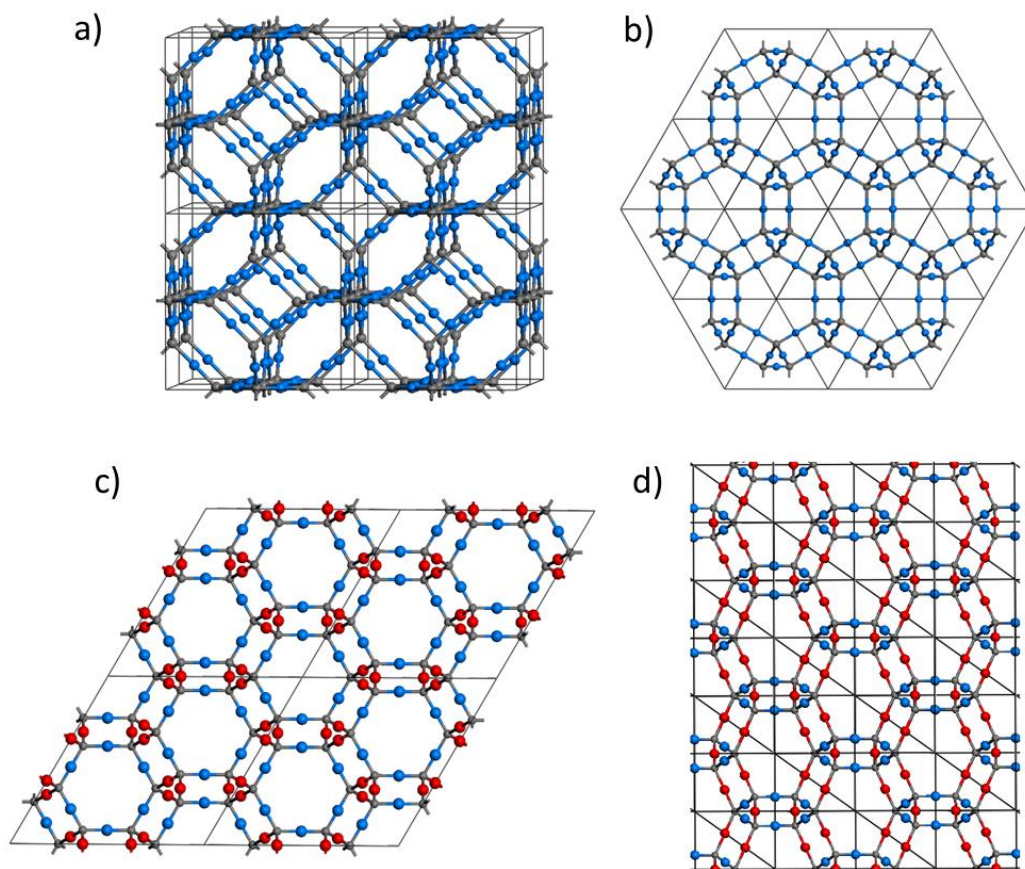
Figure 6.4. Schematic representation of the sod topology with cubic structure (a, b) and with hexagonal structure (c, d). Gray spheres represent the cations (Zn in our case) and blue or red represent the anion (imidazolate linkers in our case). Two anion colours are used to indicate the symmetrically distinct anion sites in the hexagonal structure.

It is clear then that the maximally ordered structures with 50:50 mixture of anions are the ones where each anion species occupies only one symmetrically distinct site. There are two inequivalent configurations of this type, which do not break the symmetry of the hexagonal lattice. Since nIm is always used as one of the linkers in the mixed structures, configuration 1 is described as the configuration where only the nIm linker is in the unique-pore rings, and configuration 2 is referred to as the inverted configuration (Figure 6.5).

156
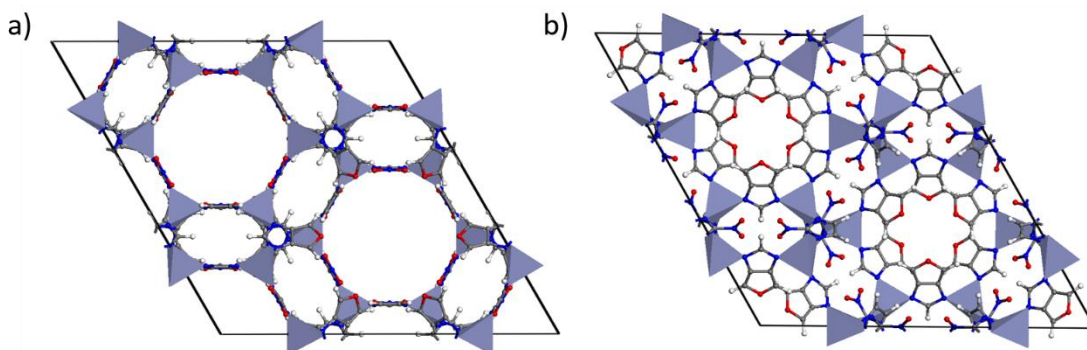
Figure 6.5. Mixed ZIF with composition Zn(fIm)(nIm) a) in the sod topology (configuration 1) and b) in the lta inverted topology (configuration 2)

Geometry optimizations were performed with the PBE functional,[69] corrected with Grimme's D2 method for including dispersion interactions.[80] In a second step, accurate electronic structures were obtained from single-point calculations with the HSE06 screened hybrid functional,[76, 77] which generally provides band-gaps in close agreement with experiment.[78] In the case of Co-containing ZIFs, both low-spin and high-spin configurations were tried, in order to identify the groundstate (high-spin). The alignment of the electronic energies with the vacuum scale was performed using the method proposed by Butler *et al* was used,[82] evaluating the average potential within a small sphere (radius of 0.3 Å) at the pore.

6.3 Results and Discussion

6.3.1 Crystal structure

The optimized cell parameters of the cells are shown in Table 6.1 and given in the hexagonal setting for convenience. Note that some of the structures (Zn(abIm)$_2$, Zn(acIm)$_2$ and Zn(pur)$_2$) exhibit a small distortion from the hexagonal symmetry. Whilst this may hinder their synthesis in the **sod** topology it is expected that they could still be formed under the right conditions due to the flexibility of the **sod** topology. It is however noted that Zn(abIm)$_2$ and Zn(pur)$_2$ have been reported experimentally in the LTA topology.[241]

Table 6.1 Optimized lattice parameters for the hexagonal cells of ZIF crystal structures with sodalite topology.

Linker	a (Å)	b (Å)	c (Å)	α (°)	β (°)	γ (°)
bIm	22.37	22.37	16.09	90.00	90.00	120.00
dcIm	22.44	22.44	16.04	90.00	90.00	120.00
dcnIm	23.16	23.16	16.12	90.00	90.00	120.00
fIm	21.81	21.81	15.90	90.00	90.00	120.00
Ica	24.29	24.29	14.91	90.00	90.00	120.00
Im	22.38	22.38	16.23	90.00	90.00	120.00
mIm	22.83	22.83	15.94	90.00	90.00	120.00
nIm	24.30	24.30	14.51	90.00	90.00	120.00
tIm	22.52	22.52	15.87	90.00	90.00	120.00
abIm	**22.28**	**22.42**	**16.05**	**90.28**	**90.06**	**120.03**
acIm	**22.09**	**22.14**	**15.96**	**90.32**	**89.92**	**120.11**
pur	**22.03**	**22.17**	**16.02**	**90.25**	**90.10**	**120.29**
fIm/nIm	24.63	24.63	13.64	90.00	90.00	120.00
Im/nIm	22.72	22.72	16.24	90.00	90.00	120.00
mIm/nIm	24.96	24.96	14.30	90.00	90.00	120.00

6.3.2 Electronic structure

The electronic structure was determined using density functional theory (DFT) with a screened hybrid density functional,[76, 77] and the electronic levels were aligned with the vacuum scale.[82] The band edges in these molecular solids, which are better referred to as the highest occupied crystal orbital (HOCO) and lowest unoccupied crystal orbital (LUCO) levels, are shown in Figure 6.7b. The widest HOCO-LUCO gap is obtained in the case of the bare imidazole linker, *i.e.* for $Zn(Im)_2$ (5.2 eV), while the narrowest gap corresponds to $Zn(nIm)_2$ (3.3 eV). The wide range observed illustrates the tunability of the electronic properties of ZIFs upon linker modification, which is consistent with previous theoretical and experimental findings for other MOFs families.[247-249] In order to test their suitability for water-splitting the band edges should straddle the redox potentials

for water photolysis,[21-23] In the periodic solid the potential at the pore was taken as the vacuum potential as was the case in Chapter 5. Figure **6.6** shows the results of the pore potentials along the 111 direction. Each ZIF shows a flat region at position (0,0,0) and can be assumed that at this point there is no electric field. The potential at this point (Table 6.2) was used as the vacuum potential in the band alignment of the ZIFs.
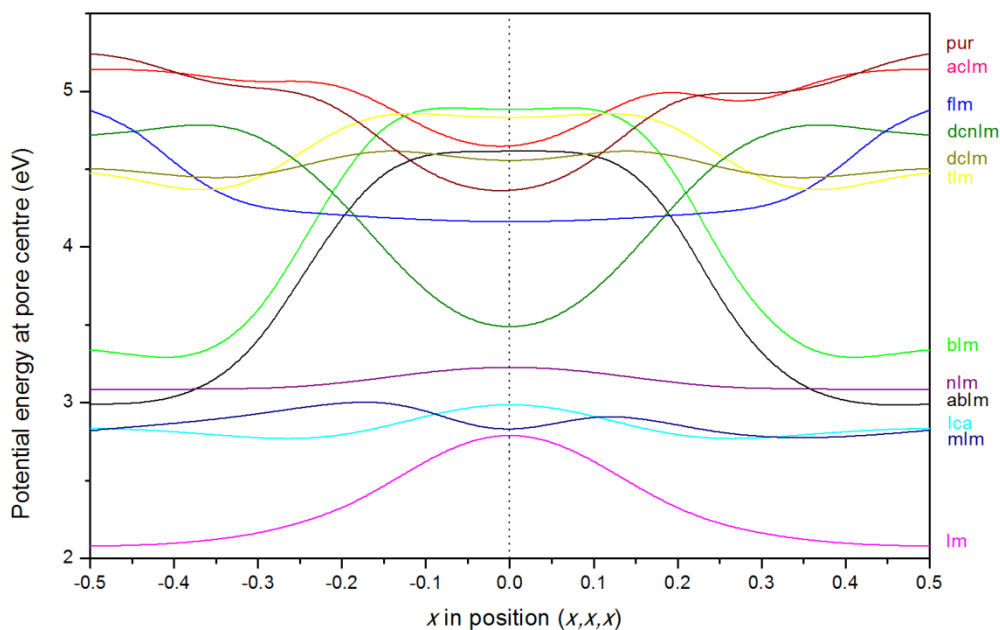
Figure 6**.**6**. Electrostatic potential variation across the direction (111) at the pore centre**

Table 6.2. Potential energies at the vacuum (with respect to average potential in crystal).

ZIF	Potential energy at pore centre (eV)	ZIF	Potential energy at pore centre (eV)
pur	4.35	bIm	4.88
acIm	4.63	nIm	3.22
fIm	4.16	abIm	4.61
dcnIm	3.47	Ica	2.99
dcIm	4.55	mIm	2.82
tIm	4.83	Im	2.80

After aligning the band edges to the vacuum level, (Figure 6.7b) it is clear that the HOCO and LUCO levels of the ZnX_2 ZIF structures straddle the redox levels for both

water splitting and methane/methanol synthesis. However, for these photocatalysts to work efficiently under solar radiation, a narrower bandgap of around 2 eV is desirable, as this would allow the absorption of the visible range solar spectrum, which carries most of the solar radiation energy. Furthermore, the bandgaps of these single-linker ZIFs correspond to intra-linker excitations, which is not convenient for photocatalysis, because some degree of electron-hole separation is needed to prevent fast recombination of the charge carriers.[232]

In order to reduce the band gap hypothetical ZIFs were generated by mixing different linkers within the same structure. To tailor the band edges to the required positions and to attain electron-hole separation via inter-linker excitations a low-LUCO linker (X=nIm) was mixed with a high-HOCO linker (Y=Im, mIm, or fIm) to form ZnXY structures with potential low-energy inter-linker excitations. In these 50:50 mixed-linker structures, two well-defined ordered configurations can be formed, considering the symmetry of the lattice. For each composition, the relative energy of each configuration was determined as

$$E_{\text{mix}}[\text{ZnXY}] = E[\text{ZnXY}] - \frac{1}{2}E[\text{ZnX}] - \frac{1}{2}E[\text{ZnY}] \tag{6.1}$$

and in each case the mixed ZIF was shown to be significantly stable with respect to the separated pure phases (by 0.2-0.4 eV per formula unit, Table 6.3), which indeed suggests they should be able to form experimentally.

Table 6.3. Mixing energies of the two maximally-ordered configurations of mixed ZIFs, as obtained from HSE calculations (in meV per formula unit). Underlined values mark the most stable configuration in each case.

Mixed ZIF	E_{mix}[Configuration 1]	E_{mix}[Configuration 1]
Zn(nIm)(Im)	-238	<u>-362</u>
Zn(nIm)(mIm)	+41	<u>-358</u>
Zn(nIm)(fIm)	<u>-228</u>	+315

Figure 6.7c shows the HOCO and LUCO levels for the most stable mixed ZIF of each composition. They perfectly straddle the targeted redox potentials and lead to gaps of 1.9-2.8 eV, which are very convenient for applications involving solar light absorption. The projected electronic density of states in the mixed ZIFs (Figure 6.8) shown for the Co and Cu analogue phases confirms that the LUCO is mainly contributed by the nitro group in the nIm linker, while the HOCO is contributed by the second linker.

This linker "mix and match" method can then be used more generally to target desired electronic structures of ZIFs for photocatalytic applications. The reason why the procedure works becomes apparent from examining the energies of the highest-occupied (HOMO) and lowest-unoccupied (LUMO) molecular orbitals of the isolated linkers. The HOMO and LUMO of the neutral molecules HX are represented as crosses in Figure 6.7b (and also in Figure 6.7c, but using the higher HOMO and the lower LUMO between the two mixed-in linkers). Despite some fluctuations, the HOCO/LUCO levels in the ZIFs follow the same trend as the HOMO/LUMO levels in the corresponding gas-phase linker molecules.
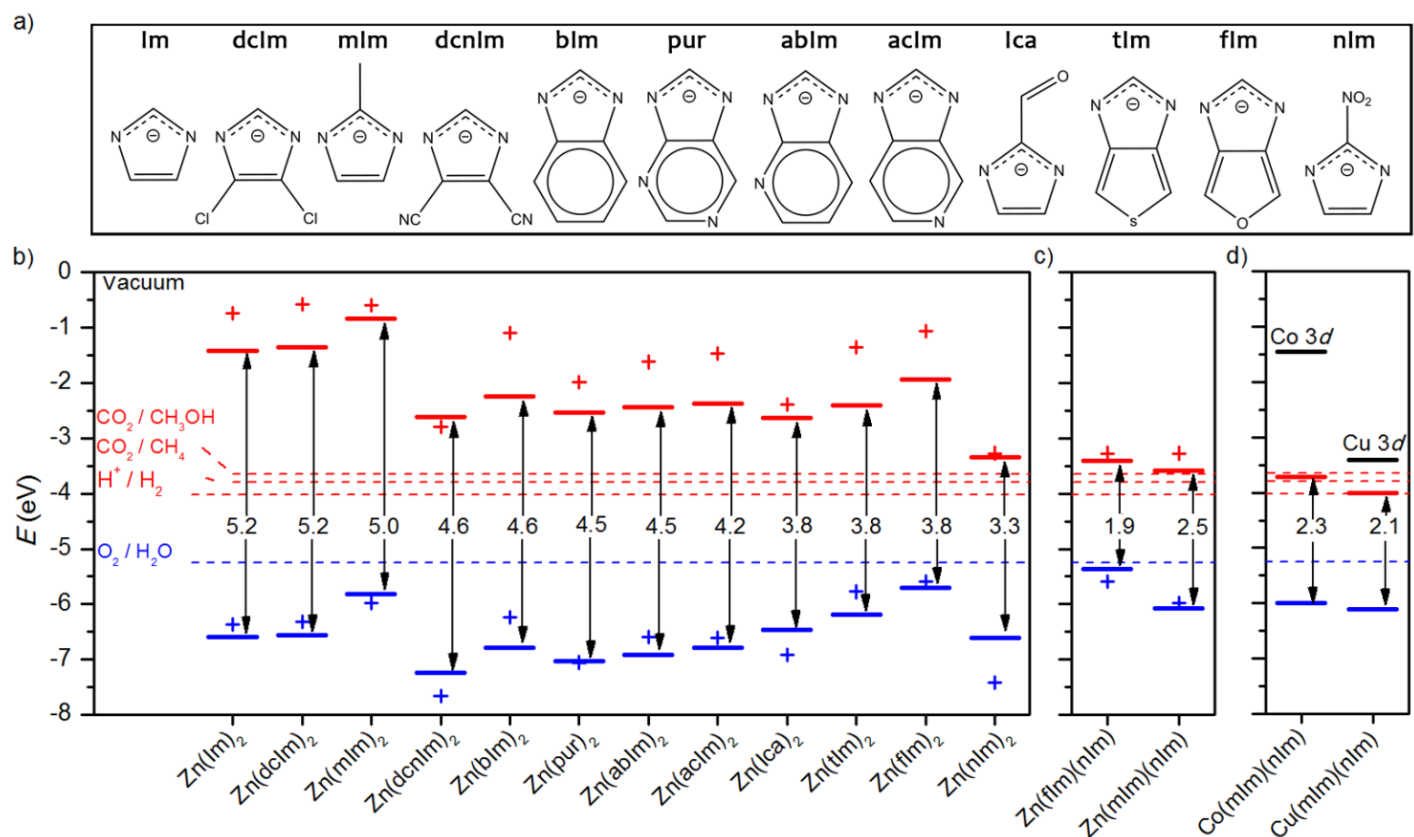
Figure 6.7. a) List of linkers (X) in the ZIF structures with composition ZnX$_2$. **b)** Positions of the highest occupied energy levels (blue) and lowest unoccupied energy levels (red) of the ZnX$_2$ crystal structures (lines), and of the isolated HX molecules (crosses). The potentials for H$_2$O splitting and two different CO$_2$ reduction reactions are shown as dashed lines. **c)** Idem for the mixed ZIF structures created by combining nIm with Im, mIm or fIm linkers; the crosses here represent the higher HOMO (blue) and the lower LUMO (red) between the two mixed linkers. **d)** Idem for mixed mIm/nIm ZIF structures with Co or Cu centers.
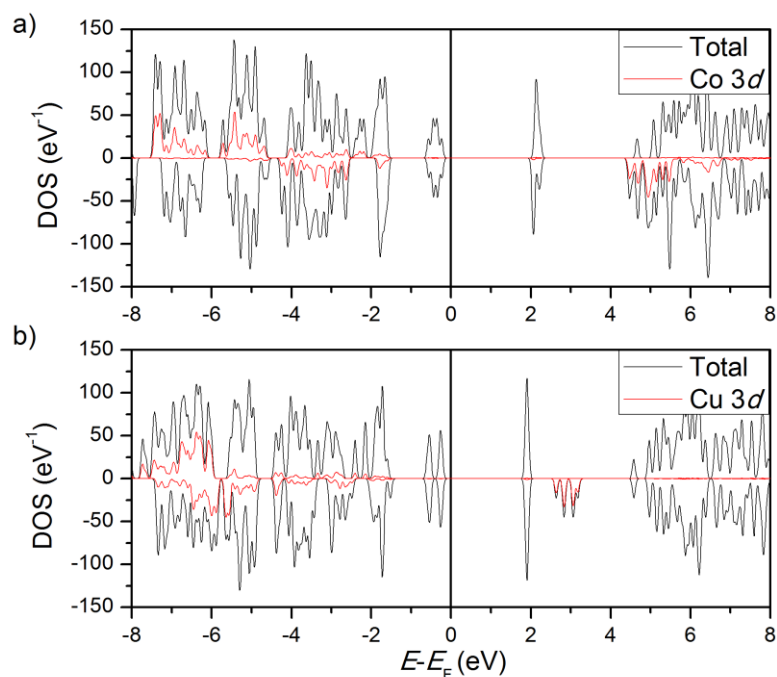
Figure 6.8. Total and 3d-projected electronic density of states (DOS) corresponding mixed-linker ZIF structures a) Co(mIm)(nIm) and b) Cu(mIm)(nIm).

As Figure 6.9 shows, there is an excellent correlation between the excitation gaps in the linkers and those in the corresponding ZIFs. The correlation extends to the mixed-linker ZIFs, if we take the difference between the higher HOMO and the lower LUMO between the two linkers. It is clear from this analysis that the positions of the band edges in the crystalline material are determined, to a large extent, by the frontier orbitals of the linkers. A larger list of modified imidazolate linkers, and their HOMO and LUMO, are reported in the Supporting Information in Ref. [250]. The motivation is that this list can serve as a reference for the electronic structures of functionalized ZIF linkers, and as a starting point for future design of mixed-linker ZIFs with tailored bands.
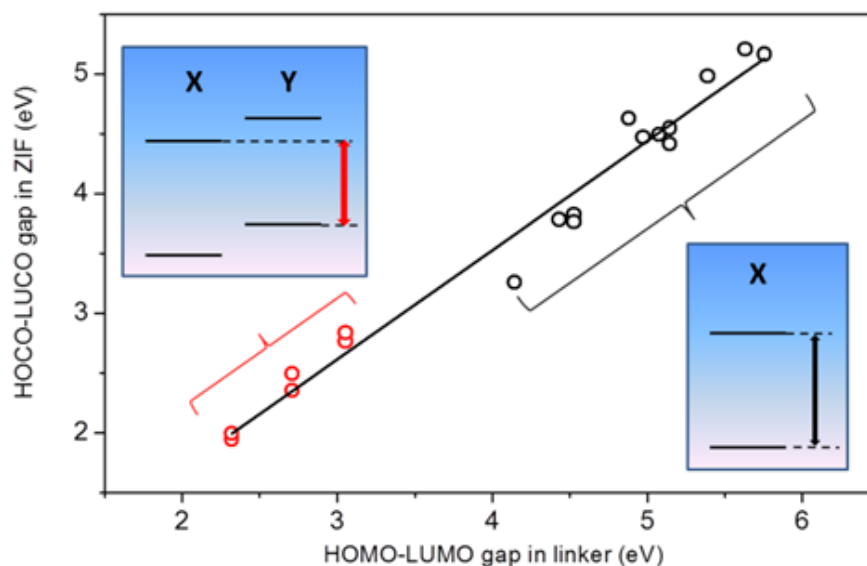
Figure 6.9. Correlation between the HOCO-LUCO gaps of the ZIF solids (ZnX$_2$ or ZnXY) and the HOMO-LUMO gaps of the protonated linkers in gas phase. Red circles correspond to inter-linker transitions in mixed ZIFs (there are two points for each mixed composition, corresponding to the two ordered configurations).

Finally, it is important to discuss how the electronic properties of the proposed ZIFs are modified by the presence of transition metal cations (instead of Zn) in the tetrahedral sites. The established picture of photocatalysis by MOFs requires that photoexcitations involve ligand-to-metal charge transfer (LMCT),[231, 251] because this allows i) strong light absorption due to the redox nature of the metal centre, and ii) effective electron-hole separation to minimize recombination. While the mixed-linker Zn-based ZIFs proposed above exhibit a fundamental gap involving charge separation (from one kind of linker to the other), such excitation might not occur from optical absorption, because it would involve charge transfer through the Zn(II) centre, which does not have any empty levels at the same energy range as the LUCO. Furthermore, even if the inter-linker charge transfer in the Zn-based mixed ZIFs was possible, the absence of a metal redox center might lead to light absorption that is too weak for the system to work as an efficient photocatalyst.

To address this Co and Cu have been considered at the tetrahedral sites of the mIm/nIm mixed ZIF. These two metals are chosen because they are known from experiment to incorporate in ZIF structures, and in fact they constitute the metal centers in two reported ZIF photocatalysts.[244, 245] Figure 6.7d shows that these transition metals introduce empty d-levels above the LUCO level of the ZIF. In the case of Co, the empty d-band edge is too high, but in the case of Cu the empty d-band edge is only about 0.6 eV above the LUCO. In fact, in the latter case the LUCO and the Cu $3d$ band clearly interact leading to some lowering of the LUCO energy. The presence of Cu and the overlap of its empty $3d$ levels with the LUCO of the ZIFs have important implications for photocatalysis. The photoadsorption leading to electron excitation would be stronger thanks to the Cu(II)/Cu(I) redox pair. In addition, the hybrid nature of the conduction edge leads to a delocalization of the excited electron which would compete with recombination to the HOCO, thus increasing the lifetime of the excitation. This picture is consistent with recent experimental measurements in ZIFs with composition Co(mIm)$_2$, where it was observed that the hybrid nature of the excited state led to longer charge carrier lifetimes.[252] The potential advantage of our mixed-linker ZIFs is that they offer unique flexibility to simultaneously tune the bandgap and achieve overlap between the ZIF LUCO and the empty metal levels.

6.4   Conclusions

The band alignment for a number of known and hypothetical Zn-based ZIFs with respect to the vacuum level is presented. This work illustrates a conceptually simple route to engineer the band structure of ZIFs, based on the mixing of linkers within the framework, to target photocatalytic applications. Structures with a single type of linker exhibit relatively wide bandgaps; however, by mixing linkers of a low-lying conduction edge with linkers of a high-lying valence edge, materials with ideal band positions for

visible-light water splitting and CO_2 reduction photocatalysis can be predicted. It is shown that using this linker mix-and-match approach it is possible to design new ZIF materials which i) are thermodynamically stable with respect to the pure ones, ii) have narrower bandgaps, of the required magnitude for solar light absorption, and iii) have band edges in with ideal positions for visible-light water splitting and CO_2 reduction photocatalysis.

By introducing copper in the tetrahedral position of the mixed-linker ZIFs, it is possible to increase photo-absorption and simultaneously extend the electron-hole recombination times, thanks to the overlap of the empty metal d-levels with the lowest unoccupied crystal orbitals in this structure. Further theoretical and experimental work is required to establish whether these excitations are indeed optically accessible, as there can be thermodynamic and/or kinetic limitations to the charge transfer process involved in such transitions.

7   Summary

7.1   Overview

The work presented in this thesis demonstrates the usefulness of electronic structure calculations of materials as a basis to understanding and optimising their thermoelectric and photocatalytic properties.

Electron transport properties were calculated for both metals and semiconductors. For semiconductors, accurate band structures were obtained using the HSE06 functional. For the sake of computational efficiency, calculations were first performed on a coarse k-grid, and then interpolated onto a fine k-grid using Wannier functions. Phonon transport properties were calculated from harmonic and anharmonic lattice dynamics calculations by considering phonon-phonon scattering events. At this level of theory, the electron scattering rates were not calculated but determined from experiment. Disorder in solid solutions was investigated by representing the system as a symmetry-adapted ensemble of configurations. Properties were then calculated as an average value over the ensemble. For photocatalysis band alignment to the vacuum potential was performed by taking the vacuum reference to be the electrostatic potential at the centre of the largest pore, ensuring the gradient at this point was zero.

In Chapter 3, excellent agreement for the electronic and phonon transport properties of the shandite-structured $Ni_3Sn_2S_2$ were obtained. $Ni_3Sn_2S_2$ was confirmed as exhibiting a metallic and nonmagnetic ground state with Ni^0 oxidation. Seebeck coefficients obtained from theoretical calculations are in excellent agreement with those measured experimentally between 100 and 600 K. The linear dependence of electron scattering rates with temperatures between 300 and 600 K, showed the dominant electron-scattering mechanism in this temperature range is via phonons. The electronic thermal

conductivity, which deviates only slightly from the Wiedemann-Franz law, provides the main contribution to thermal transport. Overall, $Ni_3Sn_2S_2$ is a poor thermoelectric material (ZT ~ 0.01 at 300 K), principally due to the low absolute value of the Seebeck coefficient. Optimisation of the transport properties in the shandite system was possible by substitution. In the half-metallic paramagnetic $Co_3Sn_2S_2$ phase it was found that the antiferromagnetic configuration gave a better description of the thermopower of the paramagnetic phase, but the model was still not able to accurately predict the experimental values. This may be attributed to the failure of the models to describe spin-flip scattering events which are not included in our models. Electronic structure calculations also show that at an equal concentration of In and Sn in Co_3SnInS_2, the electron transport properties would be optimal, due to its intrinsic semi-conducting nature and this was confirmed by experiment. Indium preferentially occupies the interlayer site in the shandite system due to bonding constraints. In has one less valence electron than tin and occupies the interlayer site, where only one *p*-orbital is needed to be occupied, rather than two in the intralayer site.

In Chapter 4, excellent agreement was obtained between the calculated and experimentally observed lattice parameters of the quaternary chalcogenides. The Ag-containing structures were all found to be formed in the kesterite I configuration. In contrast for the Cu-containing structures a probability distribution exists between kesterite I and II. In both cases this was confirmed by experiment. In the Cu-containing structures the nature of the disorder is suggested to be a stacking disorder. Accurate band structure calculations were calculated and interpolated onto dense k-grids to investigate their transport properties. Across the different quaternary chalcogenides investigated atomic substitution led only to a shift in the band gap. The investigation of CZTSe which has the smallest band gap of the kesterites investigated showed that its *ZT* can be

improved by doping. The experimentally reported Seebeck coefficient are in semi-quantitative agreement with experiment and confirmed the structure as a *p*-type semiconductor. The work presented the transport properties as a function of carrier concentration which is encouraging, as it shows a combined theoretical and experimental approach to the optimisation of the *ZT* as a function of carrier concentration.

In Chapter 5, the electronic structure of PMOFs are investigated, by aligning the electron levels with a vacuum level, the band edges are calculated and are shown to be primarily determined by the octahedral metal centre rather than the porphyrin metal centre. As in Chapter 3 the optimal properties can be achieved by chemical substitution. The substitution of Fe at the porphyrin metal centre has the effect of slightly raising the position of the valence band edge, whereas Fe at the octahedral metal node has the ability to significantly lower the position of the conduction band edge on the absolute scale. Iron is therefore a very useful dopant to engineer the band structure and alignment of these MOFs. The optimal band gap is achieved by partial substitution of Al by Fe at the octahedral sites while keeping Zn at the porphyrin centres.

In Chapter 6, substitution is again employed to optimise the required properties of the ZIFs. It was found that the band edge positions were primarily dependent on the choice of molecular ligand. It is shown that by mixing linkers of a low-lying conduction edge with linkers of a high-lying valence edge, the band positions for visible-light water splitting and CO_2 reduction photocatalysis can be accurately predicted. Further substitution of zinc by copper in the tetrahedral position of the mixed-linker ZIFs is shown to introduce of empty *d*-bands just above the LUCO. The overlap of these empty *d*-bands and the LUCO are beneficial for photocatalysis as the photoadsorption leading to electron excitation would be stronger thanks to the Cu^{II}/Cu^{I} redox pair. In addition, the hybrid nature of the conduction edge leads to a delocalization of the excited electron which

would compete with recombination to the HOCO, thus increasing the lifetime of the excitation recombination times which is consistent with recent experiments.

The theoretical calculations performed in this thesis have led to insight and understanding into the thermoelectric and photocatalytic properties of chalcogenides and MOFs. In the chalcogenide materials underlying mechanisms of disorder have been explained and throughout the thesis it has been shown that the material properties can be optimized through chemical substitution or doping.

7.2   Future Work

7.2.1   Incorporation of spin scattering events for paramagnetic systems

In spin-polarized systems the Seebeck coefficients are calculated within the two-current model as a weighted average of the spin-up and spin-down channels. While this is valid for ferromagnetic systems, in paramagnetic systems where electrons can flip between channels theoretical results were unable to reproduce experimental data. This may be attributed to the failure of the models to describe spin-flip scattering events which are not included in our models. A more accurate model needs to be developed in future work.

7.2.2   Electron scattering rates

In Chapter 3 and 4 the electron scattering rates of the chalcogenides investigated were not explicitly calculated from theory, but rather a combination of theory and experiment. The results show in the temperature of interest around and above the Debye temperature electron scattering by phonons is the dominant scattering mechanism. A future direction of this work is to apply the electron-phonon Wannier (EPW) code[136] to explicitly calculate the electron scattering rates by phonons. In Chapter 4 the accurate projections needed to calculate the MLWF for the quaternary chalcogenides have already

been determined. However, it is noted that these calculations require a large amount of computer resources.

7.2.3 Modelling dopants in quaternary chalcogenides

The electron transport properties of the CZTS and CZTSe systems were performed within the rigid band approximation. A more accurate approach would be to include the dopant explicitly into the electron structure calculation. In both cases the compositions are shown to be *p*-type and could be modelled by the removal of one electron, the substitution of one Zn atom for a Cu atom in a 64-atom supercell would lead to carrier concentrations of around 7×10^{20} cm^{-3}, which are in line with those reported in the literature.

7.2.4 High-throughput approach to *ZT* enhancement for thermoelectrics

The high throughput approach is used effectively to data mine for materials with the desired properties. A continuation of this work could be to assign a "descriptor" to identify a property of interest, that would allow a dataset to be screened. One such online repository is the Automatic – FLOW for Materials Discovery (AFLOWLIB) database with over 1,600,000 material compounds. Alternatively new high-throughput calculations could be performed using AFLOWπ.[253] AFLOWπ allows electronic structure calculations to be performed on large sets of calculations running them in parallel to determine band structures, density of states and transport properties for groups of materials of which promising materials could then be synthesized experimentally.

8   References

1. J. Conti, P. Holtberg, J. Diefenderfer, A. LaRose, J. T. Turnure and L. Westfall, *International Energy Outlook 2016* Report DOE/EIA-0484, U.S. Energy Information Administration Washington DC, 2016.

2. D. M. Rowe, *Thermoelectrics handbook: macro to nano*, CRC/Taylor & Francis, Boca Raton, 2006.

3. J. Corps, P. Vaqueiro and A. V. Powell, *J. Mater. Chem. A*, 2013, **1**, 6553-6557.

4. M. Martín-González, O. Caballero-Calero and P. Díaz-Chao, *Renew. Sustainable Energy Rev.*, 2013, **24**, 288-305.

5. W. Xie, A. Weidenkaff, X. Tang, Q. Zhang, J. Poon and T. Tritt, *Nanomaterials*, 2012, **2**, 379-412.

6. U. Müller, *Inorganic structural chemistry*, Wiley, Chichester, England; Hoboken, NJ, 2nd edn., 2007.

7. C. L. Wan, Y. F. Wang, N. Wang, W. Norimatsu, M. Kusunoki and K. Koumoto, *Sci. Tech. Adv. Mater*, 2010, **11**, 044306.

8. G. J. Snyder and E. S. Toberer, *Nat. Mater.*, 2008, **7**, 105-114.

9. R. Bjork and K. K. Nielsen, *Solar Energy*, 2015, **120**, 187-194.

10. O. Beeri, O. Rotem, E. Hazan, E. A. Katz, A. Braun and Y. Gelbstein, *J. Appl. Phys.*, 2015, **118**, 115104.

11. M. Zabel, S. Wandinger and K. J. Range, *Z. Naturforsch., B: Chem. Sci.*, 1979, **34**, 238-241.

12. J. Kim, H. Hiroi, T. K. Todorov, O. Gunawan, M. Kuwahara, T. Gokmen, D. Nair, M. Hopstaken, B. Shin, Y. S. Lee, W. Wang, H. Sugimoto and D. B. Mitzi, *Adv. Mater.*, 2014, **26**, 7427-7431.

13. W. Wang, M. T. Winkler, O. Gunawan, T. Gokmen, T. K. Todorov, Y. Zhu and D. B. Mitzi, *Adv. Energy Mater.*, 2014, **4**, 1301465.

14. C. Sevik and T. Çağın, *Appl. Phys. Lett.*, 2009, **95**, 112105.

15. K. Suekuni and T. Takabatake, *Apl Materials*, 2016, **4**, 104503.

16. G. Sneddon, A. Greenaway and H. H. P. Yiu, *Adv. Energy Mater.*, 2014, **4**, 1301873.

17. A. M. Appel, J. E. Bercaw, A. B. Bocarsly, H. Dobbek, D. L. DuBois, M. Dupuis, J. G. Ferry, E. Fujita, R. Hille, P. J. A. Kenis, C. A. Kerfeld, R. H. Morris, C. H. F. Peden, A. R. Portis, S. W. Ragsdale, T. B. Rauchfuss, J. N. H. Reek, L. C. Seefeldt, R. K. Thauer and G. L. Waldrop, *Chem. Rev.*, 2013, **113**, 6621-6658.

18. A. Kubacka, M. Fernández-García and G. Colón, *Chem. Rev.*, 2012, **112**, 1555-1614.

19. X. Zou and Y. Zhang, *Chem. Soc. Rev.*, 2015, **44**, 5148-5180.

20. A. Kudo and Y. Miseki, *Chem. Soc. Rev.*, 2009, **38**, 253-278.

21. H. Wang, L. Zhang, Z. Chen, J. Hu, S. Li, Z. Wang, J. Liu and X. Wang, *Chem. Soc. Rev.*, 2014, **43**, 5234-5244.

22. M. G. Walter, E. L. Warren, J. R. McKone, S. W. Boettcher, Q. Mi, E. A. Santori and N. S. Lewis, *Chem. Rev.*, 2010, **110**, 6446-6473.

23. T. Hisatomi, J. Kubota and K. Domen, *Chem. Soc. Rev.*, 2014, **43**, 7520-7535.

24. A. Fujishima and K. Honda, *Nature*, 1972, **238**, 37-38.

25. S. Protti, A. Albini and N. Serpone, *Phys. Chem. Chem. Phys.*, 2014, **16**, 19790-19827.

26. S. Dahl and I. Chorkendorff, *Nat Mater*, 2012, **11**, 100-101.

27. W. Tu, Y. Zhou and Z. Zou, *Adv. Mater.*, 2014, **26**, 4607-4626.

28. X. Chen, S. Shen, L. Guo and S. S. Mao, *Chem. Rev.*, 2010, **110**, 6503-6570.

29. M. Ni, M. K. H. Leung, D. Y. C. Leung and K. Sumathy, *Renew. Sustainable Energy Rev.*, 2007, **11**, 401-425.

30. V. P. Indrakanti, J. D. Kubicki and H. H. Schobert, *Energy & Environ. Sci.*, 2009, **2**, 745-758.

31. K. S. Joya, Y. F. Joya, K. Ocakoglu and R. van de Krol, *Angew. Chem. Int. Ed.*, 2013, **52**, 10426-10437.

32. D. J. Martin, K. Qiu, S. A. Shevlin, A. D. Handoko, X. Chen, Z. Guo and J. Tang, *Angew. Chem. Int. Ed.*, 2014, **53**, 9240-9245.

33. Q. Xiang and J. Yu, *J. Phys. Chem. Lett.*, 2013, **4**, 753-759.

34. Q. Xiang, J. Yu and M. Jaroniec, *Chem. Soc. Rev.*, 2012, **41**, 782-796.

35. S. N. Shirodkar, U. V. Waghmare, T. S. Fisher and R. Grau-Crespo, *Phys. Chem. Chem. Phys.*, 2015, **17**, 13547-13552.

36. J. Xiong, W. M. Fischer, K. Inoue, M. Nakahara and C. E. Bauer, *Science*, 2000, **289**, 1724-1730.

37. F. Fresno, R. Portela, S. Suarez and J. M. Coronado, *J. Mater. Chem. A*, 2014, **2**, 2863-2884.

38. M. Grätzel, *Nature*, 2001, **414**, 338-344.

39. K. Maeda and K. Domen, *J. Phys. Chem. Lett.*, 2010, **1**, 2655-2661.

40. G. C. Dismukes, R. Brimblecombe, G. A. N. Felton, R. S. Pryadun, J. E. Sheats, L. Spiccia and G. F. Swiegers, *Acc. Chem. Res.*, 2009, **42**, 1935-1943.

41. J. Z. Wu, F. De Angelis, T. G. Carrell, G. P. A. Yap, J. Sheats, R. Car and G. C. Dismukes, *lnorg. Chem.*, 2006, **45**, 189-195.

42. M. Yagi, A. Syouji, S. Yamada, M. Komi, H. Yamazaki and S. Tajima, *Photochem. Photobiol. Sci.*, 2009, **8**, 139-147.

43. S. L. Gould, G. Kodis, R. E. Palacios, L. de la Garza, A. Brune, D. Gust, T. A. Moore and A. L. Moore, *J. Phys. Chem. B*, 2004, **108**, 10566-10580.

44. G. McLendon and D. S. Miller, *J. Chem. Soc. Chem. Comm.*, 1980, DOI: 10.1039/c39800000533, 533-534.

45. A. Choplin and F. Quignard, *Coord. Chem. Rev.*, 1998, **178–180**, 1679–1702.

46. A. Thomas and M. Driess, *Angew. Chem. Int. Ed.*, 2009, **48**, 1890–1892.

47. D. Wang, R. Huang, W. Liu, D. Sun and Z. Li, *ACS Catalysis*, 2014, **4**, 4254-4260.

48. Y. Fu, D. Sun, Y. Chen, R. Huang, Z. Ding, X. Fu and Z. Li, *Angewandte Chemie International Edition*, 2012, **51**, 3364-3367.

49. T. Zhang and W. Lin, *Chem. Soc. Rev.*, 2014, **43**, 5982-5993.

50. Y. Lee, S. Kim, J. K. Kang and S. M. Cohen, *Chem. Comm.*, 2015, **51**, 5735-5738.

51. M. H. Alkordi, Y. Liu, R. W. Larsen, J. F. Eubank and M. Eddaoudi, *J. Am. Chem. Soc.*, 2008, **130** 12639–12641.

52. C. Wang , K. E. deKrafft and W. Lin, *J. Am. Chem. Soc*, 2012, **134** 7211–7214.

53. J. Juan-Alcaniz, J. Gascon and F. Kapteijn, *J. Mater. Chem.*, 2012, **22**, 10102-10118.

54. F. G. Cirujano, A. Leyva-Perez, A. Corma and F. X. Llabres i Xamena, *ChemCatChem*, 2013, **5**, 538 – 549.

55. J. Y. Lee, O. K. Farha, J. Roberts, K. A. Scheidt, S. T. Nguyen and J. T. Hupp, *Chem. Soc. Rev.*, 2009, **38**, 1450–1459.

56. F. X. Llabrés i Xamena, A. Abad, A. Corma and H. Garcia, *J. Catal.*, 2007 **250**, 294–298.

57. L. M. Rodriguez-Albelo, A. R. Ruiz-Salvador, S. Sampieri, D. W. Lewis, A. Gomez, B. Nohra, P. Mialane, J. Marrot, F. Secheresse, C. Mellot-Draznieks, R. Ngo Biboum, B. Keita, L. Nadjo and A. Dolbecq, *J. Am. Chem. Soc.*, 2009, **131** 16078–16087.

58. F. Vermoortele, B. Bueken, G. Le Bars, B. Van de Voorde, M. Vandichel, K. Houthoofd, A. Vimont, M. Daturi, M. Waroquier, V. Van Speybroeck, C. Kirschhock and D. E. De Vos, *J. Am. Chem. Soc.*, 1013, **135** 11465–11468.

59. M. E. Kosal, J.-H. Chou, S. R. Wilson and K. S. Suslick, *Nat. Mater.*, 2002, **1**, 118 - 121.

60. C. Zou and C.-D. Wu, *Dalton Trans.*, 2012, **41**, 3879-3888.

61. W.-Y. Gao, M. Chrzanowski and S. Ma, *Chem. Soc. Rev.*, 2014, **43**, 5841-5866.

62. A. Fateeva, P. A. Chater, C. P. Ireland, A. A. Tahir, Y. Z. Khimyak, P. V. Wiper, J. R. Darwent and M. J. Rosseinsky, *Angew. Chem. Int. Ed.*, 2012, **51**, 7440-7444.

63. A. Fateeva, J. Clarisse, G. Pilet, J.-M. Grenèche, F. Nouar, B. K. Abeykoon, F. Guegan, C. Goutaudie, D. Luneau, J. E. Warren, M. J. Rosseinsky and T. Devic, *Cryst. Growth Des.*, 2015, **15** 1819-1826.

64. I. N. Levine, *Quantum chemistry*, Pearson, Boston, 7th edn., 2013.

65. M. Born and R. Oppenheimer, *Ann. Phys.*, 1927, **389**, 457-484.

66. P. W. Atkins and R. S. Friedman, *Molecular quantum mechanics*, Oxford University Press, New York, 5th edn., 2010.

67. P. Hohenberg and W. Kohn, *Phys. Rev.*, 1964, **136**, B864-B871.

68. W. Kohn and L. J. Sham, *Phys. Rev.*, 1965, **140**, A1133-A1138.

69.   J. P. Perdew, K. Burke and M. Ernzerhof, *Phys. Rev. Lett.*, 1996, **77**, 3865-3868.

70.   N. W. Ashcroft and N. D. Mermin, *Solid state physics*, Holt, New York, 1976.

71.   C. Kittel, *Introduction to solid state physics*, Wiley, Hoboken, NJ, 8th edn., 2005.

72.   P. Blaha, K. Schwarz, G. K. H. Madsen, D. Kvasnicka and J. Luitz, *WIEN2k, An Augmented Plane Wave + Local Orbitals Program for Calculating Crystal Properties*, Karlheinz Schwarz, Techn. Universität Wien, Austria, 2001.

73.   P. E. Blöchl, *Phys. Rev. B*, 1994, **50**, 17953-17979.

74.   G. Kresse and D. Joubert, *Phys. Rev. B*, 1999, **59**, 1758-1775.

75.   S. L. Dudarev, G. A. Botton, S. Y. Savrasov, C. J. Humphreys and A. P. Sutton, *Phys. Rev. B*, 1998, **57**, 1505-1509.

76.   J. Heyd, G. E. Scuseria and M. Ernzerhof, *J. Chem. Phys.*, 2003, **118**, 8207-8215.

77.   J. Heyd, G. E. Scuseria and M. Ernzerhof, *J. Chem. Phys.*, 2006, **124**, 219906.

78.   T. M. Henderson, J. Paier and G. E. Scuseria, *Phys. Status Solidi B*, 2011, **248**, 767-774.

79.   S. Grimme, *J. Comput. Chem.*, 2004, **25**, 1463-1473.

80.   S. Grimme, *J. Comput. Chem.*, 2006, **27**, 1787-1799.

81.   S. Grimme, J. Antony, S. Ehrlich and H. Krieg, *J. Chem. Phys.*, 2010, **132**, 154104.

82.   K. T. Butler, C. H. Hendon and A. Walsh, *J. Am. Chem. Soc.*, 2014, **136**, 2703-2706.

83.   T. M. Tritt, *Thermal conductivity: theory, properties, and applications*, Kluwer Academic/Plenum Publishers, New York, 2004.

84.   T. J. Scheidemantel, C. Ambrosch-Draxl, T. Thonhauser, J. V. Badding and J. O. Sofo, *Phys. Rev. B*, 2003, **68**, 125210.

85.   G. D. Mahan and J. O. Sofo, *Proc. Natl. Acad. Sci.*, 1996, **93**, 7436-7439.

86.   G. K. H. Madsen and D. J. Singh, *Comput. Phys. Commun.*, 2006, **175**, 67-71.

87.   J. Singleton, *Band theory and electronic properties of solids*, Oxford University Press, Oxford ; New York, 2001.

88.   W. Kohn, *Phys. Rev.*, 1959, **115**, 809-821.

89.   W. Kohn and J. R. Onffroy, *Phys. Rev. B*, 1973, **8**, 2485-2495.

90.   E. I. Blout, *Solid State Phys.*, 1962, **13**, 305-373.

91.   G. H. Wannier, *Phys. Rev.*, 1937, **52**, 0191-0197.

92.   I. Souza, N. Marzari and D. Vanderbilt, *Phys. Rev. B*, 2002, **65**, 035109.

93.   N. Marzari and D. Vanderbilt, *Phys. Rev. B*, 1997, **56**, 12847-12865.

94.   G. Pizzi, D. Volja, B. Kozinsky, M. Fornari and N. Marzari, *Comput. Phys. Commun.*, 2014, **185**, 422-429.

95.   K. Parlinski, Z. Q. Li and Y. Kawazoe, *Phys. Rev. Lett.*, 1997, **78**, 4063-4066.

96.   L. Bjerg, B. B. Iversen and G. K. H. Madsen, *Phys. Rev. B*, 2014, **89**, 024304.

97. W. Li, J. Carrete, N. A. Katcho and N. Mingo, *Comput. Phys. Commun.*, 2014, **185**, 1747-1758.

98. A. J. H. McGaughey and M. Kaviany, *Phys. Rev. B*, 2004, **69**.

99. W. Li, N. Mingo, L. Lindsay, D. A. Broido, D. A. Stewart and N. A. Katcho, *Phys. Rev. B*, 2012, **85**.

100. W. Li, L. Lindsay, D. A. Broido, D. A. Stewart and N. Mingo, *Phys. Rev. B*, 2012, **86**, 174307.

101. R. Grau-Crespo, S. Hamad, C. R. A. Catlow and N. H. de Leeuw, *J. Phys. Condens. Matter*, 2007, **19**, 256201.

102. Q. Wang, R. Grau-Crespo and N. H. de Leeuw, *J. Phys. Chem. B*, 2011, **115**, 13854-13861.

103. P. Gütlich, K. J. Range, C. Felser, C. Schultz-Munzenberg, W. Tremel, D. Walcher and M. Waldeck, *Angew. Chem. Int. Ed.*, 1999, **38**, 2381-2384.

104. P. Vaqueiro and G. G. Sobany, *Solid State Sci.*, 2009, **11**, 513-518.

105. A. Aziz, P. Mangelis, P. Vaqueiro, A. V. Powell and R. Grau-Crespo, *Phys. Rev. B*, 2016, **94**, 165131.

106. T. Sakamoto, M. Wakeshima and Y. Hinatsu, *J. Phys. Condens. Matter*, 2006, **18**, 4417-4426.

107. W. Schnelle, A. Leithe-Jasper, H. Rosner, F. M. Schappacher, R. Pöettgen, F. Pielnhofer and R. Weihrich, *Phys. Rev. B*, 2013, **88**, 144404.

108. R. Weihrich and I. Anusca, *Z. Anorg. Allg. Chem.*, 2006, **632**, 1531-1537.

109. T. Kubodera, H. Okabe, Y. Kamihara and M. Matoba, *Physica B Condens. Matter*, 2006, **378-80**, 1142-1143.

110. J. M. D. Coey and S. Sanvito, *J. Phys. D*, 2004, **37**, 988-993.

111. J. Rothballer, F. Bachhuber, F. Pielnhofer, F. M. Schappacher, R. Pöettgen and R. Weihrich, *Eur. J. Inorg. Chem.*, 2013, 248-255.

112. A. Umetani, E. Nagoshi, T. Kubodera and M. Matoba, *Physica B Condens. Matter*, 2008, **403**, 1356-1358.

113. W. M. Skinner, G. J. Qian and A. N. Buckley, *J. Solid State Chem.*, 2013, **206**, 32-37.

114. F. Pielnhofer, J. Rothballer, P. Peter, W. Yan, F. M. Schappacher, R. Pöettgen and R. Weihrich, *Z. Anorg. Allg. Chem.*, 2014, **640**, 286-294.

115. J. Rothballer, F. Bachhuber, S. M. Rommel, T. Sohnel and R. Weihrich, *RSC Adv.*, 2014, **4**, 42183-42189.

116. M. Fujioka, T. Shibuya, J. Nakai, K. Yoshiyasu, Y. Sakai, Y. Takano, Y. Kamihara and M. Matoba, *Solid State Commun.*, 2014, **199**, 56-60.

117. J. Corps, P. Vaqueiro, A. Aziz, R. Grau-Crespo, W. Kockelmann, J.-C. Jumas and A. V. Powell, *Chem. Mater.*, 2015, **27**, 3946-3956.

118. L. Wang, T. Y. Chen and C. Leighton, *Phys. Rev. B*, 2004, **69**, 094412.

119. T. Graf, G. H. Fecher, J. Barth, J. Winterlik and C. Felser, *J. Phys. D*, 2009, **42**, 084003.

120.   G. Kresse and J. Furthmüller, *Phys. Rev. B*, 1996, **54**, 11169-11186.

121.   G. Kresse and J. Furthmüller, *Comput. Mater. Sci.*, 1996, **6**, 15-50.

122.   R. F. W. Bader, *Atoms in Molecules: A Quantum Theory*, Oxford University Press, New York, 1990.

123.   G. Henkelman, A. Arnaldsson and H. Jonsson, *Comput. Mater. Sci.*, 2006, **36**, 354-360.

124.   W. Tang, E. Sanville and G. Henkelman, *J. Phys.: Condens. Matter*, 2009, **21**, 084204.

125.   K. Ramasamy, H. Sims, R. K. Gupta, D. Kumar, W. H. Butler and A. Gupta, *Chem. Mater.*, 2013, **25**, 4003-4009.

126.   A. Togo, F. Oba and I. Tanaka, *Phys. Rev. B*, 2008, **78**, 134106.

127.   A. Michelet and G. Collin, *J. Less-Common Met.*, 1976, **45**, 185-191.

128.   K. J. Range, F. Rau, M. Zabel and H. Paulus, *Z. Kristallogr. Cryst. Mater.*, 1997, **212**, 50-50.

129.   P. Haas, F. Tran and P. Blaha, *Phys. Rev. B*, 2009, **79**, 085104.

130.   C. W. Bauschlicher and P. S. Bagus, *J. Chem. Phys.*, 1984, **81**, 5889-5898.

131.   R. G. McKinlay, N. M. S. Almeida, J. P. Coe and M. J. Paterson, *J. Phys. Chem. A*, 2015, **119**, 10076-10083.

132.   C. V. Manzano, B. Abad, M. Munoz Rojo, Y. R. Koh, S. L. Hodson, A. M. Lopez Martinez, X. Xu, A. Shakouri, T. D. Sands, T. Borca-Tasciuc and M. Martin-Gonzalez, *Sci. Rep.*, 2016, **6**, 19129.

133.   B.-Z. Sun, Z. Ma, C. He and K. Wu, *Phys. Chem. Chem. Phys.*, 2015, **17**, 29844-29853.

134.   R. M. Fernandes, E. Abrahams and J. Schmalian, *Phys. Rev. Lett.*, 2011, **107**, 217002.

135.   J. Xiao, M. Long, X. Li, H. Xu, H. Huang and Y. Gao, *Sci. Rep.*, 2014, **4**, 4327.

136.   S. Ponce, E. R. Margine, C. Verdi and F. Giustino, *Comput. Phys. Commun.*, 2016, **209**, 116-133.

137.   B. Y. Yavorsky, N. F. Hinsche, I. Mertig and P. Zahn, *Phys. Rev. B*, 2011, **84**, 165208.

138.   K. E. Goodson, *Science*, 2007, **315**, 342-343.

139.   A. Balandin and K. L. Wang, *Phys. Rev. B*, 1998, **58**, 1544-1549.

140.   Y. Suzuki and H. Nakamura, *Phys. Chem. Chem. Phys.*, 2015, **17**, 29647-29654.

141.   K. Knížek, *Phys. Rev. B*, 2015, **91**, 075125.

142.   L. Gravier, A. Fábián, A. Rudolf, A. Cachin, J. E. Wegrowe and J. P. Ansermet, *J. Magn. Magn. Mater.*, 2004, **271**, 153-158.

143.   H. J. Xiang and D. J. Singh, *Phys. Rev. B*, 2007, **76**, 195111.

144.   C. Wood, *Rep. Prog. Phys.*, 1988, **51**, 459-539.

145. S. L. Dudarev, A. I. Liechtenstein, M. R. Castell, G. A. D. Briggs and A. P. Sutton, *Phys. Rev. B*, 1997, **56**, 4900-4908.

146. Q. Guo, G. M. Ford, W. C. Yang, B. C. Walker, E. A. Stach, H. W. Hillhouse and R. Agrawal, *J. Am. Chem. Soc.*, 2010, **132**, 17384-17386.

147. S. Chen, X. G. Gong, A. Walsh and S.-H. Wei, *Appl. Phys. Lett.*, 2009, **94**, 041903.

148. S. Chen, A. Walsh, Y. Luo, J.-H. Yang, X. G. Gong and S.-H. Wei, *Phys. Rev. B*, 2010, **82**.

149. S. Delbos, *EPJ Photovolt.*, 2012, **3**, 35004.

150. C. Sevik and T. Çağın, *Phys. Rev. B*, 2010, **82**, 045202.

151. T. Gokmen, O. Gunawan and D. B. Mitzi, *Appl. Phys. Lett.*, 2014, **105**, 033903.

152. S. Schorr, H.-J. Hoebler and M. Tovar, *Eur. J. Mineral.*, 2007, **19**, 65-73.

153. J. J. S. Scragg, J. K. Larsen, M. Kumar, C. Persson, J. Sendler, S. Siebentritt and C. Platzer-Björkman, *Phys. Status Solidi B*, 2016, **253**, 247-254.

154. D. B. Mitzi, O. Gunawan, T. K. Todorov and D. A. R. Barkhouse, *Phil. Trans. R. Soc. A*, 2013, **371**, 20110432.

155. S. Bourdais, C. Choné, B. Delatouche, A. Jacob, G. Larramona, C. Moisan, A. Lafond, F. Donatini, G. Rey, S. Siebentritt, A. Walsh and G. Dennler, *Adv. Energy Mater.*, 2016, **6**, 1502276.

156. D. Huang and C. Persson, *Thin Solid Films*, 2013, **535**, 265-269.

157. J. J. S. Scragg, L. Choubrac, A. Lafond, T. Ericson and C. Platzer-Björkman, *Appl. Phys. Lett.*, 2014, **104**, 041911.

158. G. Rey, A. Redinger, J. S. Ler, T. P. Weiss, M. Thevenin, M. Guennou, B. El Adib and S. Siebentritt, *Appl. Phys. Lett.*, 2014, **105**, 112106.

159. C. Raju, M. Falmbigl, P. Rogl, X. Yan, E. Bauer, J. Horky, M. Zehetbauer and R. C. Mallik, *AIP Adv.*, 2013, **3**, 032106.

160. Y. Dong, A. R. Khabibullin, K. Wei, Z. H. Ge, J. Martin, J. R. Salvador, L. M. Woods and G. S. Nolas, *Appl. Phys. Lett.*, 2014, **104**, 252107.

161. M. Valentini, C. Malerba, F. Menchini, D. Tedeschi, A. Polimeni, M. Capizzi and A. Mittiga, *Appl. Phys. Lett.*, 2016, **108**, 211909.

162. S. Chen, A. Walsh, J.-H. Yang, X. G. Gong, L. Sun, P.-X. Yang, J.-H. Chu and S.-H. Wei, *Phys. Rev. B*, 2011, **83**, 125201.

163. C. H. Ma, H. F. Guo, K. Z. Zhang, N. Y. Yuan and J. N. Ding, *Mater. Lett.*, 2017, **186**, 390-393.

164. T. Jing, Y. Dai, X. C. Ma, W. Wei and B. B. Huang, *J. Phys. Chem. C*, 2015, **119**, 27900-27908.

165. T. Sasamura, T. Osaki, T. Kameyama, T. Shibayama, A. Kudo, S. Kuwabata and T. Torimoto, *Chem. Lett.*, 2012, **41**, 1009-1011.

166. I. Tsuji, Y. Shimodaira, H. Kato, H. Kobayashi and A. Kudo, *Chem. Mater.*, 2010, **22**, 1402-1409.

167. N. Kamoun, H. Bouzouita and B. Rezig, *Thin Solid Films*, 2007, **515**, 5949-5952.

168. T. Tanaka, T. Nagatomo, D. Kawasaki, M. Nishio, Q. X. Guo, A. Wakahara, A. Yoshida and H. Ogawa, *J. Phys. Chem. Solids*, 2005, **66**, 1978-1981.

169. J. S. Seol, S. Y. Lee, J. C. Lee, H. D. Nam and K. H. Kim, *Sol. Energy Mater. Sol. Cells*, 2003, **75**, 155-162.

170. H. Katagiri, K. Saitoh, T. Washio, H. Shinohara, T. Kurumadani and S. Miyajima, *Sol. Energy Mater. Sol. Cells*, 2001, **65**, 141-148.

171. J. J. Scragg, P. J. Dale, L. M. Peter, G. Zoppi and I. Forbes, *Phys. Status Solidi B*, 2008, **245**, 1772-1778.

172. K. Sekiguchi, K. Tanaka, K. Moriya and H. Uchiki, ed. M. Stutzmann, *Phys. Status Solidi C* 2006, **3**, 2618-2621.

173. N. Nakayama and K. Ito, *Appl. Surf. Sci.*, 1996, **92**, 171-175.

174. J. Zhang, L. Shao, Y. Fu and E. Xie, *Rare Metals*, 2006, **25**, 315-319.

175. G. Brammertz, M. Buffiere, S. Oueslati, H. ElAnzeery, K. Ben Messaoud, S. Sahayaraj, C. Koeble, M. Meuris and J. Poortmans, *Appl. Phys. Lett.*, 2013, **103**, 163904.

176. S. G. Choi, T. J. Kim, S. Y. Hwang, J. Li, C. Persson, Y. D. Kim, S. H. Wei and I. L. Repins, *Sol. Energy Mater. Sol. Cells*, 2014, **130**, 375-379.

177. S. Giraldo, M. Neuschitzer, T. Thersleff, S. Lopez-Marino, Y. Sanchez, H. Xie, M. Colina, M. Placidi, P. Pistor, V. Izquierdo-Roca, K. Leifer, A. Perez-Rodriguez and E. Saucedo, *Adv. Energy Mater.*, 2015, **5**, 1501070.

178. Z. Y. Zhao, Q. L. Liu and X. Zhao, *J. Alloys Compd.*, 2015, **618**, 248-253.

179. W. G. Zeier, Y. Z. Pei, G. Pomrehn, T. Day, N. Heinz, C. P. Heinrich, G. J. Snyder and W. Tremel, *J. Am. Chem. Soc.*, 2013, **135**, 726-732.

180. W. G. Zeier, A. LaLonde, Z. M. Gibbs, C. P. Heinrich, M. Panthofer, G. J. Snyder and W. Tremel, *J. Am. Chem. Soc.*, 2012, **134**, 7147-7154.

181. A. A. Mostofi, J. R. Yates, G. Pizzi, Y. S. Lee, I. Souza, D. Vanderbilt and N. Marzari, *Comput. Phys. Commun.*, 2014, **185**, 2309-2310.

182. J. D. Gale and A. L. Rohl, *Mol Simul.*, 2003, **29**, 291-341.

183. M. A. Green, K. Emery, Y. Hishikawa, W. Warta and E. D. Dunlop, *Prog. Photovoltaics*, 2015, **23**, 805-812.

184. D. B. Khadka and J. H. Kim, *CrystEngComm*, 2013, **15**, 10500-10509.

185. K. Wei and G. S. Nolas, *ACS Appl. Mater. Interfaces*, 2015, **7**, 9752-9757.

186. J. O. Sofo and G. D. Mahan, *Phys. Rev. B*, 1994, **49**, 4565-4570.

187. X. Y. Shi, F. Q. Huang, M. L. Liu and L. D. Chen, *Appl. Phys. Lett.*, 2009, **94**, 122103.

188. M. L. Liu, F. Q. Huang, L. D. Chen and I. W. Chen, *Appl. Phys. Lett.*, 2009, **94**, 202103.

189. T. Prabhakar and N. Jampana, *Sol. Energy Mater. Sol. Cells*, 2011, **95**, 1001-1004.

190. K. Wang, O. Gunawan, T. Todorov, B. Shin, S. J. Chey, N. A. Bojarczuk, D. Mitzi and S. Guha, *Appl. Phys. Lett.*, 2010, **97**, 143508.

191. J. P. Leitao, N. M. Santos, P. A. Fernandes, P. M. P. Salome, A. F. da Cunha, J. C. Gonzalez, G. M. Ribeiro and F. M. Matinaga, *Phys. Rev. B*, 2011, **84**, 024120.

192. Z. H. Zhou, Y. Y. Wang, D. Xu and Y. F. Zhang, *Sol. Energy Mater. Sol. Cells*, 2010, **94**, 2042-2045.

193. R. A. Wibowo, E. S. Lee, B. Munir and K. H. Kim, *Phys. Status Solidi A*, 2007, **204**, 3373-3379.

194. G. S. Babu, Y. B. K. Kumar, P. U. Bhaskar and S. R. Vanjari, *Sol. Energy Mater. Sol. Cells*, 2010, **94**, 221-226.

195. S. Y. Chen, A. Walsh, X. G. Gong and S. H. Wei, *Adv. Mater.*, 2013, **25**, 1522-1539.

196. J. M. Skelton, A. J. Jackson, M. Dimitrievska, S. K. Wallace and A. Walsh, *Apl Materials*, 2015, **3**, 041102.

197. Y. Tachibana, L. Vayssieres and J. R. Durrant, *Nat. Photonics*, 2012, **6**, 511-518.

198. J. C. Colmenares and R. Luque, *Chem. Soc. Rev.*, 2014, **43**, 765-778.

199. G. Férey, C. Mellot-Draznieks, C. Serre and F. Millange, *Acc. Chem. Res.*, 2005, **38**, 217-225.

200. A. K. Cheetham, C. N. R. Rao and R. K. Feller, *Chem. Commun.*, 2006, 4780-4795.

201. H.-C. Zhou and S. Kitagawa, *Chem. Soc. Rev.*, 2014, **43**, 5415-5418.

202. H. Furukawa, K. E. Cordova, M. O'Keeffe and O. M. Yaghi, *Science*, 2013, **341**, 1230444.

203. M. P. Suh, H. J. Park, T. K. Prasad and D.-W. Lim, *Chem. Rev.*, 2012, **112**, 782-835.

204. K. Sumida, D. L. Rogow, J. A. Mason, T. M. McDonald, E. D. Bloch, Z. R. Herm, T.-H. Bae and J. R. Long, *Chem. Rev.*, 2012, **112**, 724-781.

205. A. Dhakshinamoorthy, M. Alvaro, A. Corma and H. Garcia, *Dalton Trans.*, 2011, **40**, 6344-6360.

206. J. Liu, P. K. Thallapally, B. P. McGrail, D. R. Brown and J. Liu, *Chem. Soc. Rev.*, 2012, **41**, 2308-2322.

207. Z. Wang and S. M. Cohen, *Chem. Soc. Rev.*, 2009, **38**, 1315-1329.

208. J. Gascon, M. D. Hernandez-Alonso, A. R. Almeida, G. P. M. van Klink, F. Kapteijn and G. Mul, *ChemSusChem*, 2008, **1**, 981 - 983.

209. M.-H. Zeng, B. Wang, X.-Y. Wang, W.-X. Zhang, X.-M. Chen and S. Gao, *Inorg. Chem.*, 2006, **45**, 7069-7076.

210. D. T. de Lill, A. de Bettencourt-Dias and C. L. Cahill, *lnorg. Chem.*, 2007, **46**, 3960-3965.

211. M. A. Nasalevich, M. van der Veen, F. Kapteijn and J. Gascon, *CrystEngComm*, 2014, **16**, 4919-4926.

212. J. B. Allison and R. S. Becker, *J. Chem. Phys.*, 1960, **32**, 1410-1417.

213. Y. Liu, Y. Yang, Q. Sun, Z. Wang, B. Huang, Y. Dai, X. Qin and X. Zhang, *ACS Appl. Mater. Interfaces*, 2013, **5**, 7654-7658.

214. A. Aziz, A. R. Ruiz-Salvador, N. C. Hernández, S. Calero, S. Hamad and R. Grau-Crespo, *J. Mater. Chem. A*, 2017, **5**, 11894-11904.

215. S. Hamad, N. C. Hernández, A. Aziz, A. R. Ruiz-Salvador, S. Calero and R. Grau-Crespo, *J. Mater. Chem. A*, 2015, **3**, 23458-23465.

216. R. Grau-Crespo, A. Y. Al-Baitai, I. Saadoune and N. H. De Leeuw, *J. Phys. Condens. Matter*, 2010, **22**, 255401.

217. R. Grau-Crespo, F. Corà, A. A. Sokol, N. H. de Leeuw and C. R. A. Catlow, *Phys. Rev. B*, 2006, **73**, 035116.

218. C. Hoa, B. Demolder and A. Alexandre, *Appl. Therm. Eng.*, 2003, **23**, 1099-1108.

219. J. E. Huheey, E. A. Keiter and R. L. Keiter, in *Inorganic Chemistry: Principles of Structure and Reactivity*, HarperCollins, New York, USA, 4th edn., 1993.

220. A. M. James and M. P. Lord, *Macmillan's Chemical and Physical Data, Macmillan*, 1992.

221. D. W. Smith, *J. Chem. Educ.*, 1977, **54**, 540-542.

222. Y. Marcus, *J. Chem. Soc., Faraday Trans.*, 1991, **87**, 2995-2999.

223. D. O. Scanlon, C. W. Dunnill, J. Buckeridge, S. A. Shevlin, A. J. Logsdail, S. M. Woodley, C. R. A. Catlow, M. J. Powell, R. G. Palgrave, I. P. Parkin, G. W. Watson, T. W. Keal, P. Sherwood, A. Walsh and A. A. Sokol, *Nat. Mater.*, 2013, **12**, 798-801.

224. R. Asahi, T. Morikawa, T. Ohwaki, K. Aoki and Y. Taga, *Science*, 2001, **293**, 269-271.

225. J. Buckeridge, K. T. Butler, C. R. A. Catlow, A. J. Logsdail, D. O. Scanlon, S. A. Shevlin, S. M. Woodley, A. A. Sokol and A. Walsh, *Chem. Mater.*, 2015, **27**, 3844-3851.

226. G. N. La Mar and F. A. Walker, in *The Porphyrins V4, Physical Chemistry, Part B*, ed. D. Dolphin, Academic Press, London, 1979.

227. S. Bhandary, B. Brena, P. M. Panchmatia, I. Brumboiu, M. Bernien, C. Weis, B. Krumme, C. Etz, W. Kuch, H. Wende, O. Eriksson and B. Sanyal, *Phys. Rev. B*, 2013, **88**, 024401.

228. S. Trasatti, *Pure Appl. Chem.*, 1986, **58**, 955-966.

229. D. K. Kanan and E. A. Carter, *J. Phys. Chem. C*, 2012, **116**, 9876-9887.

230. Y. Wu, P. Lazic, G. Hautier, K. Persson and G. Ceder, *Energy Environ. Sci.*, 2013, **6**, 157-168.

231. Y. H. Fu, D. R. Sun, Y. J. Chen, R. K. Huang, Z. X. Ding, X. Z. Fu and Z. H. Li, *Angew. Chem. Int. Ed.*, 2012, **51**, 3364-3367.

232. M. A. Nasalevich, C. H. Hendon, J. G. Santaclara, K. Svane, B. van der Linden, S. L. Veber, M. V. Fedin, A. J. Houtepen, M. A. van der Veen and F. Kapteijn, *Sci. Rep.*, 2016, **6**, 23676.

233. R. Hill, *J. Phys. C Solid State Phys.*, 1974, **7**, 521-526.

234. F. Capasso, *Science*, 1987, **235**, 172-177.

235. M. Schwarze, W. Tress, B. Beyer, F. Gao, R. Scholz, C. Poelking, K. Ortstein, A. A. Günther, D. Kasemann and D. Andrienko, *Science*, 2016, **352**, 1446-1449.

236. J. A. Johnson, J. Luo, X. Zhang, Y. S. Chen, M. D. Morton, E. Echeverría, F. E. Torres and J. Zhang, *ACS Catal.*, 2015, **5**, 5283-5291.

237. J. A. Johnson, X. Zhang, T. C. Reeson, Y. S. Chen and J. Zhang, *J. Am. Chem. Soc.*, 2014, **136**, 15881-15884.

238. C. W. Kung, T. H. Chang, L. Y. Chou, J. T. Hupp, O. K. Farha and K. C. Ho, *Chem. Commun.*, 2015, **51**, 2414-2417.

239. M. J. Frisch, G. W. Trucks, H. B. Schlegel, G. E. Scuseria, M. A. Robb, J. R. Cheeseman, G. Scalmani, V. Barone, B. Mennucci, G. A. Petersson, H. Nakatsuji, M. Caricato, X. Li, H. P. Hratchian, A. F. Izmaylov, J. Bloino, G. Zheng, J. L. Sonnenberg, M. Hada, M. Ehara, K. Toyota, R. Fukuda, J. Hasegawa, M. Ishida, T. Nakajima, Y. Honda, O. Kitao, H. Nakai, T. Vreven, J. A. Montgomery Jr., J. E. Peralta, F. Ogliaro, M. J. Bearpark, J. Heyd, E. N. Brothers, K. N. Kudin, V. N. Staroverov, R. Kobayashi, J. Normand, K. Raghavachari, A. P. Rendell, J. C. Burant, S. S. Iyengar, J. Tomasi, M. Cossi, N. Rega, N. J. Millam, M. Klene, J. E. Knox, J. B. Cross, V. Bakken, C. Adamo, J. Jaramillo, R. Gomperts, R. E. Stratmann, O. Yazyev, A. J. Austin, R. Cammi, C. Pomelli, J. W. Ochterski, R. L. Martin, K. Morokuma, V. G. Zakrzewski, G. A. Voth, P. Salvador, J. J. Dannenberg, S. Dapprich, A. D. Daniels, Ö. Farkas, J. B. Foresman, J. V. Ortiz, J. Cioslowski and D. J. Fox, Gaussian, Inc., Wallingford, CT, USA, 2009.

240. B. Chen, Z. Yang, Y. Zhu and Y. Xia, *J. Mater. Chem. A*, 2014, **2**, 16811-16831.

241. A. Phan, C. J. Doonan, F. J. Uribe-Romo, C. B. Knobler, M. O'Keeffe and O. M. Yaghi, *Acc. Chem. Res.*, 2010, **43**, 58-67.

242. Y.-Q. Tian, Y.-M. Zhao, Z.-X. Chen, G.-N. Zhang, L.-H. Weng and D.-Y. Zhao, *Chem. Eur. J.*, 2007, **13**, 4146-4154.

243. W. J. Greenlee, in *US Patent* **5**,164,407, 1992.

244. S. Wang, W. Yao, J. Lin, Z. Ding and X. Wang, *Angew. Chem. Int. Ed.*, 2014, **53**, 1034-1038.

245. H. Yang, X.-W. He, F. Wang, Y. Kang and J. Zhang, *J. Mater. Chem.*, 2012, **22**, 21849-21851.

246. K. S. Park, Z. Ni, A. P. Côté, J. Y. Choi, R. Huang, F. J. Uribe-Romo, H. K. Chae, M. O'Keeffe and O. M. Yaghi, *Proc. Natl. Acad. Sci.*, 2006, **103**, 10186-10191.

247. K. Hendrickx, D. E. P. Vanpoucke, K. Leus, K. Lejaeghere, A. Van Yperen-De Deyne, V. Van Speybroeck, P. Van Der Voort and K. Hemelsoet, *lnorg. Chem.*, 2015, **54**, 10701-10710.

248. C. H. Hendon, D. Tiana, M. Fontecave, C. Sanchez, L. D'arras, C. Sassoye, L. Rozes, C. Mellot-Draznieks and A. Walsh, *J. Am. Chem. Soc.*, 2013, **135**, 10942-10945.

249. H. Q. Pham, T. Mai, N.-N. Pham-Tran, Y. Kawazoe, H. Mizuseki and D. Nguyen-Manh, *J. Phys. Chem. C*, 2014, **118**, 4567-4577.

250. R. Grau-Crespo, A. Aziz, A. W. Collins, R. Crespo-Otero, N. C. Hernández, L. M. Rodriguez-Albelo, A. R. Ruiz-Salvador, S. Calero and S. Hamad, *Angew. Chem. Int. Ed.*, 2016, **55**, 16012-16016.

251.   D. R. Sun, Y. H. Fu, W. J. Liu, L. Ye, D. K. Wang, L. Yang, X. Z. Fu and Z. H. Li, *Chem. Eur. J.*, 2013, **19**, 14279-14285.

252.   B. Pattengale, S. Yang, J. Ludwig, Z. Huang, X. Zhang and J. Huang, *J. Am. Chem. Soc.*, 2016, **138**, 8072-8075.

253.   A. R. Supka, T. E. Lyons, L. Liyanage, P. D'Amico, R. A. Al Orabi, S. Mahatara, P. Gopal, C. Toher, D. Ceresoli, A. Calzolari, S. Curtarolo, M. B. Nardelli and M. Fornari, *Comput. Mater. Sci.*, 2017, **136**, 76-84.